LBL-23512
UC-25

Center for Advanced Materials

CAM REPORT

RECEIVED
LAWRENCE
BERKELEY LABORATORY

JUL 14 1987

LIBRARY AND
DOCUMENTS SECTION

ION BEAM CHARACTERIZATION OF THIN FILM METAL/GaAs INTERFACE REACTIONS

K. M. Yu
(Ph.D. Thesis)

May 1987

For Reference

Not to be taken from this room

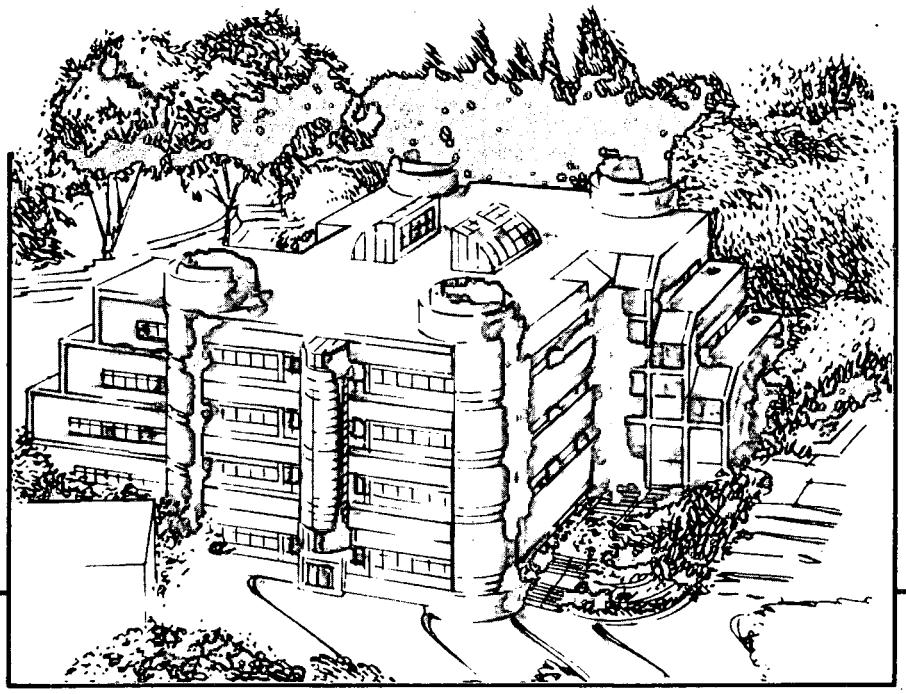

Materials and Chemical Sciences Division

Lawrence Berkeley Laboratory • University of California

ONE CYCLOTRON ROAD, BERKELEY, CA 94720 • (415) 486-4755

Prepared for the U.S. Department of Energy under Contract DE-AC03-76SF00098

LBL-23512

DISCLAIMER

This document was prepared as an account of work sponsored by the United States Government. While this document is believed to contain correct information, neither the United States Government nor any agency thereof, nor the Regents of the University of California, nor any of their employees, makes any warranty, express or implied, or assumes any legal responsibility for the accuracy, completeness, or usefulness of any information, apparatus, product, or process disclosed, or represents that its use would not infringe privately owned rights. Reference herein to any specific commercial product, process, or service by its trade name, trademark, manufacturer, or otherwise, does not necessarily constitute or imply its endorsement, recommendation, or favoring by the United States Government or any agency thereof, or the Regents of the University of California. The views and opinions of authors expressed herein do not necessarily state or reflect those of the United States Government or any agency thereof or the Regents of the University of California.

LBL-23512

ION BEAM CHARACTERIZATION OF THIN FILM METAL/GaAs INTERFACE REACTIONS

Kin Man Yu

Ph. D. Dissertation

Lawrence Berkeley Laboratory
and
Department of Materials Science and Mineral Engineering
University of California, Berkeley.
Berkeley, Ca 94720

May 1987

ION BEAM CHARACTERIZATION OF THIN FILM METAL/GaAs INTERFACE REACTIONS

Kin Man Yu

Center For Advanced Materials
Lawrence Berkeley Laboratory
and
Department of Materials Science and Mineral Engineering
University of California,
Berkeley, Ca

ABSTRACT

Metal contacts are essential to all semiconductor devices. In this study the thermally activated interface interactions of (100) GaAs and thin films of near noble metals (Co, Rh, Ir, Ni, Pd and Pt) and refractory metals (Ti, Zr, V, Nb, Cr, Mo and W) were systematically investigated. Depth profilings of M/GaAs interfaces were achieved using ion beam analytical techniques including conventional and heavy ion Rutherford backscattering spectrometry. Information on the structure and morphology of the reacted phases was obtained by x-ray diffraction and transmission electron microscopy. For some systems (Co/GaAs, Rh/GaAs, Ni/GaAs, Pd/GaAs, Pt/GaAs and W/GaAs), electrical measurements were also carried out with current voltage dependence of the diodes.

Results of this study indicate that interface reactivity and the reacted phase distribution of metal/GaAs contacts were dependent on the electronegativity differences between the metal and the substrate as

well as the metal-metal bond strength of the metal. For near noble metals which are very electronegative ($X \geq 1.8$) and have relatively weak M-M bonds, reactions between metal and GaAs were initiated at low temperatures ($\leq 350\,°C$). For refractory metals which are relatively electropositive ($X \leq 1.8$) and have stronger M-M bonds, the metal/GaAs interfaces were relatively inert (reactions observed at temperatures $\geq 450\,°C$). It was also found that for metals with $|X_M - X_{Ga}| \neq |X_M - X_{As}|$, a layer sequence of M-Ga/M-As/GaAs was always observed after reactions. A relationship between the interface reactivity and the activation energy of reactions for refractory metal/GaAs contacts was proposed. The electrical properties of metal/n-GaAs diodes were also correlated with the M/GaAs solid phase reactions. Important issues of the solid-state reactions of metal/GaAs contacts such as the phase formation sequence, reaction kinetics, and the distribution and stability of the different M-Ga and M-As phases will be discussed in detail.

ACKNOWLEDGMENTS

I would like to express my gratitude to my research advisors, Professor Eugene Haller and Dr. Joseph Jaklevic for their guidance, support and encouragement throughout the course of my graduate education. It has been my pleasure to collaborate with Dr. Tim Sands in the study of near noble metal/GaAs interfaces, and I wish to thank him for allowing me to include the TEM results in this thesis. Thanks are due to Dr. Wladek Walukiewicz for many invaluable and stimulating discussions on theory of Schottky barrier formation. I would like to acknowledge S. K. Cheung for his assistance in sputter deposition of thin films and electrical measurements of Schottky contacts.

I would also like to thank W. L. Searles for his expert technical assistance and for keeping the Van de Graaff running. The HIRBS experiments were made possible through the cooperation and assistance of R. Stokstad, R. M. Larimer and the staff of the 88" cyclotron at LBL.

I am grateful to Professor D. deFontaine and Professor N. W. Cheung for reading and commenting on this manuscript.

Finally I wish to express my deepest thanks to my family and friends. I especially wish to thank my wife, Sandra, without her patience, understanding and encouragement this work would not be possible.

I wish acknowledge the support of an Atlantic Richfield Corporation Fellowship. This work was supported by the Director, Office of Energy Research, Office of Basic Sciences, Materials Science Division of the U. S. Department of Energy under Contract No. DE-AC03-76SF-00098.

TABLE OF CONTENTS

Chapter 1: Introduction.....1

1.1 Electrical Properties of Metal/Semiconductor Contacts.....3
1.1.1 Schottky contacts.....3
1.1.2 Ohmic contacts.....7

1.2 Models for Metal/GaAs Schottky Barrier Formation.....11
1.2.1 Unified defect model (UDM).....11
1.2.2 Effective work function model (EWFM).....13
1.2.3 Metal induced gap state (MIGS) model.....15
1.2.4 Amphoteric native defect model.....17

1.3 Metal/Semiconductor Interface Reactions.....19
1.3.1 Metal/Si contact reactions-silicide formation.....21
1.3.2 Metal/GaAs contact reactions.....26

References.....32

Chapter 2: Characterization Techniques.....40

2.1 Conventional and Heavy Ion Rutherford Backscattering Spectrometry.....41
2.1.1 General background of RBS.....43
2.1.2 RBS spectrum for thin film samples.....51
2.1.3 Limitations of conventional RBS on thin film analysis.....56
2.1.4 Advantages of heavy-ion RBS (HIRBS).....59
2.1.5 Instrumentation.....67

2.2 Complementary Techniques.....68

References.....71

Chapter 3: Results and Discussions I: Solid Phase Reactions Between (100) GaAs and Near Noble Metal Films.....74

3.1 Co/GaAs.....74

3.2 Rh/GaAs.....83

3.3 Ir/GaAs.....89

3.4 Ni/GaAs.....99

3.5 Pd/GaAs.....105

3.6 Pt/GaAs.....115

3.7 Summary and Conclusions on
Near Noble Metal/GaAs Reactions.....120
3.7.1 Phase composition and structure.....120
3.7.2 Phase distribution and morphology.....121
3.7.3 Reaction kinetics.....123

References.....125

Chapter 4: Results and Discussions II: Solid Phase Reactions
Between (100) GaAs and Refractory Metal Films.....128

4.1 Ti/GaAs.....130

4.2 Zr/GaAs.....134

4.3 V/GaAs.....139

4.4 Nb/GaAs.....144

4.5 Cr/GaAs.....146

4.6 Mo/GaAs.....150

4.7 W/GaAs.....155

4.8 Summary and Conclusions on
Refractory Metal/GaAs Reactions.....165
4.8.1 Phase composition and structure.....165
4.8.2 Phase distribution and morphology.....166
4.8.3 Reaction kinetics.....167

References.....169

Chapter 5: Results and Discussions III: Correlations Between
Electrical Behaviors and Interface Metallurgy.....171

5.1 Very Reactive M/GaAs Contacts (M=Co, Ni and Pd).....172

5.2 Reactive M/GaAs Contacts (M=Rh and Pt).....176

5.3 Non-Reactive M/GaAs Contact: W/GaAs Contact.....180

References.....187

Chapter 6: Further Discussions of
Experimental Results and Summary.....188

6.1 Systematics of The Solid Phase Reactions
of Thin Film Metal/GaAs Interface Reactions.....188
6.1.1 Reaction kinetics.....188
6.1.2 Interface reactivity.....189
6.1.3 Phase distribution.....194

6.2 Dependence of Electrical Properties on
The Interface Reactions of Metal/n-GaAs diodes.....196

6.3 Summary.....201

References.....204

Appendix: Sample Preparation Procedures.....205

LIST OF ACRONYMS

AES	Auger Electron Spectroscopy
BF	Bright Field
C-V	Capacitance-Voltage
CBM	Conduction Band Maximum
EDS	Energy Dispersive x-ray Spectroscopy
EWFM	Effective Work Function Model
FWHM	Full Width at Half Maximum
HIRBS	Heavy Ion Rutherford Backscattering Spectrometry
I-V	Current-Voltage
IC	Integrated Circuit
IMPATT	Impact Ionization Avalanche Transit Time
M/III-V	Metal on III-V compound Semiconductor
M/S	Metal on Semiconductor
MBE	Molecular Beam Epitaxy
MESFET	Metal-Semiconductor Field Effect Transistor
MIGS	Metal Induced Gap State
MODFET	Modulation Doped Field Effect Transistor
PES	Photoemission Spectroscopy
RBS	Rutherford Backscattering Spectrometry
SAG	Self Aligned Gate
SB	Schottky Barrier
SEM	Scanning Electron Microscopy

SIMS	Secondary Ion Mass Spectrmetry
SXPS	Soft X-ray Photoemission Spectroscopy
TED	Transmission Electron Diffraction
TEM	Transmission Electron Microscopy
UDM	Unified Defect Model
VLSI	Very Large Scale Integration
XRD	X-Ray Diffraction

Chapter 1 INTRODUCTION

For many decades, III-V compound semiconductors such as GaAs and InP have been known to have certain advantages over elemental semiconductors (Si and Ge). These advantages include efficient light generation, high mobility of electrons and the availability of semi-insulating substrates. In the late 70s the development of thin film crystal growth technology such as molecular beam epitaxy allowed the growth of high quality compound semiconductor films with controllable thickness. This enabled the fabrication of novel electronic and photonic devices using the unique properties of III-V compound semiconductors. Among the III-V compounds, GaAs is the best studied because of its desirable properties for optoelectronic devices and high speed electronic devices. The inherent advantages of GaAs together with the existing silicon technology provide promising prospects for the development of ultra high speed, high density GaAs integrated circuits. Although to a large extent, the technology developed for Si such as lithography, surface preparation, film deposition, design, etc., can be transferred to the development of GaAs circuits, new technology (art) must be developed. This is because of the many differences in the material nature of GaAs and Si.

It is well known from the experiences with silicon devices that the metal/semiconductor interface structures play an important role in all semiconductor devices in the form of rectifying (Schottky) or ohmic contacts. In the case of GaAs, devices utilizing Schottky barrier junctions include solar cells, microwave mixer diodes, metal-semiconductor field effect transistors (MESFETs) and modulation-doped FETs (MODFETs). The importance of ohmic contacts lies in the connection of a device to the outside world. Low resistance ohmic contacts are essential for the high performance of many GaAs devices. The efficiency of light emitting diodes as well as the noise behavior and the gain of MESFETs depend on the quality of the contact. For the very large scale integration (VLSI) of ultra high speed GaAs circuits to become a reality in the near future, one of the most important basic problems to be solved is the fabrication of stable, reliable and reproducible metal contacts to GaAs devices.

Since electrical properties of metal/GaAs (like all other metal/semiconductor) contacts are very sensitive to interface reactions, developing a basic understanding of the metallurgy at the metal/GaAs interface is the first step in solving the GaAs contact problems. This is the main motivation for this work. The objectives of this work are, therefore twofold:

1. to understand the solid phase reactions between thin films of various metal and (100) GaAs substrates and to establish systematics for such reactions, and
2. to correlate interface metallurgy with electrical properties of metal/GaAs contacts.

Results of this study are presented in chapters 3, 4, and 5 of this thesis. Readers who are not interested in the fine details should refer to the summaries given in chapter 6.

1.1 Electrical Properties of Metal/Semiconductor Contacts

According to their resultant electrical behavior, metal/semiconductor (M/S) junctions can be classified into two categories: 1) rectifying junctions which allow current flow when bias is applied to the junction in one direction but blocks current when bias is applied in the opposite direction, and 2) ohmic junctions which allow a free current flow across the junction for both polarities of the applied bias. These two types of contacts will be briefly described in the following sections.

1.1.1 Schottky contacts

The rectification behavior at M/S interfaces was first explained independently by Schottky[1], Mott[2] and Davidov[3]. Contacts which exhibit this behavior are often referred to as Schottky barrier contacts. According to the classical theory of Schottky[1], a metal coming in contact with a semiconductor creates a potential difference across the interface by the redistribution of charges across the junction. This potential difference is referred to as the Schottky barrier (SB). Schottky suggested that the height of this barrier is equal to the difference between the work function of the deposited metal ξ_m and the

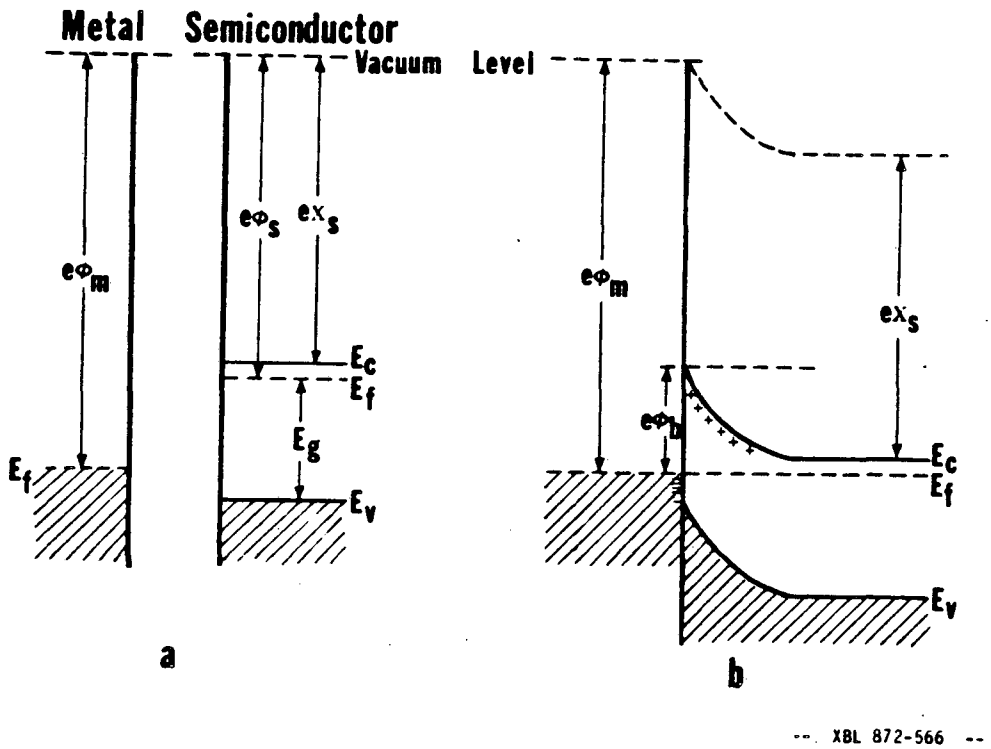

Figure 1.1 The electron energy band diagrams for a metal with high work function and an n-type semiconductor with $\xi_m > X_s$ before (a) and after (b) contact.

electron affinity of the semiconductor X_s. Figure 1.1 shows the electron energy band diagrams for a metal with high work function and a n-type semiconductor with $\xi_m > X_s$ before and after contact. It is obvious from this figure that the SB height ξ_b can be expressed as $\xi_b = \xi_m - X_s$.

Current transport in M/S contacts is mainly due to majority carriers, i.e. in the case of n-type semiconductors, due to electrons. The transport of electrons or holes over the potential barrier can be adequately described by the thermionic emission theory developed by Bethe[4]. According to this theory, the current-voltage (I-V) relationship for a M/S junction can be described by in the following equation:

$$J = A^{*}T^{2}\exp\left(\frac{-q\phi_b}{kT}\right)\left[\exp\left(\frac{qV_a}{nkT}\right) - 1\right] \qquad (1.1)$$

where J is the total current flux, A^* is the effective Richardson constant[5], k is the Boltzmann constant, T is the measurement temperature in degree Kelvin and V_a is the applied bias. The rectifying property of a M/S contact is illustrated in Figure 1.2 where the current transport under forward, zero and reverse applied bias conditions is illustrated according to the thermionic emission theory.

Schottky's model discussed above was proposed to explain ideal M/S junctions, i.e. the metal is in intimate contact with the semiconductor so that the interface is abrupt, uniform and free from any contamination and defects. In reality, however, such an ideal interface can

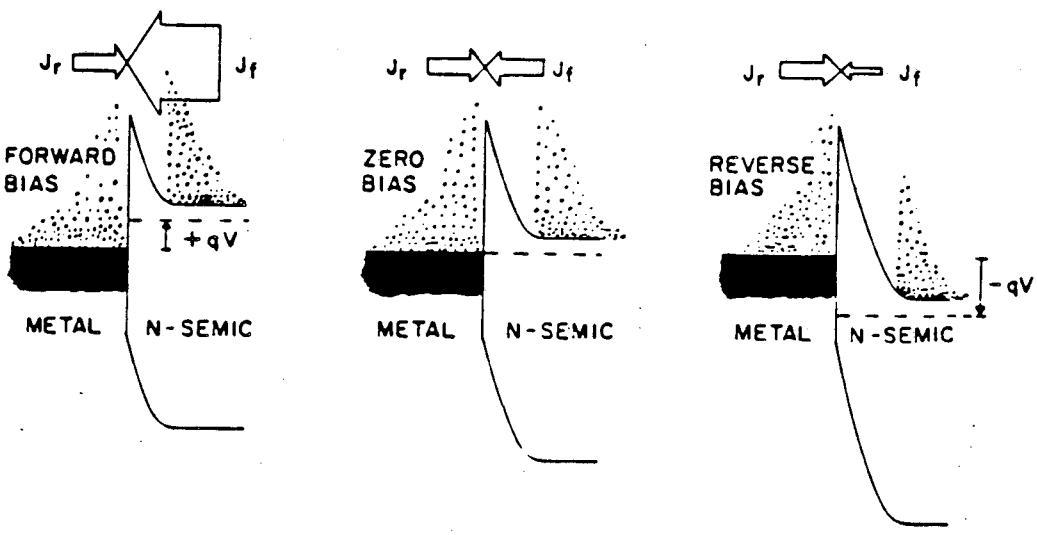

Figure 1.2 Schematic of the thermionic model for a M/S contact under forward, zero and reverse applied bias conditions (Reference 6. Reprinted with permission of Solid-State Electron., Vol. 18, V.L. Rideout, "A Review of the Theory and Technology for Ohmic Contacts to Group III-V Compound Semiconductors," 1975, Pergamon Press, Ltd.

rarely be realized. Therefore, the Schottky model cannot explain "real" contact systems. In fact, most experimental results showed that the SB height is almost independent of the metal deposited. In 1947 Bardeen[7] introduced the idea of "pinning" of the semiconductor fermi level at the M/S interface by states due to imperfection. Bardeen suggested that this pinning is responsible for the experimentally observed insensitivity of the barrier heights to the metal work functions.

With the advancement of ultra high vacuum technology and the development of novel surface sensitive characterization techniques in the past decades, comprehensive surface science studies on III-V surfaces and M/S interfaces have been carried out[8]. Many new models on the SB formation mechanism have been proposed to explain the experimental results. All of these models are, however, extensions of the ideas of either Schottky or Bardeen. Models based on the idea of pinning include:

1. Unified Defect Model (UDM) proposed by Spicer et al[9] in 1979,
2. Metal Induced Gap States (MIGS) model proposed by Heine[10] in 1965 and later developed by Louie et al[11] and Tersoff[12], and
3. Amphoteric native defect model proposed by Walukiewicz[13] in 1986.

The main difference among the above mentioned models lies in the nature and source of the pinning states. Aside from these pinning models, in 1981 Freeouf and Woodall[14] proposed another model in the spirit of Schottky known as the effective Work Function Model (EWFM). These models will be briefly reviewed in section 1.2.

1.1.2 Ohmic contacts

Another type of M/S contact is the ohmic contact which has very different electrical behavior from the Schottky contact. An ohmic contact is one that has a reproducible linear I-V relationship characterized by low electrical resistance. Hence an ideal ohmic contact would be a Schottky barrier with zero barrier height so that carriers can move with minimum loss between the metal and bulk semiconductor. Due to the fermi level pinning phenomenon mentioned in the last section, this kind of ohmic contact is rarely achievable. A special case is InAs which has the surface fermi level pinned in the conduction band [15-17] so that metal/InAs junctions always exhibit zero barrier. However, in most other semiconductors, the fermi level is always pinned inside the energy gap (in many cases close to the mid-gap) so that the M/S junction results in a finite barrier.

Despite the fermi level pinning, low resistance ohmic contacts can still be fabricated by heavily doping the near surface region of the semiconductor to such a high concentration that the surface depletion region associated with this barrier is only several nanometer thick. Electrons can then move across this thin barrier through quantum mechanical tunneling.[18] The operation of such a tunneling ohmic contact is illustrated in Figure 1.3. For n-GaAs, doping levels greater than $5X10^{19}cm^{-3}$ are required if a low enough contact resistivity ($\sim 10^{-6}\Omega cm^2$) shall be achieved[20]. However, such doping level exceeds the solid solubility limit for donors in GaAs. Therefore it is rather unlikely that tunneling ohmic contact can be fabricated for n-GaAs devices.

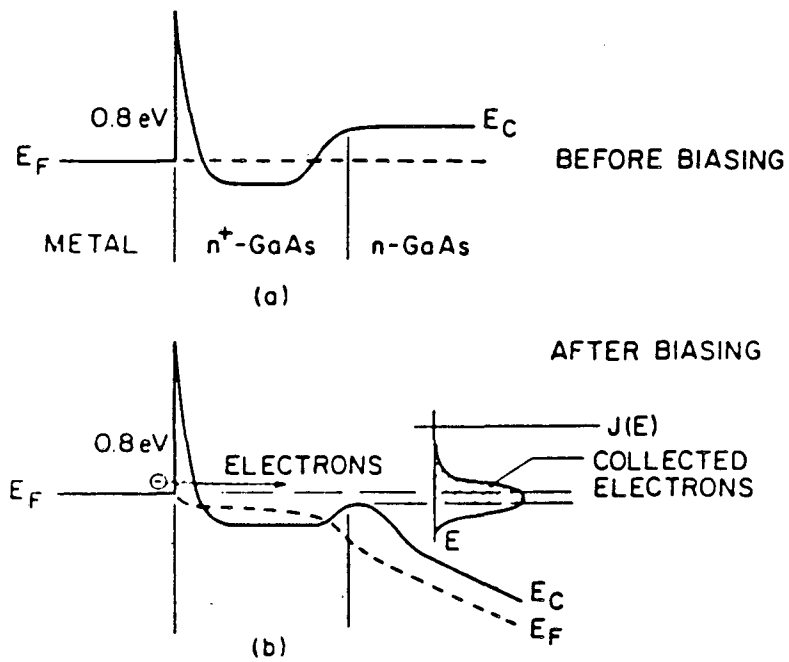

Figure 1.3 Electron energy band diagrams of an n-GaAs tunneling ohmic contact without and with bias (Reference 19. Reprinted with permission of J. Vac. Sci. Technol.).

The most widely used ohmic contact to n-GaAs today is the Au-Ge-Ni/GaAs system alloyed at ~400 °C introduced originally by Braslau et al in 1967 as contact to Gunn effect devices.[21] This system has been extensively studied by many investigators.[22-24] Because of its multi-component nature, the interface metallurgy of this contact system has been found to be extremely complex. In addition, the liquid phase reactions of the contact create a spatially heterogeneous interface. The ohmic properties of this contact are believed to be the result of an inhomogeneous distribution of microscopic Ge rich regions which provide low-resistance current paths to the contact[19]. Ni in this

system acts as a wetting agent to prevent the "balling" of Au on GaAs. Though the Au-Ge based ohmic contact has low contact resistance, it is thermally unstable. The contact resistance increases at temperatures required for further device processing or packaging because of extensive diffusion of Au atoms into the substrate. Moreover, the laterally non uniform morphology of this contact system limits its use in the fabrication of GaAs devices at the micron feature scale for large scale integration circuits.

Recently, sintered, non-alloyed GaAs ohmic contact systems have been developed. Sintered ohmic contacts with Ni-Ge[25], Pd-Ge[26,27], Ge implanted Ni[28] and Si implanted Pt[29] on GaAs have been fabricated with acceptably low contact resistance ($<10^{-4}$ Ω-cm^2). One common feature of these contacts is that the thermally activated solid phase reactions between the overlayer metal and the GaAs substrate are essential in achieving low contact resistivity. The interface metallurgy of these contacts has yet to be investigated in detail. The role of the various metals in these contacts is still not well understood.

Ohmic contacts with lattice matched heteroepitaxial layers grown by molecular beam epitaxy (MBE) have also been under investigations. Ohmic behavior is expected for semiconductors with similar electron affinity. This is observed for the case of the MBE grown n^+-Ge/n-GaAs[30,31] structure and also recently the $In_xGa_{(1-x)}As$/n-GaAs structure with x varies from zero to one from the GaAs to metal interfaces[32,33]. The band structure of the metal/$In_xGa_{(1-x)}As$/n-GaAs contact is shown in Figure 1.4. The semiconductor fermi level at the metal/InAs interface

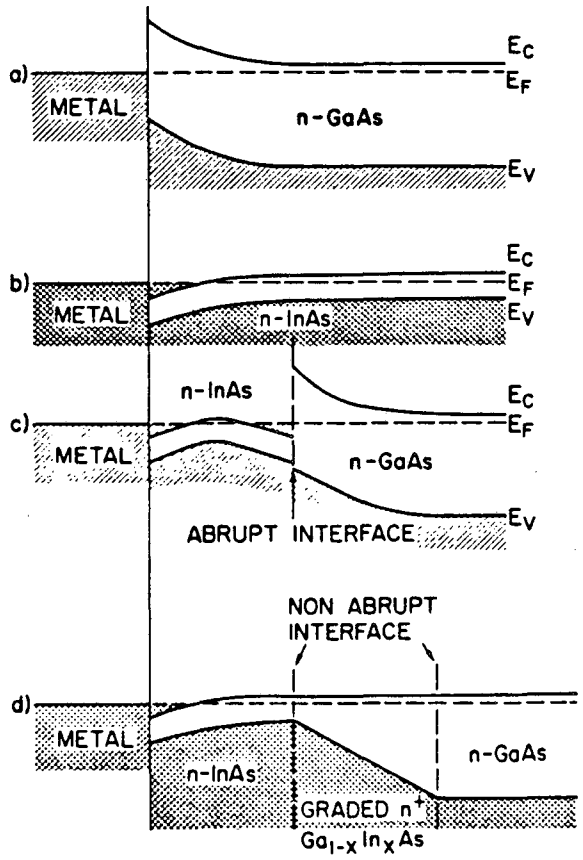

Figure 1.4 Electron energy band diagram of different types of metal/semiconductor interfaces and structures illustrating the heterostrucure ohmic contacts on n-GaAs (Reference 32. Reprinted with permission of J. Vac. Sci. Technol.).

is pinned in the conduction band so that there is no barrier to electron flow and the contact is ohmic. This structure has been shown by Woodall et al[32] to have a very low contact resistance of $<10^{-6}\ \Omega cm^2$.

1.2 Models for Metal/GaAs Schottky Barrier Formation

1.2.1 Unified defect model (UDM)

Based on a large body of experimental data acquired in ultra high vacuum using the surface sensitive photoemission spectroscopy (PES) technique, Spicer et al[9] found that for III-V semiconductors, the interface fermi level pinning is relatively independent of the type of foreign atoms deposited on the semiconductor surface. They also found that the pinning is in many cases already well established at a submonolayer coverage. These observations led them to suggest that the pinning is a result of defects located in the semiconductor near the interface which have been induced by the deposition of the overlayer. They named this model the unified defect model because it supposedly explains the pinning phenomena for a number of interfaces including M/S and insulator/semiconductor in a unified fashion. Spicer et al claimed that the defects responsible for pinning the surface fermi level of the semiconductor are native defects. The energy needed for the formation of these defects is believed to be provided by the heat of condensation of foreign atoms on the semiconductor surface.

For (110) GaAs, The UDM suggests that the interface fermi level is pinned by two levels according to the type of substrate: for n-type substrate, an acceptor level at 0.7 eV below the conduction band minimum (CBM) due to missing anion for p-type substrate, and a donor level at 0.9 eV below CBM due to missing cation. The exact positions

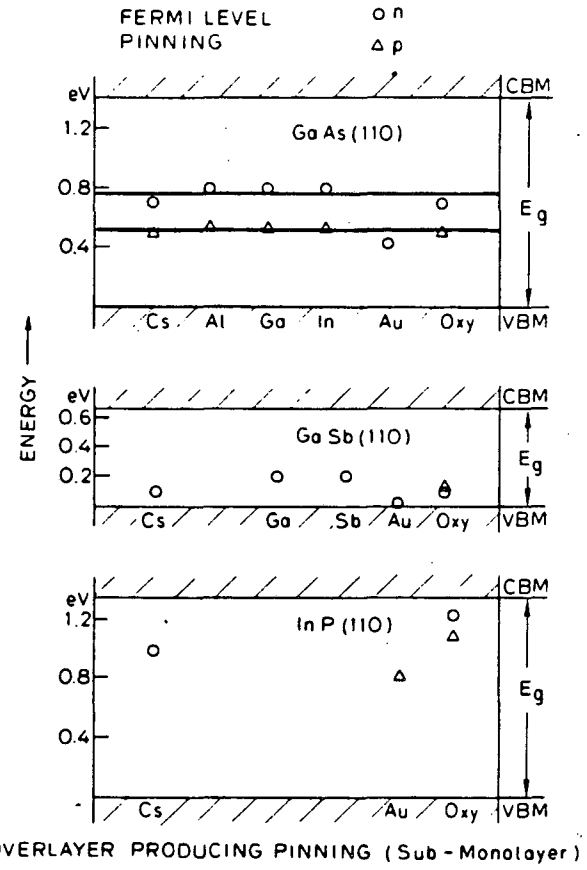

Figure 1.5 The final fermi energy level E_f positions for a number of metals and oxygen on GaSb, GaAs and InP. Note that there is little dependence on the chemical nature of the adatom (Reference 9. Reprinted with permission of J. Vac. Sci. Technol.).

of these pinning levels has not been unambiguously established. Figure 1.5 shows the defect levels for different III-V semiconductors as predicted by the UDM. It has been pointed out that the UDM can only give a rough approximation of the SB.[34,35] Since it was proposed in 1979, the UDM has undergone many refinements. Including adjustments for the effects of metal electronegativity[34], thermal aging[35] and interface reactions.[36,37]

Although the UDM has been successful in explaining experimental results on many M/III-V interfaces, there exists significant criticism

regarding this model in general. As pointed out by Tersoff[38] there is no evidence that the experimentally observed pinning at submonolayer coverage is associated with defect levels. Calculations by Zur et al [References 39,40] indicate that at the M/S interface, because of screening by metal, a defect density of ~$10^{14}cm^{-2}$ is required to pin the fermi level. Such a high density of defect at the M/S interface is rarely observed. Another problem with the UDM is the inconsistency of SB heights measured for n and p type materials for submonolayer and thick coverage. According to the UDM, the difference in the pinning levels between n and p type materials is ~0.2 eV. This difference has been observed for small metal coverage (submonolayer to a few monolayers). But no such difference has been measured for real diodes with thick metal overlayer (1000 Å). Instead, experimental results obtained by I-V measurements of diodes with thick (>1000 Å) overlayers reveal that the sum of the SBs for n and p type semiconductors is always equal to the band gap of the semiconductor.

1.2.2 Effective work function model (EWFM)

Another model proposed to explain the experimentally observed SB values is the effective work function model (EWFM) by Freeouf and Woodall.[14,41-43] The EWFM is basically a modification of Schottky's original model. The EWFM suggests that the insensitivity of the barrier heights to the metal work function is not due to fermi level pinning by interface states but is the result of the existence of an interface layer with a work function different from that of the metal.

Schottky's theory on barrier heights at M/S interface can therefore be used to explain the experimental data by replacing the work function of the metal with an effective work function ξ_{eff} of microclusters of one or more interface phases resulting from chemical reactions during metal deposition. According to the EWFM, the barrier height can then be expressed as $\xi_b = \xi_{eff} - \chi_s$. Using thermodynamic data, Freeouf and Woodall suggested that excess anions of the compound semiconductor are always present at the M/S interface due to one or both of the following reactions:

Anion oxide + Compound Semiconductor ⟶ Anion + Cation oxide

M + Compound Semiconductor ⟶ (Anion or M-Anion complex) + (M-Cation)

Therefore the effective work function ξ_{eff} is due mainly to the work function of the anion, ξ_{anion}. Freeouf and Woodall found reasonably good agreements of the EWFM with experimental barrier heights of Au on various different compound semiconductors.[14,43] However, the large uncertainty in the values of the work function of the anions reported by different sources, puts the good match between experimental and theoretical barrier heights as predicted by EWFM in doubt.

Despite its limited success in predicting the SB of Au on III-V semiconductors, the EWFM contradicts some recent experimental findings on M/S interfaces. Results on metal/GaAs and metal/InP systems with surface sensitive techniques (PES) and soft x-ray photoemission spectroscopy (SXPS) as well as analytical techniques such as transmission electron microscopy (TEM), Rutherford backscattering spectrometry (RBS)

and x-ray diffraction (XRD) demonstrate that most metals react with the anion of the semiconductor substrate resulting in the diffusion of mobile cations to the surface. Therefore the effective work function is expected to be that of the metal-anion phase instead of that of the anion predicted by the EWFM.

1.2.3 Metal induced gap states (MIGS) model

In 1965 Heine[10] proposed that pinning of fermi level at M/S interface is established by states induced at the interface by the decay of the tails of the metal wave functions into the forbidden gap of the semiconductor. These states came to be known as "metal induced gap states" (MIGS). The MIGS model has been further developed by Louie, Chelikowsky and Cohen[11] who used self-consistent pseudopotential calculation and predicted the pinning at an energy approximately equal to the experimentally observed value. Recently, Tersoff[12] further refined the model and suggested that the fermi level at the M/S interface is pinned at or near the energy E_B where the gap states cross over from predominantly valence- to conduction-band character. Hence this pinning behavior is determined primarily by the intrinsic property of the semiconductor and is rather independent of the deposited metal. The behavior of the M/II-VI interfaces as "true" Schottky barriers (i.e. $\xi_b = \xi_m - X$) can also be explained by this model. Because the very short MIGS decay lengths in the more ionic II-VI semiconductors (e.g. 1.5 Å for ZnS comparing to 3 Å for the more covalent Si and GaAs) are unable to screen the effect of metal electronegativity, the SB is

expected to be more dependent on the metal work function for these interfaces. The MIGS model therefore suggests that there are two contributions to the SB at the M/S interface. First, there is a short range contribution related to the surface dipole due to the M/S electronegativity difference or the more subtle details of bonding. Second, there is an additional dipole due to metallic screening by MIGS which tends to pin the fermi level so as to maintain local charge neutrality. The penetration depth of the MIGS determines which one of these dominates.

PES data on many M/S systems show that SB is well established at submonolayer metal coverage. These data are in conflict with the MIGS model because at such a low coverage the overlayer is not yet metallic and therefore pinning in these cases cannot be due to MIGS. Since MIGS are expected to decay much more quickly in oxides than in semiconductors, no MIGS should be found in the semiconductor of a metal/oxide/semiconductor structure. However, experimental results show that a structure with ~20 Å of oxide on semiconductor has interface fermi level pinned at a level identical to that of a M/S intimate contact. Moreover, the penetration depth of MIGS is typically a few Å while for most M/GaAs contacts, the interfaces are non-abrupt with lateral non-uniformity more than ~10 Å. The effectiveness of MIGS for pinning the M/GaAs interface fermi level is therefore questionable. These apparent inconsistencies between the MIGS model and some of the experimental results are still unresolved to date.

1.2.4 Amphoteric native defect model

Recently, Walukiewicz[13] proposed a microscopic model to explain the M/GaAs SB formation using the thermodynamic properties of the native defects and the electronegativity of the overlayer metal. Since it has been known experimentally that there is always an As rich layer of GaAs at the M/GaAs interface[37,44], it is expected that native defects are formed in order to accommodate this non-stoichiometry. For As rich GaAs, it has been shown that two types of native defects dominate: a gallium vacancy V_{Ga} which is an acceptor and (As_{Ga}, V_{As}) complex which is a donor. These two defects are structurally similar and the energy required for the transformation of one type to another is very small. Therefore, the defect reaction $V_{Ga} \rightleftharpoons (As_{Ga}, V_{As})$ depends strongly on the location of the fermi level E_f. Walukiewicz suggested that for $E_f < E_v + 0.5$ eV, the $(As_{Ga}, V_{As})^{3+}$ donor is the stable defect, while for $E_f > E_v + 0.7$ eV, the acceptor V_{Ga}^{3-} is stable. The SB formed is then controlled mainly by the balance of the two types of defects which in turn depends on the type of the semiconductor.

The effects of the electronegativity of the overlayer metal are also considered in this model. For n-type III-V semiconductors, Walukiewicz argued that metals with electronegativity $X_m > X_{GaAs}$ (the effective electronegativity of GaAs) induce a downward shift in E_f by removing electrons from GaAs and the fermi level is thus pinned at the donor level (0.52 eV) and the $\phi_{bn} \approx 0.92$ eV. For metals with $X_m < X_{GaAs}$, the fermi level is shifted toward the upper acceptor level, $E_v + 0.7$ eV, and the barrier heights are pinned at 0.72 eV. Therefore a total

barrier height change of 0.2 eV is expected for n-GaAs Schottky diodes. For the case of $X_m \approx X_{GaAs}$, no charge transfer occurs and the fermi level will be located at the energy at which defect formation energies for the two types of native defects are equal, i.e. ξ_{bn}=0.82 eV.

Figure 1.6 shows experimental data for SB heights for metals with different electronegativities. The lines in the figure represent the theoretical values of barrier heights given by this model. Good agreements between theoretical and experimental results are observable. However, for rare earth metals with extremely low electronegativities, the SBs are found to be around 0.85 eV [Reference 45] instead of 0.72eV predicted by this model. This apparent discrepancy may be the result of the fact that these data were obtained on GaAs substrates which had been annealed at 500°C in order to remove the native oxide before metal deposition. This process may have changed the interface stoichiometry to such an extent that it is no longer As rich[46]. It is also possible that other mechanisms dominate for metals with such low electronegativities. Since this is a relatively new model, much more work has to be done in order that it can be firmly established. Walukiewicz also suggested that the validity of this model can be extensively tested on other compound semiconductors which also form similar native defects at the interface.

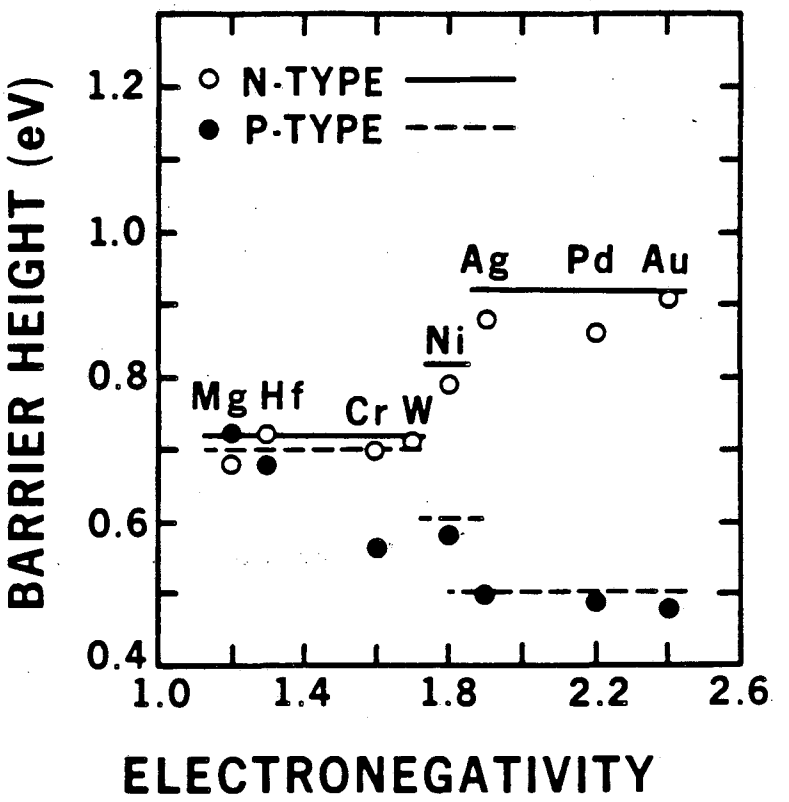

XBL 868-3142

Figure 1.6 Schottky barrier height for n-type and p-type GaAs as functions of metal electronegativity. The lines in the figure represent theoretical values of barrier heights given by the amphoteric native defect model (Reference 13).

1.3 Metal/Semiconductor Interface Reactions

In early semiconductor devices where the device dimension was relatively large (typically larger than a few microns), the only major requirements on contact materials were good adhesion, desirable barrier height, low electrical resistance and high corrosion resistance. Aluminum satisfies adequately all these requirements and was used as

the most common metal contact to "large" silicon devices. It is known that at relatively low temperatures (~400°C) Al tends to penetrate locally into the Si substrate forming electrically shorted paths through the junction.[47-49] Moreover, heat treatment of the Al/n-Si contact results in the incorporation of Al in the n-Si substrate creating a p-Si layer at the interface[50-55]. Therefore the contact exhibits p-n junction instead of a Schottky junction characteristics. But for early devices which had relatively large p-n junction depth (several microns) beneath the Al contact, these undesirable properties posed no significant problems to the overall electrical behavior of the devices.

With the advent of large scale integration, individual device dimension has become smaller resulting in more stringent constraints on contact metallization. Furthermore, with the miniaturization of devices, junction depths have become shallower. Therefore the Al penetration into the Si could no longer be tolerated since it caused serious junction shorts in the devices. The search for other contact materials for the development of high density integrated circuits led to the comprehensive investigation of the metal/silicon interface metallurgy for the last twenty years. Brief reviews on the present knowledge of metal/Si and metal/GaAs contact reactions will be given in the following sections.

1.3.1 Metal/Si contact reactions-silicide formation

In the last twenty years, the intense research in the area of metal/Si interface interactions led to the development of a new class of contact materials: the transition metal silicides. The silicides are commonly formed by a solid phase reaction between a single crystal Si wafer and a transition metal layer at temperatures lower than half of the lowest eutectic temperature of the corresponding metal-Si equilibrium phase diagram. Most of the transition metal silicides exhibit metallic conductivity and behave as Schottky contacts to Si. Since a silicide is formed as a result of a solid phase reaction between a metal layer and the Si substrate, the original metal/Si interface is consumed leading to a new silicide/silicon interface which is abrupt and free from oxide and other contaminations. Moreover, silicides usually show good mechanical adhesion to the Si substrate. Table I shows a summary of the experimental results obtained from solid phase reactions between a metal layer on Si after conventional furnace annealing. Recently other processing techniques such as laser and electron beam annealing and ion beam mixing have been used in the formation of silicides with varying stoichiometries. However, only results on the furnace annealing experiments will be discuss in this review.

In general, the transition metal silicides can be broadly divided into three classes: metal-rich silicide (M_2Si), monosilicide (MSi) and disilicide (MSi_2). Metals which react with Si to form metal-rich silicide as the first phase of reaction are normally near noble metals

Table I A summary of silicide formations [a)]

Metal	Silicide	Formation Temp. (°C)	Activation Energy(eV)	Growth Rate[(b)]	Crystal Structure	Moving Species	Heat of Formation - H_f (kcal/metal atom)
Co	Co_2Si	350-500	1.5	D	Orthorhomb.	Co	13.8
	CoSi	400-500	1.9	D	Cubic	-	24.0
	$CoSi_2$	550	-	-	Cubic	-	24.6
Ni	Ni_2Si	200-350	1.5	D	Orthorhomb.	Ni	17.7
	NiSi	350-750	1.4	R	Orthorhomb.	Ni	20.5
	$NiSi_2$	≥750	-	N	Cubic	-	20.85
Pd	Pd_2Si	100-700	1.3-1.5	D	Hexagonal	Pd,Si	28.7
	PdSi	≥700	-	-	Orthorhomb.	-	34.0
Pt	Pt_2Si	200-500	1.5	D	Tetragonal	Pt	25.5
	PtSi	≥300	1.6	D	Orthorhomb.	-	40.2
Rh	RhSi	350-425	1.95	D	Cubic	-	29.2
	Rh_4Si_5	825-850	-	N	Monoclinic	-	-
	Rh_3Si_4	925	-	N	Orthorhomb.	-	-
Ir	IrSi	400-600	1.9	D	-	-	32.0
	$IrSi_{1.75}$	500-950	≈2.1	D	Monoclinic	-	-
	$IrSi_3$	~1000	-	N	Hexagonal	-	-

Table I (cont.)

Fe	FeSi	450-550	1.7	D	Cubic	Si	17.6
	$FeSi_2$	550	-	-	Tetragonal	Si	19.4
Ru	Ru_2Si_3	450	1.8	D	Orthorhomb.	-	-
Os	Os_2Si_3	~600	1.8	D	Tetragonal	-	-
	$OsSi_2$	~750	-	N	Orthorhomb.	-	
Cr	$CrSi_2$	450	1.7	R	Hexagonal	-	29.4
Mo	$MoSi_2$	525	3.2	R	Tetragonal	Si	26.0
W	WSi_2	650	3	D,R	Tetragonal	Si	22.2
V	VSi_2	600	2.9,1.8	D,R	Hexagonal	Si	75
Nb	$NbSi_2$	650	-	-	Hexagonal	-	33
Ta	$TaSi_2$	650	-	-	Hexagonal	Si	28.5
Ti	TiSi	500	-	-	Orthorhomb.	Si	31
	$TiSi_2$	600	-	D,R	Orthorhomb.	Si	32
Zr	$ZrSi_2$	700	-	-	Orthorhomb.	-	38
Hf	HfSi	550-700	2.5	D	Orthorhomb.	Si	34
	$HfSi_2$	750	-	-	Orthorhomb.	-	54

a) Data taken from references 64, 65, 67 and 69.
b) D≡diffusion controlled growth; R≡interface reaction comntrolled growth and N≡nucleation controlled growth.

except for Mg. Metals which form disilicide with Si as the initial phase include most of the refractory metals. As can be seen in Table I, metal-rich silicides have temperatures of formation in the range of 200 to 400 °C, with growth rates proportional to the square root of the annealing time, i.e. parabolic or diffusion controlled growth rates with formation energy ~1.5 eV. For monosilicide, the formation temperature is higher than that for metal-rich silicides and lies between 350 °C and 500 °C. An exception is the formation of PdSi from Pd_2Si occurring at above 700 °C. This implies that Pd_2Si is an extremely stable phase, a fact further supported by the high heat of formation (ΔH_f=28.7 kcal/metal atom) of this phase. Parabolic reaction rates are also observed for monosilicide growth with a formation energy of 1.6-2.5 eV. The formation of disilicide usually starts at around 500 °C except for $CrSi_2$ which already forms at 450 °C. Formation energies for disilicide lie in the range 1.7 to 3.2 eV. The growth for refractory metal disilicides is, however, linear with the annealing time, i.e. reaction controlled growth, in the early stage of reaction.

A notable exception to the general behavior mentioned above is the formation of rare earth metal (RE) silicides. For RE (Gd, Dy, Ho, Er, Y, La and Tb) silicide, the first phase has been observed to be forming very rapidly in a narrow temperature range of between 325 and 400 °C [References 56-58]. There is, however, no general agreement on the composition of this first phase. Baglin et al[56] showed that Y, Tb and Er form a first phase RE Si_{2-n} with n≈0.3. From experimental data on Gd, Dy, Ho, Er, Y and La, Thompson et al[58] concluded that disilicide is

the first and only phase formed in a RE/Si systems. Thompson and Tu[59] observed the conversion of 3000 Å of Er on Si substrate to $ErSi_2$ in 15 minutes at 400 °C. This rapid growth rate is characteristic for all RE silicides and leads to the conclusion that a nucleation controlled rather than a diffusion controlled process dominates in RE metal/Si reactions. Therefore, instead of the layer by layer growth observed for the growth of most silicides, RE silicides have been found to nucleate at a few spots at the interface and grow as isolated islands. The resultant RE silicide layer, however, has a uniform and sharp interface with the Si substrate.

Compositions of some silicides of osmium, ruthenium, rhodium and iridium do not fall into the three general classes. For pure Ru on Si substrate, Ru_2Si_3 starts to grow at ~450 °C and has been found to be the only phase formed in this system[60]. Os/Si reactions result in the formation of two phases: first the formation of Os_2Si_3 at ~600 °C, then the nucleation of $OsSi_2$ at ~750 °C [Reference 60]. The formations of both, Ru_2Si_3 and Os_2Si_3, follow diffusion controlled mechanisms with an activation energy ~1.8 eV. The formation of $OsSi_2$ which occurs again in a very narrow temperature range is believed to be nucleation controlled. The Rh/Si system starts reacting following the general trend of monosilicide formation at 350 °C according to diffusion controlled kinetics. At high temperatures, ~ 800 °C and 925 °C, it forms Rh_4Si_5 and Rh_3Si_4, respectively following a mechanism controlled by nucleation [References 61-63]. Similar behavior is observed in the Ir/Si reaction in which $IrSi_{1.75}$ and $IrSi_3$ are formed following the monosilicide

growth. In this case, the formation of $IrSi_{1.75}$ still follows diffusion controlled kinetics while the formation of the final phase $IrSi_3$ is controlled by nucleation[64].

As far as the composition of the first phase of formation is concerned, a general trend can be observed in silicide formation. The Si content in the silicide increases as the position of the metal in the periodic table moves from right (i. e. Ni, Pd and Pt) to left (i.e. V, Nb, Ta, Mo and W). Three types of reaction kinetics are observed for transition metal silicide formation: diffusion controlled for all metal-rich and mono- silicides; nucleation controlled for RE silicide and most Si-rich silicides which form at high temperatures (~800 °C) and reaction rate controlled for refractory metal disilicide. Issues such as electrical behavior, mechanical properties and the applications of silicides in various aspects of Si VLSI technology are not included in this review. Readers interested in these areas are referred to books and review articles published recently[65-70].

1.3.2 Metal/GaAs contact reactions

The technological importance of GaAs for the development of ultra high speed ICs as well as novel electronic and photonic devices has been discussed at the beginning of this chapter. Despite the interests in this material, neither the electrical nor the metallurgical properties at the metal/GaAs interface are well understood. This is mainly because of the complexity of the multi-component (at least three) system of the metal/GaAs interface as well as the structural and

electrical properties of the III-V surface involved. Reports on the interface solid phase reactions between metal thin films and GaAs substrate have been concentrated on certain metals such as Au, Pt and W. Pt and Au have been used traditionally as contacts to GaAs IMPATT (impact ionization avalanche transit time) diodes for microwave applications[71]. The Au/Pt/GaAs structure has been employed with the Au layer acting as a bonding layer to the heat sink[72,73]. This structure was then found to be unacceptable due to the migration of Au atoms through the Pt layer to the GaAs interface during device operation. A high temperature stable "inert" layer of tungsten was introduced between the Pt and Au layers as diffusion barrier[74]. The interests in the Au/GaAs system has also been due to the success with the Au based alloyed ohmic contact to GaAs introduced by Braslau et al[21]. Unlike the metal/Si case where exhaustive data have been obtained, only preliminary results on a few systems are available for metal/GaAs interface reactions. Therefore no systematics for such reactions have been established to date.

Based on the limited data available, a general trend for metal/GaAs reaction has been proposed[75]. Sinha and Poate suggested that the different types of reaction observed for metal/GaAs interface can be rationalized by the electronegativity difference between the various metals and Ga and As. They divided the metals into three groups based on their electronegativity: group I consists of the noble metals (group IB in the periodic table) which are very electronegative; group II consists of the near noble metals (group VIII metals in the periodic

table) which are quite electronegative and group III consists of the electropositive refractory metals (group IVB, VB, VIB).

According to Sinha and Poate, the group I metal/III-V reaction is characterized by the outdiffusion of the electropositive cation (Ga in the case of GaAs). This has been illustrated in the Au/GaAs system [References 76,77]. The reaction of the Au/GaAs interface is believed to proceed as follows: 1. the thermal dissociation of GaAs at the interface, 2. the liberated Ga atoms diffuse to the surface and propagate into the gold, and 3. the vacancies left behind by the Ga are filled by the indiffusing Au atoms. The outdiffusion of the Ga atoms to the surface forming Ga_2O_3 is due to the effect of the increase in electronegativity in the sequence Ga→As→Au→O. Reaction at a group II metal/GaAs interface results in the formation of chemical phases in a layered structure. The formation of stable phases M-III and M-V is due to the strong tendency of these metals to attain the stable d^{10} electronic structure through electron transfer. The layered structure of different phases is the result of the outdiffusion of the electropositive cation released through thermal dissociation at the M/S interface. This can be illustrated with the reactions of Pt/GaAs.[78-81] The large electronegativity difference between Ga and Pt induces the outdiffusion of the Ga atoms into the Pt overlayer at low temperatures (<300°C). At ~350°C, Pt forms the stable compound $PtAs_2$ at the interface releasing more Ga atoms. As more and more Ga diffuse into the Pt, a stable Pt-Ga phase is formed. For group III metals, which are rather electropositive, the electronegativity effect is minimum. The group

III metal/III-V interface is therefore relatively inert. This has been shown for the W/GaAs interface[77] at which no interdiffusion is observed after annealing at 500°C for 2 hours in vacuum.

Recently, with the development of new non-alloyed ohmic contacts and new processing techniques for GaAs electronic and photonic devices, metallurgy at the interfaces of GaAs and both, near noble and refractory metals, has attracted much attention. In fact in the last five years, a number of studies have been carried out for the solid phase reaction between GaAs substrates and thin film metals such as Ti, Mo, Cr, W, Co, Pd and Pt. Table II shows a summary of the thermally induced solid phase reactions at metal/GaAs interfaces. The results obtained in the present investigation are not included in this summary. It is obvious that most of these data have been obtained in the 1980s. These recent results show that the model proposed by Sinha and Poate which should explain most metal/III-V reactions, is not satisfactory. One example is the case of Ti/GaAs[100] in which the formation of a layered structure of Ti-Ga/Ti-As/GaAs is observed at ~450°C despite the fact that Ti is even more electropositive than W.

It has been mentioned in section 1.1 that a large quantity of data on metal/GaAs interfaces in UHV condition investigated by surface sensitive techniques is available. These experiments have been performed on the M/S systems with ultra thin metal coverage (submonolayer to a few monolayers). At this metal coverage, the interface reaction is expected to be thermodynamically and kinetically very different from that of the thin film case (with film thickness

~100-1000 Å). While these experimental data are essential to the fundamental understanding of the physics of surfaces and interfaces, their significance for the metallurgy of metal/GaAs interfaces is limited. Therefore it is the purpose of this thesis to take a materials science approach in a compre-hensive investigation of the interface reactions of metal/GaAs systems in a systematic fashion.

Table II A summary of the solid phase reactions of metal/GaAs contacts reported in the literature.

Metal	Reaction Temp. (°C)	Reaction Rate	Stable Phases	Intermediate Phases	Phase Stratification	Activation Energy(eV)	References
Au	≥250	-	$AuGa_2$	-	No	-	76-78
Ni	≥200	-	NiGa, NiAs	Ni_xGaAs (x=2~3)	No	-	23, 82-85
Pd	200	-	PdGa, PdAs	Pd_xGaAs (x=2~4)	No	-	86-91
Pt	≥300	$\sim t^{1/2}$	PtGa, $PtAs_2$	Pt_3Ga	Yes	1.6, 2.1	78-81
Co	≥300	$\sim t^{1/2}$	CoGa, CoAs	Co_2GaAs	No	1.68	92, 93
Rh	450	-	RhGa, RhAs	-	Yes	-	94
Cr	>450	-	Cr_2X (X=Ga, As or both	-	-	-	95, 96
Mo	700	-	Mo_3GaAs_2, Mo_5As_4	Mo_3Ga	-	-	97, 98
W	900	-	-	-	-	-	78, 99
Ta	>450	-	-	-	-	-	95, 96
Ti	480	$\sim t^{1/2}$	Ti_5Ga_4, Ti_5As_3	Ti_2Ga_3, TiAs	Yes	1.7	100, 101

REFERENCES TO CHAPTER 1

1. W. Schottky, Naturwiss. **26**, 843 (1938); Z. Phys. **113**, 367(1939); and Z. Phys. **118**, 539 (1942).

2. N. F. Mott, Proc. Cambridge Phil. Soc. **34**, 568 (1938).

3. B. Davydov, J. Phys. USSR **1**, 167 (1939); and J. Phys. USSR **4**, 335 (1941).

4. H. A. Bethe, MIT Radiat. Lab. Rep. 43-12 (1942).

5. For discussions on the effective Richardson constant, see for example S. M. Sze, *Physics of Semiconductor Devices*, p. 256, Wiley, New York, 1981.

6. V. L. Rideout, Solid-State Electron. **18**, 541 (1975).

7. J. Bardeen, Phys. Rev. **71**, 717 (1947).

8. L. J. Brillson, Surf. Sci. Rep. **2**, 123 (1982).

9. W. E. Spicer, P. W. Chye, P. R. Skeath, C. Y. Su, and I. Lindau, J. Vac. Sci. Technol. **16**, 1422 (1979); and W. E. Spicer, I. Lindau, P. Skeath, C. Y. Su, and P. Chye, Phys. Rev. Lett. **44**, 4204 (1980).

10. V. Heine, Phys. Rev. **A138**, 689 (1965).

11. S. G. Louie and M. L. Cohen, Phys. Rev. **B13**, 2461 (1976); S. G. Louie, J. R. Chelikowsky and M. L. Cohen, J. Vac. Sci. Technol. **13**, 790 (1976); and S. G. Louie, J. R. chelikowsky and M. L. Cohen, Phys. Rev. **B15**, 2154 (1977).

12. J. Tersoff, Phys. Rev. Lett. **52**, 465 (1984).

13. W. Walukiewicz, 14th Conf. on the Phys. and Chem. of Semicond. Interfaces, Salt Lake City, Utah, Jan. 26-29, 1987.

14. J. L. Freeouf and J. M. Woodall, Appl. Phys. Lett. **39**, 727 (1981).

15. K. Kajiyama, Y. Mizushima and S. Sakata, Appl. Phys. Lett. **23**, 4581 (1973).

16. J. H. Walpole and K. M. Nill, J. Appl. Phys. **42**, 5609 (1971).

17. C. A. Mead and W. G. Spitzer, Phys. Rev. Lett. **10**, 471 (1963).

18. See for example, S. M. Sze, *Physics of Semiconductor Devices*, p.97, Wiley, New York, 1981.

19. N Braslau, J. Vac. Sci. Technol. **19**, 803 (1981).

20. W. J. Bondville and T. C. McGill, J. Vac. Sci. Technol. **83**, 1192 (1985).

21. N. Braslau, J. B. Gunn and J. L. Staples, Solid State Electron. **10**, 381 (1967).

22. G. Y. Robinson, J. Vac. Sci. Technol. **13**, 884 (1976).

23. M. Ogawa, J. Appl. Phys. **51**, 406 (1980).

24. T. S. Kuan, P. E. Barson, T. N. Jackson, H. Rupprecht and E. L. Wilkie, J. Appl. Phys. **54**, 6952 (1983).

25. W. T. Anderson, Jr., A. Christou and J. E. Davey, J. Appl. Phys. **49**, 2998 (1978).

26. H. R. Grinolds and G. Y. Robinson, Solid State Electron. **23**, 973 (1980).

27. E. D. Marshall, W. X. Chen, C. S. Wu, S. S. Lau and T. F. Kuech, Appl. Phys. Lett. **47**, 298 (1985).

28. S. R. Smith and J. S. Solomon, Mat. Lett. **3**, 294 (1985).

29. K. Tsutsui and S. Furukawa, J. Apll. Phys. **56**, 560 (1984).

30. R. A. Stall, C. E. C. Wood, K. Board, N. Dandekar, L. F. Eastman and J. Devlin, J. Appl. Phys. **52**, 4062 (1981).

31. J. Devlin, C. E. C. Wood, R. A. Stall and L. F. Eastman, Solid State Electron. **23**, 823 (1980).

32. J. M. Woodall, J. L. Freeouf, G. D. Pettit, T. Jackson and P. Kirchner, J. Vac. Sci. Technol. **19**, 626 (1981).

33. A. A. Lakhani, J. Apll. Phys. **56**, 1888 (1984).

34. M. D. Williams, T. Kendelewicz, R. S. List, N. Newman, C. E. McCants, I. Lindau and W. E. Spicer, J. Vac. Sci. Technol. **B3**, 1202 (1985).

35. I. Lindau and T. Kendelewicz, CRC Crit. Rev. Solid States and Mat. Sci. **13**, 27 (1986).

36. N. Newman, K. K. Chin, W. G. Petro, T. Kendelewicz, M. D. Williams, C. E. McCants and W. E. Spicer, J. Vac. Sci. Technol. **A3**, 996 (1985).

37. W. Mönch, Surf. Sci. **132**, 92 (1983).

38. J. Tersoff, J. Vac. Sci. Technol. **B3**, 1157 (1985).

39. A. Zur, T. C. McGill and D. L. Smith, Phys. Rev. **B28**, 2060 (1983).

40. A. Zur and T. C. McGill, J. Vac. Sci. Technol. **B2**, 440 (1984).

41. J. M. Woodall and J. L. Freeouf, J. Vac. Sci. Technol. **19**, 794 (1981).

42. J. M. Woodall and J. L. Freeouf, J. Vac. Sci. Technol. **B2**, 510 (1984).

43. J. M. Woodall and J. L. Freeouf, J. Vac. Sci. Technol. **21**, 574 (1982).

44. Z. Liliental-Weber, E. R. Weber, N. Newman, W. E. Spicer, R. Gronsky and J. Washburn, *Proc. XIV Intern. Conference on Defects in Semiconductors*, (Paris, 1986) in press.

45. J. R., Waldrop, Appl. Phys. Lett. **46**, 864 (1985).

46. W. Walukiewicz, private communications.

47. P. A. Totta and R. P. Sopher, IBM J. Res. Dev. **13**, 226 (1967).

48. I. E. Price and L. A. Berthond, Solid State Electron. **16**, 1303 (1973).

49. C. H. Lane, Metall. Trans. **1**, 713 (1970).

50. J. O. McCaldin and H. Sankur, Appl. Phys. Lett. **20**, 171 (1972).

51. J. Sankur, J. O. McCaldin and J. Devaney, Appl. Phys. Lett. **22**, 64 (1973).

52. G. Ottaviani, D. Sigurd, V. Marello, J. W. Mayer and J. O. McCaldin, J. Appl. Phys. **45**, 1730 (1974).

53. D. Sigurd, G. Ottaviani, H. J. Arnal and J. W. Mayer, J. Appl. Phys. **45**, 1740 (1974).

54. J. S. Best and J. O. McCaldin, J. Appl. Phys. **46**, 4071 (1976).

55. R. L. Boatright and J. O. McCaldin, J. Appl. Phys. **47**, 2260 (1976).

56. J. E. Baglin, J. M. d'Heurle and C. S. Petersson, Appl. Phys. Lett. **36**, 594 (1980).

57. F. M. d'Heurle and P. S. Gas, J. Mat. Res. **1**, 205 (1986).

58. R. D. Thompson, B. Y. Tsaur and K. N. Tu, Appl. Phys. Lett. **38**, 535 (1981).

59. R. D. Thompson and K. N. Tu, Thin Solid Films **93**, 265 (1982).

60. C. S. Petersson, J. E. Baglin, F. M. d'Heurle and S. J. LaPlaca, J. Appl. Phys. **53**, 4866 (1982).

61. J. M. Andrews and M. P. Lepselter, Solid State Electron. **13**, 1011 (1970)

62. O. J. Coe, E. H. Rhoderick, P. H. Gerzon and A. W. Tinsley, Inst. Phys. Conf. Ser., London and Bristol **22**, 74 (1974).

63. C. S. Petersson, R. Anderson, J. E. Baglin, J. Dempsey, W. Hammer, F. M. d'Heurle and S. J. LaPlaca, J. Appl. Phys. **51**, 373 (1980).

64. C. S. Petersson, J. E. Baglin, W. Hammer, F. M. d'Heurle, T. S. Kuan, I. Odhomari, J. deSousa Pires and P. A. Tove, J. Appl. Phys. **50**, 3357 (1979).

65. K. N. Tu and J. M. Mayer, "Silicide Formation" in *Thin Film-Interdiffusion and Reactions*, eds. J. M. Poate, K. N. Tu and J. W. Mayer, Chapter 10 (Wiley, New York, 1978).

66. G. Ottavianni, J. Vac. Sci. Technol. **16**, 1112 (1979).

67. F. Mohammad, Solid State Electron. **24**, 65 (1981).

68. S. P. Murarka, *Silicide for VLSI Applications* (Academic Press, New York, 1983).

69. M-A. Nicolet and S. S. Lau in *VLSI Electronics, Microstructure Science*, eds. N. G. Einspruch and G. B. Larrabee (Academic Press, New York, 1983).

70. B. L. Sharma, "Fabrication and Characterization of Metal-Semiconductor Schottky Barrier Junctions" in *Metal-Semiconductor Schottky Barrier Junctions and Their Applications*, ed. B. L. Sharma (Plenum Press, New York, 1984).

71. See for example S. M. Sze, *Physics of Semiconductor Devices*, p.566 (Wiley, New York, 1981).

72. J. C. Irvin, D. L. Coleman, W. A. Johnson, I. Tatsuguchi, D. R. Kecker and C. N. Dunn, Proc. IEEE **59**, 1212 (1971).

73. W. R. Wisseman, D. W. Shaw, R. L. Adams and T. E. Hasty, IEEE Trans. Electron. Devices **ED21**, 317 (1974).

74. G. E. Mahony, Appl. Phys. Lett. **27**, 613 (1975).

75. A. K. Sinha and J. M. Poate, "Metal-ompound Semiconductor Reactions" in *Thin Films-Interdiffusion and Reactions*, eds. J. M. Poate, K. N. Tu and J. W. Mayer, Chapter 11 (Wiley, New York, 1978).

76. J. Gyulai, J. W. Mayer, V. Rodriquez, A. Y. C. Yu and H. J. Gopeu, J. Appl. Phys. **42**, 3578 (1971).

77. G. Y. Robinson, J. Vac. Sci. Technol. **13**, 884 (1976).

78. A. K. Sinha and J. M. Poate, Appl. Phys. Lett. **23**, 666 (1973).

79. V. Kumar, J. Phys. Chem. Solids **36**, 535 (1975).

80. C. C. Chang, S. P. Murarka, V. Kumar and G. Quintana, J. Appl. Phys. **46**, 4237 (1975).

81. C. Fontaine, T. Okumura and K. N. Tu, J. Appl. Phys. **54**, 1404 (1983).

82. A. Lahav and M. Eizenberg, Appl. Phys. Lett. **45**, 256 (1984).

83. A. Lahav, M. Eisenberg and Y. Komen, Mat. Res. Soc. Symp. Proc. **37**, 641 (1985).

84. T. Sands, V. G. Keramidas, J. Washburn and R. Gronsky, Appl. Phys. Lett. **48**, 402 (1986).

85. A. Lahav, M. Eisenberg and Y. Komen, J. Appl. Phys. **60**, 991 (1986).

86. P. Oelhafen, J. L. Freeouf, T. S. Kuan, T. N. Jackson and P. E. Batson, J. Vac. Sci. Technol. **B1**, 588 (1983).

87. T. S. Kuan, Mat. Res. Soc. Sym. Proc. **31**, 143 (1984).

88. T. S. Kuan, J. L. Freeouf, P. E. Batson and E. L. Wilkie, J. Appl. Phys. **58**, 1519 (1985).

89. T. Sands, V. G. Keramidas, R. Gronsky and J. Washburn, Mat. Lett. **3**, 409 (1985).

90. T. Sands, V. G. Keramidas, A. J. Yu, K. M. Yu, R. Gronsky and J. Washburn, Mat. Res. Soc. Proc. **54**, 367 (1986).

91. T. Sands, V. G. Keramidas, R. Gronsky and J. Washburn, Thin Solid Films **136**, 105 (1986).

92. A. J. Yu, G. J. Galvin, C. J. Palmstrom and J. W. Mayer, Appl. Phys. Lett. **47**, 934 (1985).

93. A. J. Yu, G. J. Galvin, J. W. Mayer, C. J. Palmstrom, T. Sands and C. C. Chang, presented at the 1986 Spring Meeting of Mat. Res. Soc. April 17, 1986, Palo Alto, Ca.

94. C. J. Todd, J. D. Speight, G. W. B. Ashwell and Heckingbottom, ECS Extended Abstract No.119, Spring Meeting, Toronto (1975), p.274.

95. S. D. Mukherjee, D. V. Morgan, M. J. Howes, J. G. Smith and P. Brook, J. Vac. Sci. Technol. **16**, 134 (1979).

96. S. D. Mukherjee, C. J. Palmstrom and J. G. Smith, J. Vac. Sci. Technol. **17**, 904 (1980).

97. K. Suh, H. K. Park and K. L. Moazed, J. Vac. Sci. Technol. **B1**, 365 (1983).

98. P. Ling, J-K Chang, M-S Lin and J-C Lou, Mat. Rers. Soc. Symp. Proc. **48**, 137 (1985).

99. K. Matsumoto, N. Hashizume, H. Tanoue and T. Kanayama, Jpn. J. Appl. Phys. **21**, L393 (1982).

100. O. Wada, S. Yanagisawa and H. Takanashi, Appl. Phys. Lett. **29**, 263 (1976).

101. A. K. Sinha, T. E. Smith, M. H. Read and J. M. Poate, Solid State Electron. **19**, 489 (1976).

Chapter 2 CHARACTERIZATION TECHNIQUES

The major groups of technique for the characterization of thin film interactions and interdiffusion are based on charged particle energy loss such as Rutherford backscattering spectrometry (RBS) and on sputter sectioning of the sample. In conventional RBS, a collimated beam of He or H ions with energies in the MeV range is incident on the target and the projectiles backscattered from the target are collected and energy analyzed by a solid state detector. Depth information of the sample is obtained from the energy loss of the particles on their inward and outward paths. Other than the minimum beam damage to the crystal lattice on single crystals, there is no physical damage to the sample. Techniques employing sputter sectioning are usually carried out with a keV heavy ion beam using for example Ar. The sample is analyzed layer by layer through the analysis of either the surface of the specimen with a surface sensitive technique such as Auger electron spectroscopy (AES) or the sputtered species as in secondary ion mass spectrometry (SIMS). The sectioning techniques physically destroy the sample which makes subsequent complementary analysis of the same sample with different techniques impossible. The fundamental problems associated with SIMS and AES are, however, not only their destructive nature but also their inability of quantitative analysis without the use of standards. Moreover, accurate depth information cannot be obtained by sputtering because of preferential sputtering of different materials at the interface.

Due to the reasons mentioned above, charge particle energy loss techniques are used as the major tool to investigate thin film metal/GaAs interface in this work. Experiments using both conventional RBS with ^{4}He projectiles and heavy ion RBS (HIRBS) with ^{16}O projectiles have been carried out. Measurements using complementary techniques including x-ray diffraction (XRD) and transmission electron microscopy (TEM) have also been performed. Electrical characteristics of some of the metal/GaAs contacts as a function of annealing temperature have been investigated with the current voltage (I-V) dependence of diodes. A general description of the theory and the applications of the RBS and HIRBS techniques together with their strengths and weaknesses in the analysis the thin film interactions will be presented in the following sections.

2.1 Conventional and Heavy Ion Rutherford Backscattering Spectrometry

Rutherford backscattering spectrometry (RBS) was established following the discoveries of Rutherford[1] and Geiger and Marsden[2]. The original experiment by Geiger and Marsden was to confirm the atomic model proposed by Rutherford. The basic idea of the experiment is to shoot energetic particles (4 to 8 MeV alpha particles from a radioactive source) at a group of atoms and to examine the angular distribution of the scattered alpha particles. This experiment was originally of interest to nuclear physics and the analytical nature of the backscattering method was not fully realized until the late 1950s [Reference 3].

RBS did not become a powerful analytical technique in solving real scientific problems until the early 60s when solid-state detectors with good energy resolution became available. Perhaps, one of the most famous RBS experiments performed was the Surveyor alpha-scattering experiment in 1967 [References 4 and 5]. In this experiment, the chemical composition of the lunar surface material was determined by RBS. With the rapid growth of the electronic industry and the introduction of planar technology to semiconductor device fabrication, RBS as a near surface (~.01 to 1 micron) characterization technique found more and more applications in electronic materials research in particular in the area of thin film/semiconductor interfaces.[6] In fact, significant contributions to the understandings of silicon contact structures and the advancement of Si technology in general have been achieved using RBS in recent years.

With the development of GaAs ICs and new GaAs devices, there is a rising demand for more stable, reproducible and planar metal contacts to GaAs. However, investigation of metal/GaAs contact problems using the conventional RBS technique are, in many cases, inadequate. This is due to the fact that the mass resolution of the technique on heavy targets (A>50 AMU) is relatively poor (>4 AMU). In other words, energies of the alpha particles backscattered from, say Ga (A=70 AMU) and As (A=75) become indistinguishable. This limitation of RBS can be solved through the use of heavier projectile ions.

2.1.1 RBS: general background

The basic physics of RBS is appealing because of its uncomplicated nature. As a matter of fact, there are only three important physical concepts involved in this technique and each of these can provide a specific kind of information:

(1) the kinematic scattering factor K which gives target mass elemental information,

(2) the scattering cross section σ which gives quantitative information of the atomic composition of the target, and

(3) the energy loss dE/dx of a projectile ion when penetrating through the target which can be interpreted to give depth information of the target layers without sectioning.

All these parameters will be described in the following paragraphs.

A. The kinematic factor K

When a beam of monoenergetic charged particles is incident on a solid surface, it can undergo a number of interactions with the atoms in the target. Some of the particles will interact with the first layer of atoms of the target. If the incoming particle energy E_o is lower than the energy needed to overcome the repulsive coulomb barrier for nuclear reaction between the projectile ion and the target atom, the projectiles will be elastically scattered. The energy of these scattered particles at a specific scattering angle is a function only of the particle mass M_1, the target mass M_2 and the angle of scattering θ. Figure 2.1 shows the geometry of such a collision. Projectiles

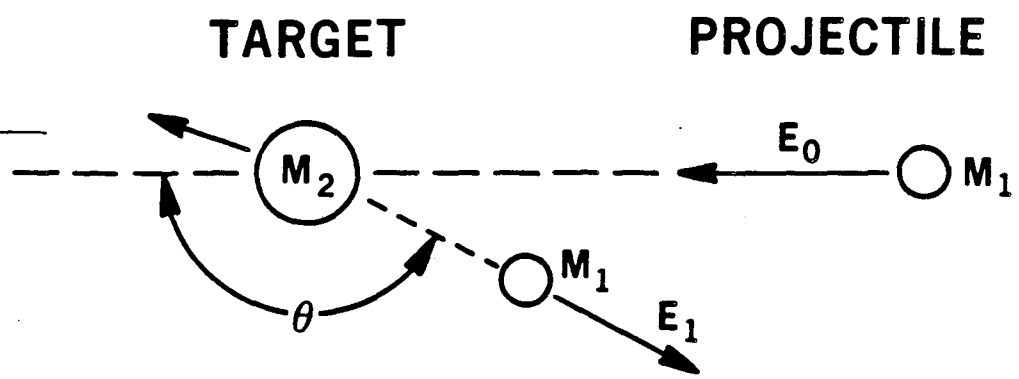

$$K \equiv E_1/E_0$$

$$K(\theta \doteq 180°) = \left[\frac{1 - M_1/M_2}{1 + M_1/M_2}\right]^2$$

$$\frac{d\sigma}{d\Omega} \approx \left[\frac{Z_1 Z_2 e^2}{4E_0}\right]^2 \mathrm{SIN}^{-4}\,\theta/2 \qquad M_1 \ll M_2$$

XBL 834-9456

Figure 2.1 Geometry of an elastic collision process between a projectile atom with mass M_1 and a target atom with mass M_2.

scattered from the surface of the target have an energy $E_1 = KE_o$ where K is the kinematic factor which is determined solely by kinematic consideration. K can be derived from conservation of energy and momentum for a projectile of mass M_1 and scattering from target M_2 at a laboratory angle θ and expressed as follows[6]:

$$K = \left[\frac{(M_2{}^2 - M_1{}^2 \sin^2\theta)^{1/2} + M_1 \cos\theta}{(M_1 + M_2)}\right]^2 . \qquad (2.1)$$

For a given type of projectile ion and at a particular scattering angle, K is uniquely defined for any given target mass. As a result, different element in the target can be identified by measuring the energies of the scattered projectiles.

Figure 2.2 shows the relationship between K and M_2/M_1 for five scattering angles. For $\theta < 90°$, i.e. the forward scattering case, K is relatively insensitive to the change in target mass. Since the K determines the scattered energy of a projectile, it is desirable to have the slope of the K versus M_2/M_1 curve as large as possible in order to achieve good mass resolution. Hence it is most favorable to have a backscattering geometry with θ close to 180° for maximum mass resolving power. It is also obvious from Figure 2.2 and equation 2.1 that when $M_2/M_1 < 1$, K is zero for $\theta > 90°$. In other words, a projectile colliding with a stationary atom with mass smaller than its own mass cannot be scattered backward, but only forward.

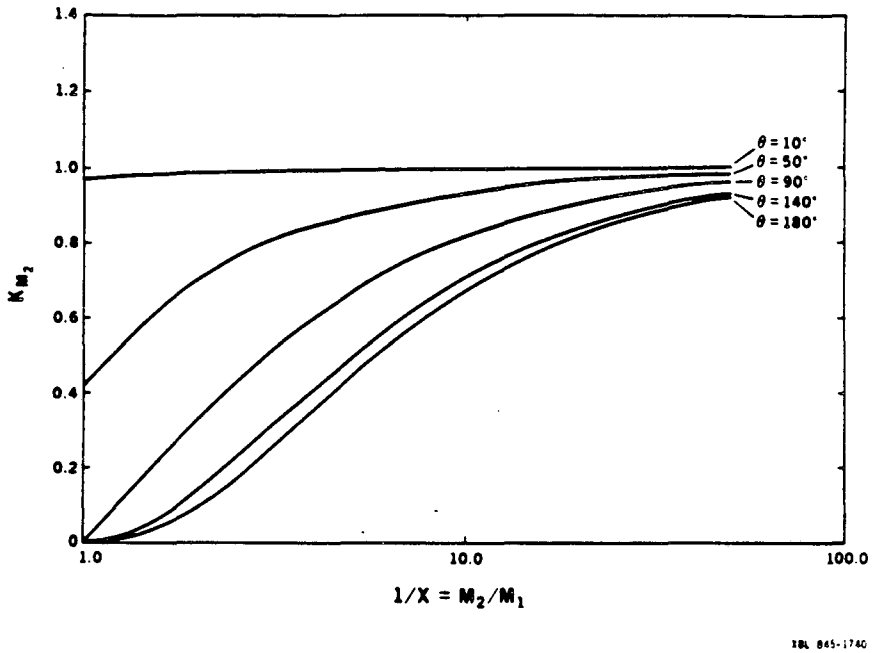

Figure 2.2 The kinematic factor K plotted as a function of the mass ratio $1/x = M_2/M_1$ for different scattering angle θ.

B. Differential Rutherford scattering cross section $d\sigma/d\Omega$

Quantitative information about the target material can be obtained through the differential Rutherford scattering cross section $d\sigma/d\Omega$ where Ω is the detector solid angle which is typically a few millisteradian. The $d\sigma/d\Omega$ can be interpreted as the probability that a particle will be elastically scattered by a target atom through a solid angle between Ω and $\Omega + d\Omega$. The expression for the differential Rutherford scattering cross section has been developed by assumming Coulombic interaction between target and projectile[1,7,8]:

$$\frac{d\sigma}{d\Omega} = \left(\frac{Z_1 Z_2 e^2}{4E}\right)^2 \frac{4}{\sin^4\theta} \frac{\{[1-((M_1/M_2)\sin\theta)^2]^{1/2}+\cos\theta\}^2}{\{1-[(M_1/M_2)\sin\theta]^2\}^{1/2}} \quad (2.3)$$

where Z_1 and Z_2 are the atomic numbers of the projectile and the target nuclei, respectively and E is the incident energy. This expression shows that the number of backscattered particles has a $(Z_1 Z_2/E)^2$ dependence. Because of this Z^2 dependence, targets with heavy impurities in a light matrix are more easily analyzed by RBS than the reverse case.

Generally the total detected backscattered particles A can be related to the amount of material in the target by the following expression:

$$A = d\sigma/d\Omega \cdot QNtd\Omega \quad (2.2)$$

where Q is the total number of incident particles and Nt is the amount of target material in atoms per unit area. Since A, Q and $d\Omega$ are measurable quantities, the amount of target material can be calculated if $d\sigma/d\Omega$ is known. In the case of thin film analysis, assuming that N is the bulk atomic density of the material, the thickness of the film t can also be measured.

C. Energy loss dE/dx

As an energetic ion passes through the target, it slows down gradually due to energy loss to its surrounding by two processes:

(1) Nuclear or elastic scattering--interaction of the ion with the target nuclei. This is the process responsible for Rutherford scattering.

(2) Electronic or inelastic scattering--interaction of the ion with the target electrons.

These two processes are largely independent of each other so that the the total energy loss can be written as:

$$\frac{dE}{dx} = \left.\frac{dE}{dx}\right|_{electronic} + \left.\frac{dE}{dx}\right|_{nuclear} \quad . \tag{2.4}$$

For high energy projectiles (in the MeV range), the nuclear stopping process which has a cross section proportional to $1/E^2$ ($d\sigma/d\Omega \sim 10^{-24} cm^2$) is highly unlikely (equation 2.3) and can be treated as a secondary process for slowing down the ion. The main contribution to the total energy loss of an energetic ion (in the MeV range) in matter stems from its interaction with the target electrons. This interaction results in the excitation or ionization of the target atoms to which the ion comes sufficiently close. These changes of state are caused by the Coulomb force giving a sharp impulse to a target electron as the ion moves by swiftly. The energy transferred to an electron represents a loss of kinetic energy of the moving ion (typically in the order of a few eV). Since the ion has kinetic energy in the MeV range, it hardly changes its direction after an electronic scattering process (hence, this is also referred to as small angle scattering).

Different theoretical models have been derived for the calculation of the energy loss of various ions in matters[9-11]. Compilation of dE/dx values for different ion species in various solids based on theoretical calculations as well as experimental data are available. Because of the growing importance of RBS as a tool for non-destructive depth profiling, a lot of work has been done on the energy loss characteristics of the He and H ions in matter.[12,13] Owing to the large amount of experimental data available, dE/dx values for H and He ions can be obtained with accuracy better than 5%. In contrast, relatively few dE/dx data are available for heavier ions[14,15] so that it is difficult to estimate energy loss values for heavy ions such as N and O to an accuracy better than 15%. With the knowledge of dE/dx, a depth scale can be established for the target.

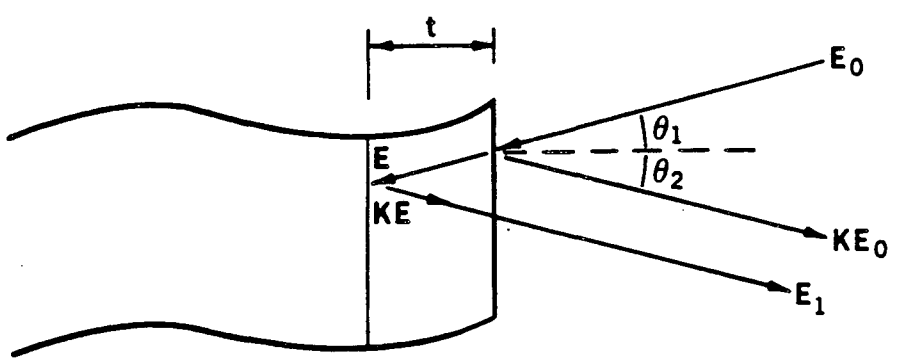

XBL 842-626

Figure 2.3 Schematic diagram of a RBS experiment showing the incident and scattering angle θ_1 and θ_2, the backscattering energy from the surface KE_0 and from a depth t, E_1.

Figure 2.3 illustrates the target-beam interaction in a RBS experiment. The energy difference ΔE between the particles scattered from the target surface and those scattered at a depth t below surface can be written as:

$$\Delta E = KE_o - E_1 = N\,[S]t \tag{2.5}$$

where [S] is called the energy loss factor. With reference to Figure 2.3, the energy loss factor can be expressed as follows:

$$[S] = \frac{K}{\cos\theta_1}\left.\frac{dE}{dx}\right|_{in} + \frac{1}{\cos\theta_2}\left.\frac{dE}{dx}\right|_{out} \tag{2.6}$$

where the subscripts "in" and "out" represent the stopping powers along the inward and outward paths of the ion, respectively. In the surface energy approximation, i.e. using E_o as the energy of the ion, equation 2.6 becomes:

$$[S] = \frac{K}{\cos\theta_1}\left.\frac{dE}{dx}\right|_{E_o} + \frac{1}{\cos\theta_2}\left.\frac{dE}{dx}\right|_{KE_o} \tag{2.7}$$

Since the total energy loss for a projectile ion penetrating a target material with depth δx is dependent on the areal density of the target, a density independent parameter ϵ, the stopping cross section is normally used in RBS analysis. ϵ is defined in the following way:

$$\epsilon \equiv \left(\frac{1}{N} \cdot \frac{dE}{dx}\right) \tag{2.8}$$

with the conventional unit eV-cm^2/atom. In term of this parameter, the energy loss can be written as:

$$\Delta E = [\epsilon]\, Nt \tag{2.9}$$

where $[\epsilon]$ is the stopping cross section factor.

For the case of compounds, the energy loss processes are essentially the same as for pure elements. In 1905 Bragg and Kleeman postulated the principle of the additivity of stopping cross sections [Reference 16], later known as the Bragg's rule and it was stated as follows:

$$\epsilon^{A_m B_n} = m\epsilon^A + n\epsilon^B \tag{2.10}$$

where $\epsilon^{A_m B_n}$ is the stopping cross section of the molecule AmBn, m and n are the atomic fraction of atoms A and B, and ϵ^A and ϵ^B are the stopping cross section of the atomic constituents A and B.

2.1.2 RBS spectrum for thin film samples

A schematic of the backscattering geometry and the resulting energy spectrum for a thin film with element mass M'_2 on a substrate with element mass M_2 is shown in Figure 2.4. The abscissa is usually

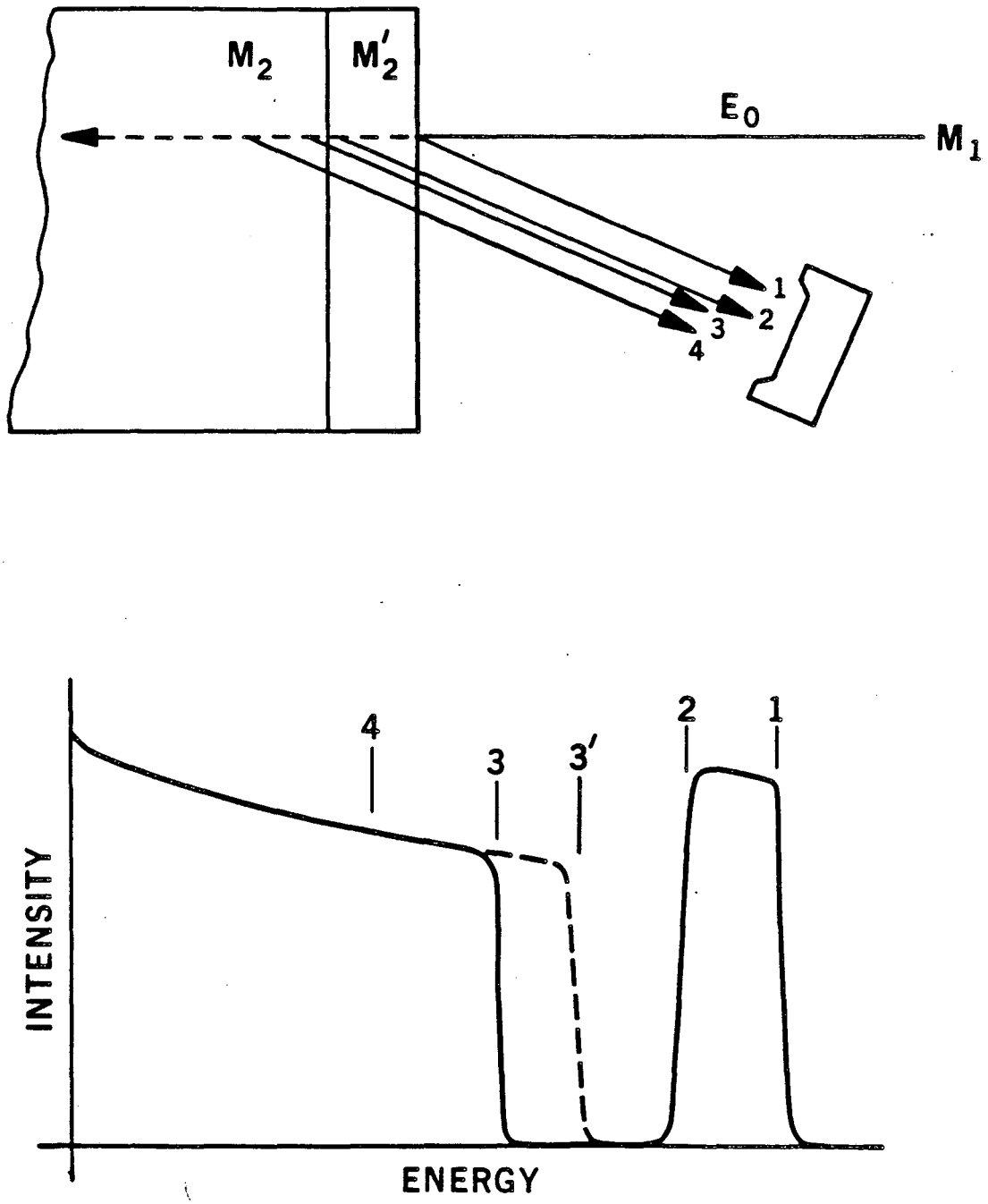

XBL 834-9455

Figure 2.4 (a) Schematic of the backscattering process of a thin film of mass M'_2 on a substrate with mass M_2 where $M'_2 > M_2$. (b) The corresponding RBS spectrum of (a). The dashed line represents the edge of the substrate without the overlayer.

represented in channel number which can be converted into an energy scale by using the energy loss information discussed in the last section. The ordinate is the backscattering yield of the projectiles per channel. We have chosen $M'_2 > M_2$. Under this condition the thickness of the thin film can be easily determined from the energy difference at edges 1 and 2. Using equations (2.5) and (2.6) the film thickness t can be expressed as:

$$t = (E_1 - E_2)\left(K_{M'_2} \frac{dE}{dx}\bigg|_{in}^{M'_2} + \frac{1}{\cos\theta_2} \frac{dE}{dx}\bigg|_{out}^{M'_2}\right)^{-1} \qquad (2.11)$$

where $K_{M'_2}$ is the scattering factor for M'_2 and $\frac{dE}{dx}\Big|_{in}^{M'_2}$ and $\frac{dE}{dx}\Big|_{out}^{M'_2}$ are the energy loss along the in and out paths for M_1 in M'_2, respectively. This thickness can also be determined by measuring the energy shift of the substrate surface signal with and without the film on top. The dotted spectrum in Figure 2.4(b) represents the spectrum of M_2 without the film.

Depth resolution of RBS is governed by the uncertainty ΔE_R in energy measurement which has two major sources: detector energy resolution ΔE_d and energy straggling ΔE_s. For conventional RBS using Si surface barrier detectors, the detector energy resolution (full width at half maximum) ΔE_d is typically 15 keV (detector energy resolution of better than 8keV can be achieved by cooling the detector). Energy straggling ΔE_s of the projectile in the target arises from the statistical fluctuations in the numerous energy loss processes of the

projectile in the target. It depends on the kind of projectile, the target atomic number, and the density and thickness of the target. An estimate of the straggling of projectile Z_1 in target Z_2 of thickness t and atomic density N can be obtained from the Bohr value of straggling variance[17]:

$$\Omega_B^2 = 4\pi(Z_1 e^2)^2 N Z_2 t \qquad (2.12)$$

For thick film targets (> 1000 Å) with mass >50 AMU ΔE_s is comparable to ΔE_d. The total energy resolution of the system is then the quadratic sum of ΔE_s and ΔE_d which is typically of the order of 20 keV resulting in depth resolution of about 200 Å. Although the energy resolution is to a large extent fixed by the type of detector used, improvement in depth resolution can still be achieved by varying the scattering geometry to increase the effective depth of penetration of the beam.

Figure 2.5 shows a schematic of the RBS spectrum for the case when there is interaction at the thin film/substrate interface (such as in silicide formation). The overlayer A has partially reacted with the substrate B in Figure 2.5. The thicknesses of the reacted layer, the unreacted film, and the amount of film and substrate materials reacted can be measured from the energy loss characteristics. The composition of the layer formed at the interface, A_mB_n can also be obtained from the height ratio of the signals in the spectrum :

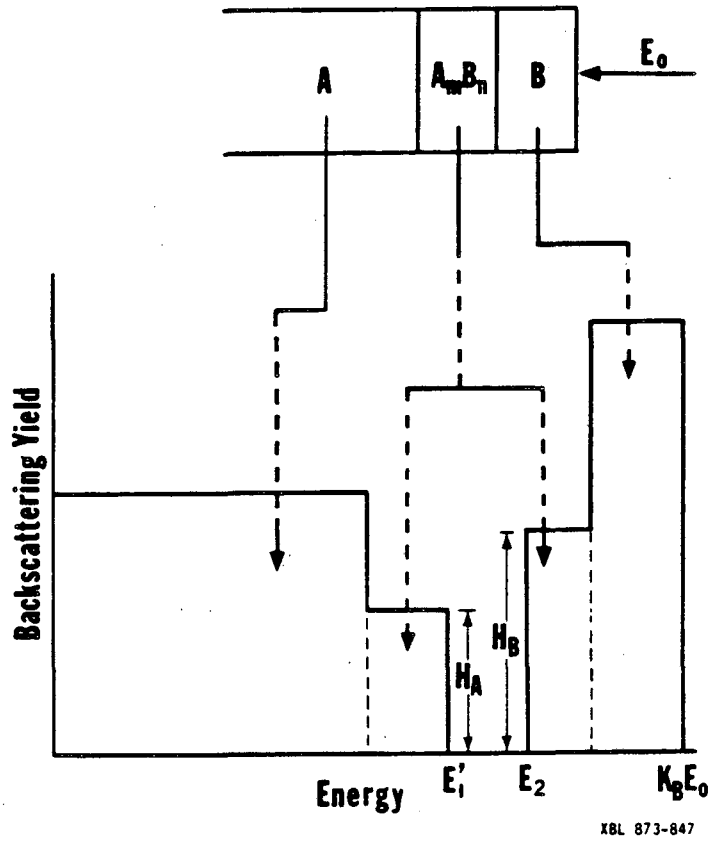

Figure 2.5 Schematic of the ideal RBS spectrum of a thin film/ substrate sample where there is interaction at the interface with mass of the film higher than that of the substrate.

$$\frac{n}{m} = \frac{H_B}{H_A} \frac{(d\sigma/d\Omega)_A}{(d\sigma/d\Omega)_B} \frac{[\epsilon]^B_{A-B}}{[\epsilon]^A_{A-B}} \tag{2.13}$$

In equation (2.13) the superscripts of the stopping cross section factor refer to the scattering atoms and the subscripts, to the alloy the beam traverse. The last term in the above equation is very close to one and is usually neglected for first order approximation.

2.1.3 Limitations of conventional RBS for thin film analysis

The RBS spectrum in Figure 2.5 shows that for $E_2 > E'_1$, the interpretation of the RBS spectrum is straight forward. However, there are cases when the mass of the overlayer is close to that of the substrate. In these cases, the backscattering signals from the layer and the substrate begin to overlap, i.e. $E'_1 \simeq E_2$. When this occurs, interpretation of the RBS spectra becomes difficult. The energy separation of E'_1 and E_2 is mainly governed by the kinematic factor K for the corresponding materials. Figure 2.6 shows a plot of the kinematic factor K as a function of the target mass M_2 for ^{4}He backscattered at $\theta = 170°$. Note that the slope of the curve approaches zero as M_2 increases above 50 AMU.

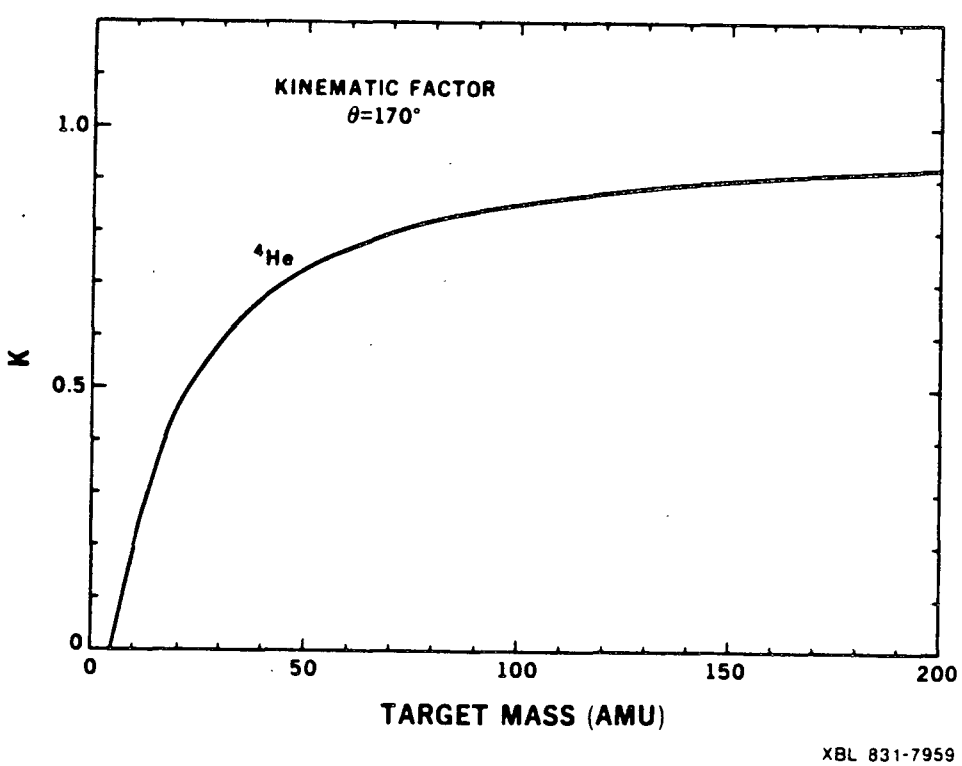

Figure 2.6 Kinematic factor versus target mass for ^{4}He projectiles calculated for 170° scattering angle.

In the past twenty years, RBS has been used for the analysis of metal silicide formation. Since Si has mass of 28 AMU, K_{Si} is in the most sensitive region of K versus M_2 curve. Moreover, all transition metals of interest in silicide formation studies are considerably heavier than Si. Hence interpretation of the RBS spectra from silicides are usually straight forward. For the case of thin film metal/GaAs, however, significant signal overlapping always occurs in the RBS spectrum. This is mainly due to the insensitivity of the K with respect to changes in target masses for high Z elements (M_2 for GaAs is 70 AMU).

Figure 2.7 illustrates the criterion for signal separation between overlayer (with mass M'_2) and substrate (with mass M_2) signals for (a) $M'_2 > M_2$ and (b) $M'_2 < M_2$. In this figure the spectra for the unreacted cases are represented by dotted lines while those for the reacted cases by solid lines. From Figure 2.7, it is obvious that no signal overlap occurs when $\Delta E > \Delta E_R$ where ΔE_R is the total system energy resolution and ΔE is for case (a) the energy difference between the high energy edge of the substrate signal and the low energy edge of the overlayer signal and for case (b), that between the high energy edge of the overlayer signal and the unreacted substrate front edge. ΔE can then be written as :

$$\Delta E = |K_{M'_2} - K_{M_2}| \, E_o - [S]t \qquad (2.14)$$

where t is the film thickness and [S] is the energy loss factor of the overlayer. Assuming an overlayer with [S]t $\approx$ 200 keV (~1500 Å of Pd)

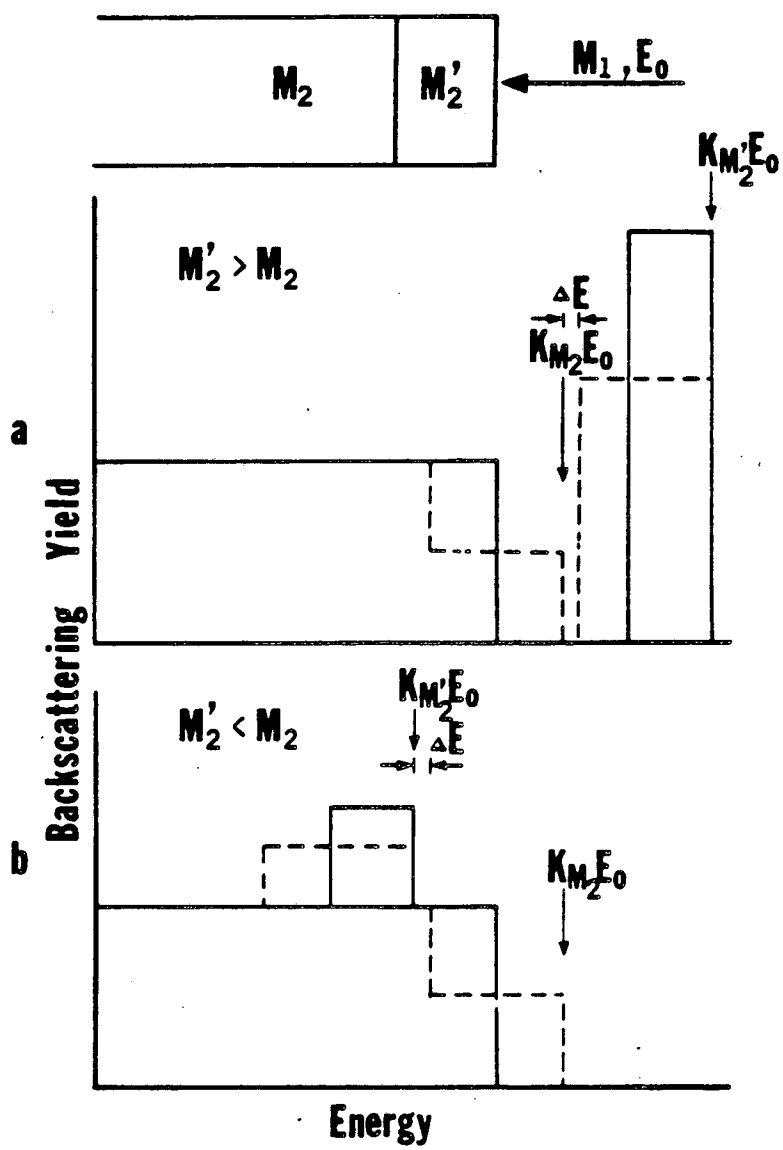

XBL 872-562

Figure 2.7 Schematics of the ideal RBS spectra of samples of thin film with mass M'_2 on substrate with mass M_2 illustrating the criterion for signal separation between overlayer and substrate backscattering signals for (a) $M'_2 > M_2$ and (b) $M'_2 < M_2$.

and a ΔE of $\approx$15 keV for 2.0 MeV α-RBS, $|K_{M'_2}-K_{M_2}|$ must be larger than 0.11 in order to avoid signal overlap. Taking Ge (which has mass similar to that of GaAs) as the substrate, then M'_2 has to be smaller than 42 or larger than 162 so that the overlayer and the substrate signal can be resolved. This poses a serious problem in the investigation of metal/GaAs contact systems using RBS. Recently, the interpretation of complicated RBS spectrum using computer simulation skill has achieved some success in the application of RBS to metal/GaAs systems overcoming the signal overlapping problem [References 18-20]. However, since fitting a RBS spectrum is a multi-parameter problem, the results of these simulations can be misleading. A better solution to this limitation is the use of heavy ions as projectiles for backscattering analysis. The advantages of heavy ion RBS will be discussed in the following section.

2.1.4 Advantages of heavy-ion RBS (HIRBS)

Figure 2.8 shows the kinematics factor K as a function of target mass M_2 for various projectiles scattered at θ=170°. It is obvious that for large M_2 (>50 AMU), the slope of the curve increases as the mass of the projectile M_1 increases. The increase in sensitivity of K for heavy target masses using heavy projectiles results in the improvement in mass resolving power. For thin film analysis, in order to achieve good resolution, the maximum value of ΔE in equation (2.14) is desirable. In other words, both sensitivity of K and the incident projectile energy should be maxima while the energy loss and energy uncertainty should be minima.

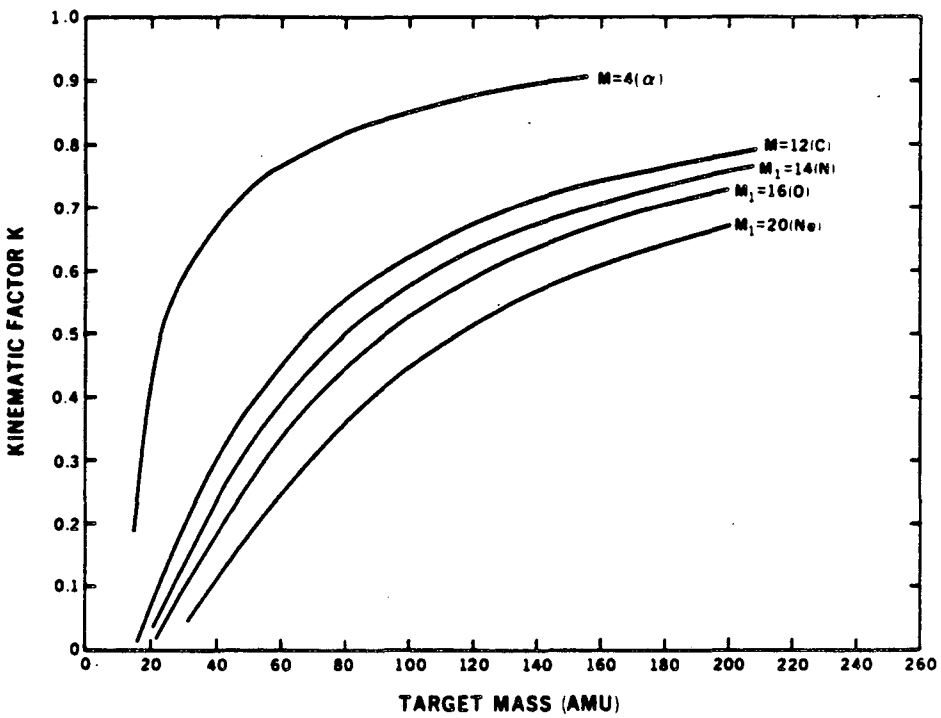

Figure 2.8 The kinematic factor K plotted as a function of target mass M_2 for different projectile ions with mass ranging from 4 to 20 AMU.

The upper limit for the projectile energy E_o is governed by the Coulomb barrier E_c caused by electrostatic repulsion between the nuclear charges of the projectile particle and the target nuclei. If E_o is larger than E_c inelastic nuclear reaction occurs and the process can no longer be analyzed by simple scattering physics. The height of the Coulomb barrier can be related to the atomic numbers, Z_1 and Z_2 and mass numbers, A_1 and A_2 of the projectile and the target in the following way[21]:

$$E_c = \frac{Z_1 Z_2 e^2}{r_o (A_1^{1/3} + A_2^{1/3})} \tag{2.15}$$

where r_o is a radius parameter ranging from 1.2 to 1.5 $X10^{-13}$cm. When heavy ions are used as projectiles, the Coulomb barrier increases. Therefore, a higher energy can be employed with heavy projectiles without breaking the Coulomb barrier, i.e. without the interference of nuclear reactions.

It is also desirable to minimize the energy loss factor [S] through a thin film as is evident in equation (2.14). However, minimizing the energy loss also degrades depth resolution since depth resolution $\delta x \sim 1/[S]$. Moreover, for Si detectors, the detector resolution degrades with the increase in projectile mass[22]. With 20 MeV ^{16}O projectile FWHM resolution for Si surface barrier detector of ~100 keV has been reported[23]. For optimum resolution in thin film analysis, careful consideration has to be given to different parameters in the backscattering process. With 20 MeV ^{16}O HIRBS on a sample with a thin overlayer on Ge substrate at θ=170°, typical values of [S]t (for 1500 Å Pd layer) are ~1.1 MeV with a system energy resolution ΔE_R ~120 keV. From equation (2.14), it can be estimated that thin film metal/GaAs systems with a metal mass smaller than 60 AMU and larger than 80 AMU can be effectively analyzed by HIRBS. In other words, almost all transition metal/GaAs couples can be studied by HIRBS. Table III gives a comparison of the typical values for different parameters in RBS and HIRBS analysis of thin film samples.

Table III Comparison of the typical values for different parameters in RBS and HIRBS analysis of thin film samples.

	RBS[a)]	HIRBS[b)]
$[S_o]t$[c)] (MeV)	0.2	1.10
ΔE_R (MeV)	0.018	0.13
Resolvable Overlayer Mass M_2' (AMU)	$M_2' < 42$ $M_2' > 162$	$M_2' < 60$ $M_2' > 80$

a) 2.0 MeV ^{4}He beam.
b) 20 MeV ^{16}O beam.
c) Assuming a Pd overlayer 1500 Å thick.

Depth resolution for HIRBS is not as good for low mass materials (<100 AMU) but is comparable to that of RBS for high mass target. A comparison of depth resolution for RBS and HIRBS with typical values for the corresponding scattering parameters is given in Table IV. The reduced depth resolution of HIRBS for low mass targets is due to the low [S] values of heavy projectiles in these targets. Since depth resolution can always be improved by varying the scattering geometry as mentioned in the last section, this is not a serious disadvantage to the technique.

Energy straggling of HIRBS has been studied with 20 MeV ^{16}O projectiles passing through Al, Cr and Au films of various thicknesses. Figure 2.9 shows the variance of the straggling through the different metal films as a function of the square root of the areal density of the film ($\sqrt{Nt}$). The corresponding Bohr straggling values for the different metals are also shown (dashed lines) for comparison.

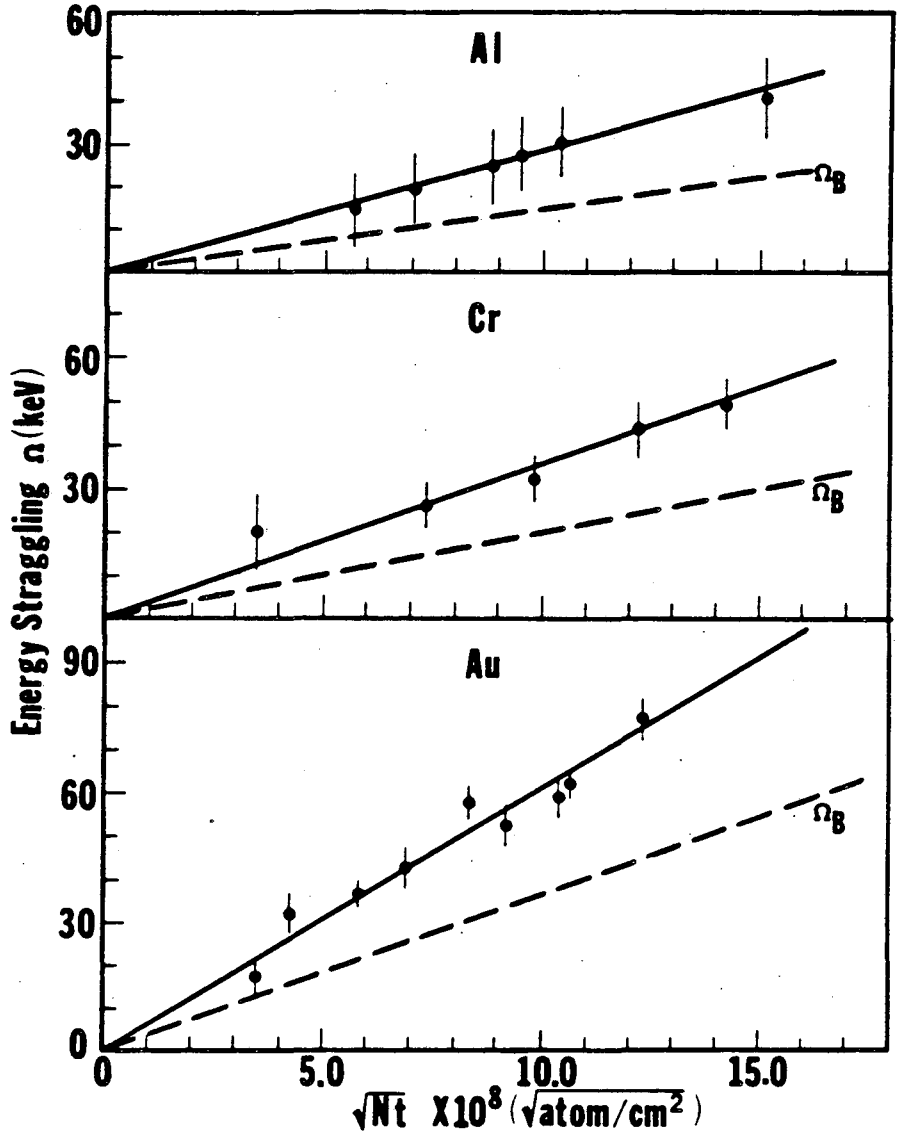

Figure 2.9 Plots of the experimental energy stragglings as functions of the square root of the film thickness in atoms/cm^2 for 20 MeV ^{16}O ions in Al, Cr and Au targets. The dashed lines in the plots show the corresponding Bohr straggling values.

Table IV Comparison of depth resolution in Å for RBS and HIRBS under similar scattering geometry.

Target Material	RBS[a)]	HIRBS[b)]
Al	330	680
Ni	130	170
Pd	110	150
Ag	140	160
Au	110	120

a) 2.0 MeV ^{4}He beam.
b) 20 MeV ^{16}O beam.

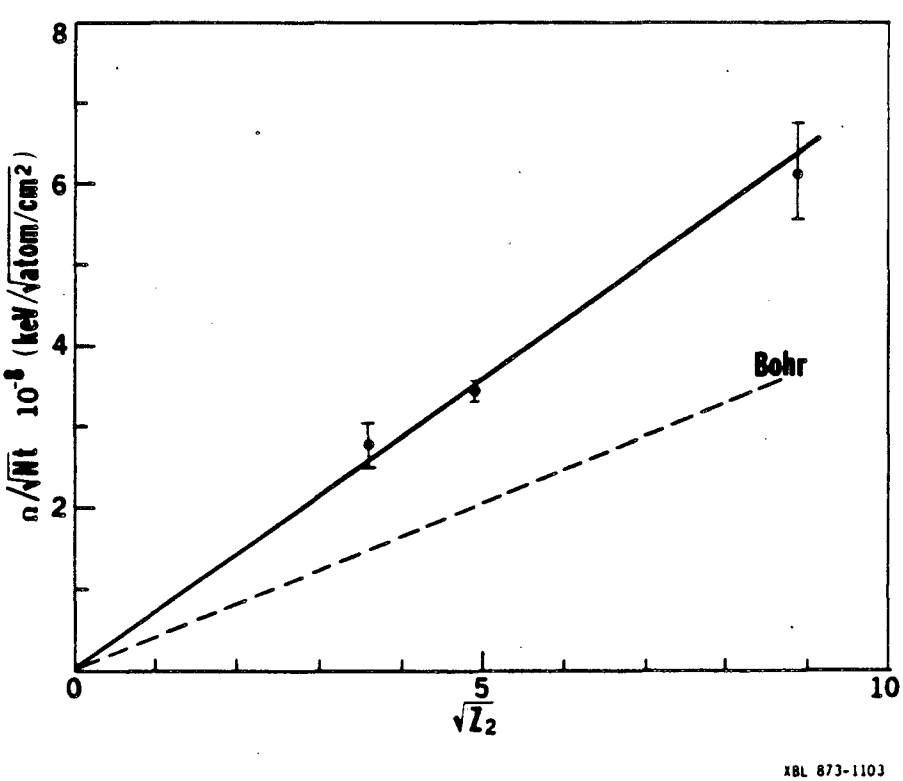

Figure 2.10 A plot of the $\Omega/\sqrt{Nt}$ versus $\sqrt{Z_2}$ where Ω is the experimental straggling values taken from Figure 2.9. The dashed line is a similar plot using the Bohr stragglling values.

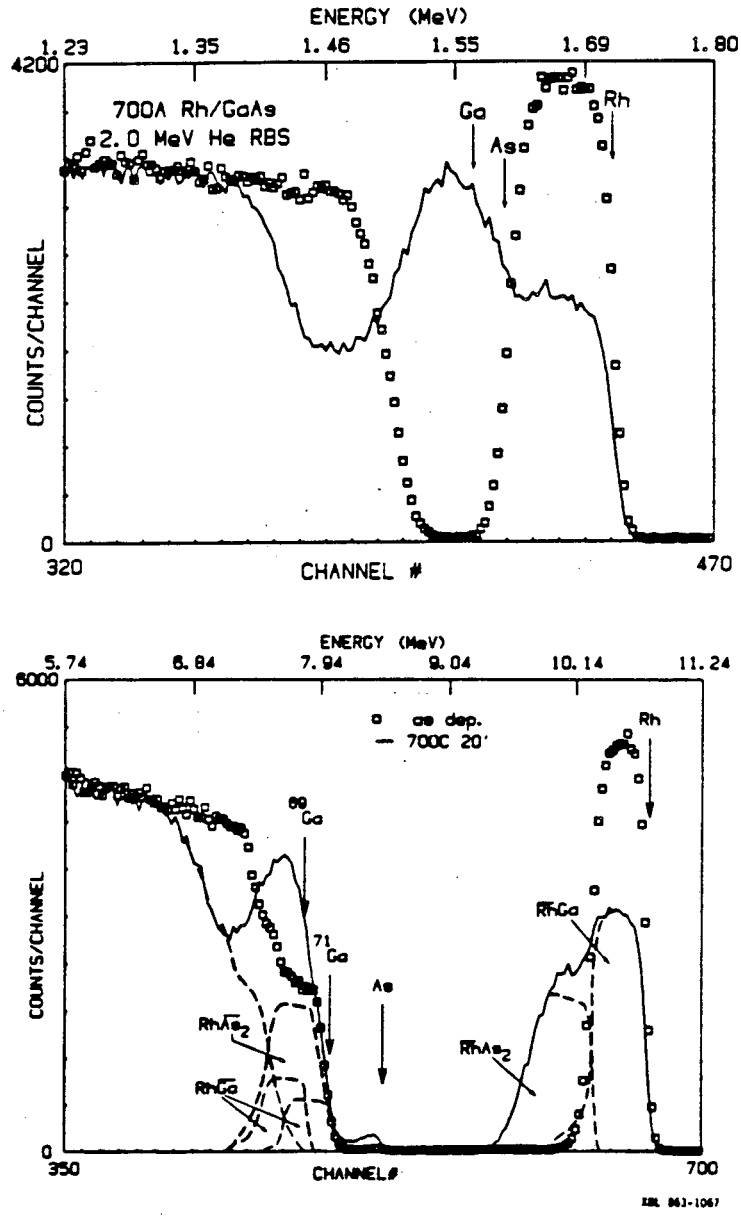

Figure 2.11 A comparison of the 2.0 MeV α-RBS and 20 MeV ^{16}O HIRBS spectra of 700 Å Rh/GaAs sample after reactions. The improved mass resolution of HIRBS is clearly illustrated in the spectrum.

It can be seen that the values for experimental straggling Ω for heavy ions are larger than the Bohr values but still follow the same dependence. Figure 2.10 shows a plot of $\Omega/\sqrt{Nt}$ versus $\sqrt{Z_2}$. A linear dependence is observed indicating a relationship: $\Omega^2 \sim NtZ_2$. From the slope of the plot in Figure 2.10, the following empirical relationship is derived for the straggling of 20 MeV ^{16}O ions in matter:

$$\Omega^2 = 5.0X10^{-17}NtZ_2$$

where Nt is expressed in atoms/cm^2 and Ω in keV. With ^{16}O ions, the Bohr values for straggling is given by:

$$\Omega^2 = 1.67x10^{-17}NtZ_2.$$

Applications of HIRBS using projectiles such as lithium[24], nitrogen[25,26] and oxygen[27-29] to different problems relating to materials science have proven the value of HIRBS as an analytical tool for near surface characterization. Recently, HIRBS has also been extensively applied to the study of GaAs and Ge contact reactions[23,31] with considerable success. Figure 2.11 shows a comparison of the 2.0 MeV α-RBS and 20 MeV ^{16}O HIRBS spectra from 700 Å Rh/GaAs sample after reactions. The improved mass resolution of HIRBS is clearly illustrated in the spectrum. The layer structure of the reacted Rh/GaAs interface is clearly visible in the HIRBS spectrum. However, overlapping of the signals from Rh and GaAs in the α-RBS spectrum is so serious that no sensible interpretation can be derived from this spectrum.

2.1.5 Instrumentation

Both conventional RBS and HIRBS measurements have been carried out on thin film metal/GaAs systems. A 20 MeV $^{16}O^{++}$ beam generated by the 88" cyclotron at the Lawrence Berkeley Laboratory was used for HIRBS measurements. The 20 MeV ^{16}O beam was chosen to achieve good mass resolution, high backscattering yield and high dE/dx. For HIRBS, the incident beam was collimated to a 1.5 mm diameter spot size with an angular spread of less than 1°. An annular silicon surface barrier detector (EG & G Ortec model #TC-021-300-100) depleted to a depth of 200 μm was situated in the beam line in front of the sample so that the beam passes through the open center of the detector. The scattering angle was 176.25° with a solid angle for detection ≈ 16.45 msr. The detector was coated with 40.0 μg/cm² of Au and 40.2 μg/cm² of Al as front and back electrodes, respectively. Positive bias of 130 V was applied to the detector during operation and an energy resolution of 25 keV (FWHM) was achieved for 5 MeV alpha particles. Overall system resolution for 20 MeV ^{16}O was ≈110 keV (FWHM). Typical beam currents ranged from 30-100 nA and a total charge between 20-50 μC was normally accumulated for each sample. The target was tilted at ~3° with respect to the beam in order to minimize channeling effects in the single crystal substrates.

Conventional RBS measurements were performed with 2.0 MeV $^{4}He^{+}$ ions generated by the 2 MeV Van de Graaff at LBL. The beam was focussed down to 0.75 mm in diameter on target. A Si surface barrier detector was situated at a backscattering angle of 170° with a detector

solid angle of ~2.7 msr. A system energy resolution of ≈18 keV was achieved. Beam currents were usually below 15 nA and the accumulated total charge ranged from 5 to 12 μC for each sample. Secondary electrons produced from the target were suppressed by a cylindrical ring positioned around the target biased to -900 V. For very thin layers with thickness < 150 Å, samples were mounted on a goniometer and tilted to an incident angle > 50° in order to improve depth resolution.

The detector output pulses were amplified and fed into a 1024 channel pulse height analyzer. The pulse height spectra were then stored on floppy diskettes for plotting and subsequent analysis.

2.2 Complementary Techniques

For the investigation of thin film metal/GaAs interface interactions, HIRBS and RBS can provide information on chemical composition as a function of depth. However, other important information such as structure of the reacted phases and their orientation relationship with the substrate and morphology of the film and that of the metal/GaAs interface is missing. In order to understand the contact issues on GaAs in a systematic and complete fashion, measurements with other analytical techniques have to be performed on the same systems in addition to the backscattering measurements. Complementary techniques used in this work include x-ray diffraction, transmission electron microscopy, scanning electron microscopy and current-voltage dependence.

X-ray diffraction (XRD) experiments were performed in the Bragg-Brentano focusing geometry where the diffraction peaks were recorded by a detector scanning through a Bragg angle 2θ, ranging from 10 to 100°. Phase identification was achieved by matching the detected diffraction peaks with x-ray powder diffraction data files. XRD in this geometry is sensitive to films with thicknesses $\gtrsim$300 Å.

Sample morphology was characterized by transmission electron microscopy (TEM) of plan-view and cross-sectional samples. Electron diffraction was performed in a Siemens 102 TEM at 100 keV. The combination of electron and x-ray diffraction data facilitates conclusive phase identification. In the case of thin film (120 Å) Pd/GaAs, the composition of the reacted film was determined by energy dispersive x-ray analysis (EDS) in a JEOL JEM 200 CX operated at 100 keV. In the case of W/GaAs, the sample morphology was also studied by scanning electron microscopy (SEM) with a Hitachi S310 SEM.

Electrical properties of some of the contact systems were also investigated by the current-voltage (I-V) dependence of the systems. I-V measurements were performed with a HP 4140B current meter with a built-in dc voltage source. Ideal I-V characteristics are represented by the following equation:

$$J = A^{*}T^{2}\exp\left(\frac{-q\phi_b}{kT}\right)\left[\exp\left(\frac{qV_a}{nkT}\right)-1\right], \qquad (2.16)$$

where J is the current density, A^{*} is the effective Richardson constant

(taken to be ~8.16 $A/cm^2/K^2$ in this work), T is the measurement temperature expressed in degree Kelvin, k is the Boltzmann constant, V_a is the applied voltage, $q\phi_b$ is the Schottky barrier height of the diode, and n is the ideality factor which is ≈1 if the thermionic emission process dominates. In the investigation of the W/GaAs contact system, capacitance-voltage (C-V) measurements were also carried out with a HP 4192A impedance analyzer. Dopant concentration profiles of the GaAs substrates and the Schottky barrier heights of the diodes can be obtained by plotting the $1/C^2$ versus reverse bias voltage V_R. The dopant concentration N_d at the edge of the depletion region x_d under an applied dc voltage V_R is expressed as

$$N_d(x_d) = \frac{-2}{\{q\epsilon\epsilon_o A^2[d(1/C^2)/dV_R]\}}, \qquad (2.17)$$

where A is the diode area and ϵ is the relative permittivity of the substrate material and ϵ_o is the permittivity of free space.

REFERENCES TO CHAPTER 2

1. E. Rutherford, Phil. Mag. **21**, 669 (1911).

2. H. Geiger and E. Marsden, Phil. Mag. **25**, 606 (1913).

3. S. Rubin, T. O. Passell and E. Bailey, Anal. Chem. **29**, 737 (1957).

4. A. L. Turkevich, K. Knolle, R. A. Emmert, W. A. Anderson, J. H. Patterson and E. Franzgrate, Rev. of Sci. Instrum. **37**, 168 (1966).

5. A. L. Turkevich, E. J. Franzgrate and J. H. Patterson, Science **158**, 635 (1967).

6. W. K. Chu, J. W. Mayer and M-A. Nicolet, *Backscattering Spectrometry* (Academic Press, New York, 1978).

7. H. Goldstein, *Classical Mechanics* (Addison-Wiley, Mass.,1959).

8. R. B. Leighton, *Principle of Modern Physics* (McGraw Hill, New York, 1959).

9. H. A. Bethe, Ann. Phys. **5**, 325 (1930).

10. F. Bloch, Ann. Phys. **16**, 285 (1933)

11. J. Lindhart and A. Winthers, Mat. Fys. Medd. Dan. Vid. Selsk. 34, No.4 (1964).

12. H. H. Andersen and J. F. Ziegler, *Hydrogen Stopping Powers and Ranges in All Elements* (Plenum Press, New York, 1977).

13. J. F. Ziegler and W. K. Chu, At. Data and Nucl. Data Tables 13, 463 (1974).

14. J. F. Ziegler, *Handbook of Stopping Cross Sections for Energetic Ions in All Elements* (Pergeamon Press, New York, 1980).

15. L. C. Northcliff and R. F. Schilling, Nucl. Data Table A7, 233 (1970).

16. W. H. Bragg, R. Kleeman, Phil. Mag. **10**, 318 (1905).

17. N. Bohr, Phil. Mag. **30**, 581 (1915).

18. L. R. Doolittle, Nicl. Instrum. Meth. **B9**, 344 (1985); and Nucl. Instrum. Meth. **B15**, 227 (1986).

19. P. A. Saunders and J. F. Ziegler, Nucl. Instrum. Meth. **218**, 67 (1983).

20. J. M. Eridon and G. S. Was, Nucl. Instrum. Meth. **B12**, 505 (1985).

21. See for example, H. Semat, *Introduction to Atomic and Nuclear Physics* (Holt, Rinehart and Winston, New York, 1971).

22. S. Petersson, P. A. Tove, O. Meyer, B. Sundqvist and A. Johansson, Thin Solid Films **19**, 157 (1973).

23. K. M. Yu, J. M. Jaklevic and E. E. Haller, Nucl. Instrum. Meth. **B10/11**, 606 (1985).

24. E. Norbeck, L. W. Li, H. H. Lin and M. E. Anderson, Nucl. Instrum. Meth.

25. W. Pabst in *Ion Beam Surface Layer Analysis* Vol.1, eds. O. Meyer, G. Linker and F. Käppeler, p.211 (Plenum Press, New York, 1976).

26. P. Oerson, A. Chevarier, N. Chevarier, P. Clechet, D. Lamonche, J. R. Martin and M. Stern, Nucl. Instrum. Meth. **B15**, 425 (1986).

27. M. Östling and C. S. Petersson, Nucl. Instrum. Meth. **B4**, 88 (1984).

28. K. Takita, K. Masuda, H. Kudo and S. Seki, Appl. Phys. Lett. 37, 460 (1980).

29. K. Takita, K. Murakami, H. Otake, K. Masuda, S. Seki and H. Kudo, Appl. Phys. Lett. **44**, 996 (1984).

30. K. Takita, T. Ipposhi, K. Murakami, K. Masuda, H. Kudo and S. seki, J. Appl. Phys. **59**, 1500 (1986).

31. K. M. Yu, J. M. Jaklevic and E. E. Haller, Mat. Res. Soc. Symp. Proc. **69**, 281 (1986).

Chapter 3 RESULTS AND DISCUSSIONS I: SOLID PHASE REACTIONS BETWEEN (100) GaAs AND NEAR NOBLE METAL FILMS

As mentioned in section 1.3.2, near noble metals react with GaAs at low temperatures (usually below 350°C). Unlike the noble metals which only react with either Ga or As [Reference 1], near noble metals react with both the anion and cation of the substrate semiconductor to form stable M-III and M-V phase(s). This property is particularly important for GaAs contacts because by reacting with both Ga and As the presence of non-stoichiometry related defects will be minimized in the GaAs layer beneath the reacted layer at the interface.

Investigation of the solid phase reactions between (100) GaAs and near noble metals including cobalt, rhodium, iridium, nickel, palladium and platinum have been carried out. The results are summarized in Table V. In the following sections discussions on these experimental observation will be presented. Details on the sample preparation procedures are given in the appendix.

3.1 Co/GaAs

Cobalt films with thicknesses of 120 and 1100 Å were vacuum deposited on (100) GaAs and annealed under different conditions in order to study different aspects of the solid-state reactions of the Co/GaAs contact system. HIRBS and RBS measurements show that interface

Table V Summary of the solid phase reactions between near noble metal thin films and (100) GaAs substrates.

Metal	Reaction Temp. (°C)	Phases formed	Phase Distribution	Reaction Rate[a)]	Activation Energy (eV)
Co	≤300	Co_2GaAs (Hexagonal)	-	D	1.68±0.10
	500	CoGa (Cubic) CoAs (Orthorhombic)	Laterally Separated		
Rh	300	RhGa (Cubic) RhAs (Orthorhombic)	RhGa/RhAs/GaAs	D	1.65±0.20
	400	RhGa (Cubic) $RhAs_2$ (Monoclinic)	$RhGa/RhAs_2/GaAs$		
Ir	500	IrGa (Cubic) $IrAs_2$ (Monoclinic)	$IrGa/IrAs_2/GaAs$	D	3.15±0.15
	700	Ir_3Ga_5 (Tetragonal) $IrAs_2$ (Monoclinic)	$Ir_3Ga_5/IrAs_2/GaAs$	N	-
Ni	200	Ni_xGaAs (Hexagonal) x varies from 3 to 2 at temp. increases	-	-	-
	·500	NiGa (Cubic) NiAs (Hexagonal)	Laterally Separated	-	-
Pd	250	Pd_xGaAs (Hexagonal) $x \approx 4$	-	-	-
	350	Pd_yGaAs (Hexagonal) $y \approx 3.5$	-	-	-
	450	Pd_2Ga (Orthorhombic) $PdAs_2$ (Cubic)	Laterally Separated	-	-
	≥600	PdGa (Cubic) $PdAs_2$ (Cubic)	Laterally Separated	-	-

Table V (cont.)

Pt	300	Pt_3Ga (Cubic)· $PtAs_2$(Cubic)	$Pt_3Ga/PtAs_2/GaAs$	D	1.60±0.15
	500	PtGa (Cubic) $PtAs_2$(Cubic)	$PtGa/PtAs_2/GaAs$		

a) D≡diffusion controlled reactions and N≡nucleation controlled reactions.

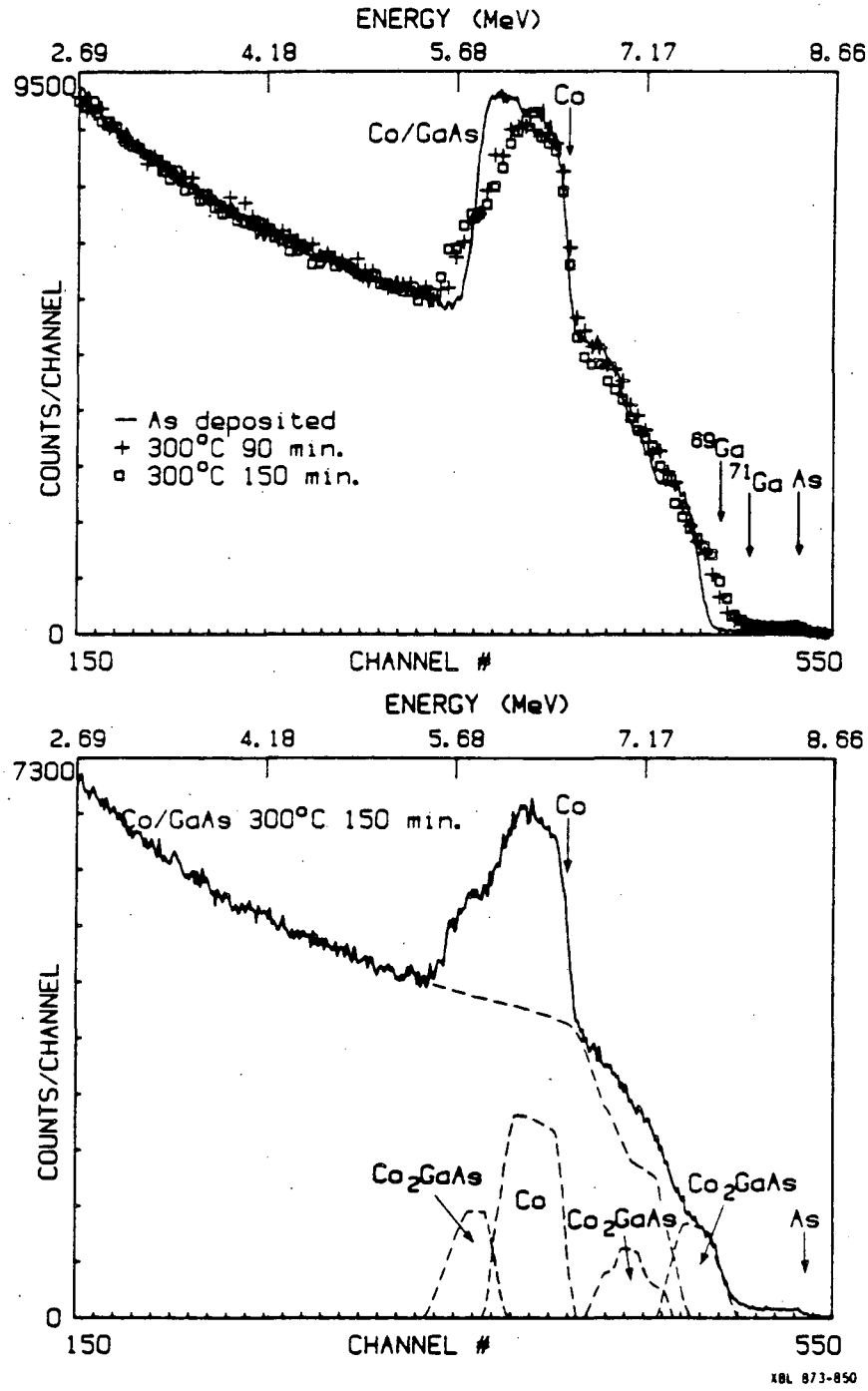

Figure 3.1 (a) A series of HIRBS spectra of 1100 Å Co/GaAs as deposited and annealed at 300 °C for 90 and 150 min. (b) Deconvolution of the HIRBS spectrum of Co/GaAs sample annealed at 300 °C for 150 min showing a layer sequence of Co/Co-Ga-As/GaAs.

reaction of the Co/GaAs system starts at an annealing temperature below 300°C. Figure 3.1(a) shows a series of HIRBS spectra from 1100 Å Co on GaAs samples as deposited and annealed at 300°C for 90 and 150 min. The deconvolution of the spectrum of a sample annealed at 300°C for 150 min is given in Figure 3.1(b) showing a layer sequence Co/Co-Ga-As/GaAs. Bars over individual elements in the spectrum represent the backscattering signals from that element in the compound, for example Co_2GaAs means the backscattering signal from Co in Co_2GaAs. Height ratio and energy loss analyses of the spectra indicate that the intermediate layer formed has a [Co]:[Ga]:[As] ratio of ≈ 2:1:1. The entire 1100 Å Co film is reacted with GaAs after annealing at 400°C for 150 min. Figure 3.2 is a HIRBS spectrum from Co/GaAs annealed at 450°C for 90 min. The deconvolution of this spectrum shows a reacted layer with composition similar to that of the intermediate layer in the sample annealed at 300°C. The XRD spectrum from this sample shows a diffraction pattern distinctly different from that of any binary phase of Co-Ga and Co-As. Therefore we assume that the first phase formed from Co/GaAs solid phase reaction at 300°C is a ternary phase with nominal composition Co_2GaAs. Our assumption is in good agreement with the results of Yu et al[2,3] who first determeined the composition of this ternary phase by computer simulation analysis of the RBS spectra together with XRD measurements and TEM analysis.

HIRBS spectra for Co/GaAs samples annealed at temperatures higher than 500°C do not show significant differences from the spectra of the sample annealed at 450°C for 90 min (Figure 3.2). XRD measurements,

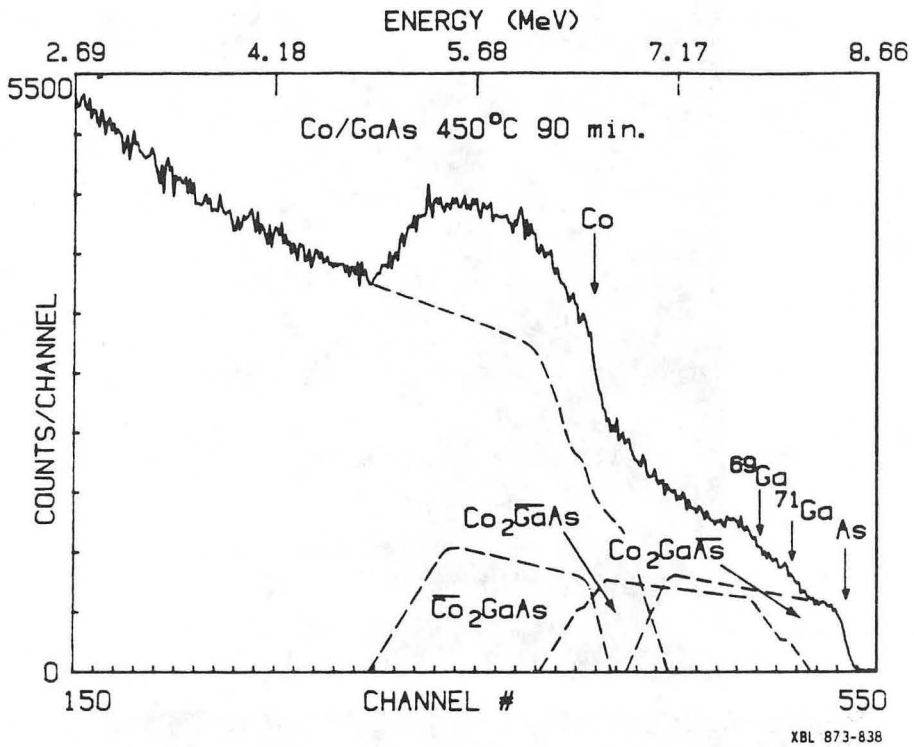

Figure 3.2 HIRBS spectrum of Co/GaAs sample annealed at 450 °C for 90 min. Deconvolution (dashed spectrum) of this spectrum shows a reacted layer with a concentration ratio of Co to GaAs ≈2.

however, indicate the formation of two binary phases: CoGa and CoAs when the annealing temperature is higher than 500 °C. The presence of these binary phases is further confirmed by TEM. Figure 3.3 shows the transmission electron diffraction (TED) pattern with the corresponding bright field (BF) image from 120 Å Co/GaAs sample annealed at 600 °C for 20 min. Cubic CoGa phase with CsCl structure (a_o=2.878 Å) and the orthorhombic CoAs phase (a_o=5.278 Å, b_o=5.868 Å and c_o=3.489 Å) are clearly identified in the electron diffraction pattern. The plan-view TEM micrograph in Figure 3.3 shows that the reacted film consists of a

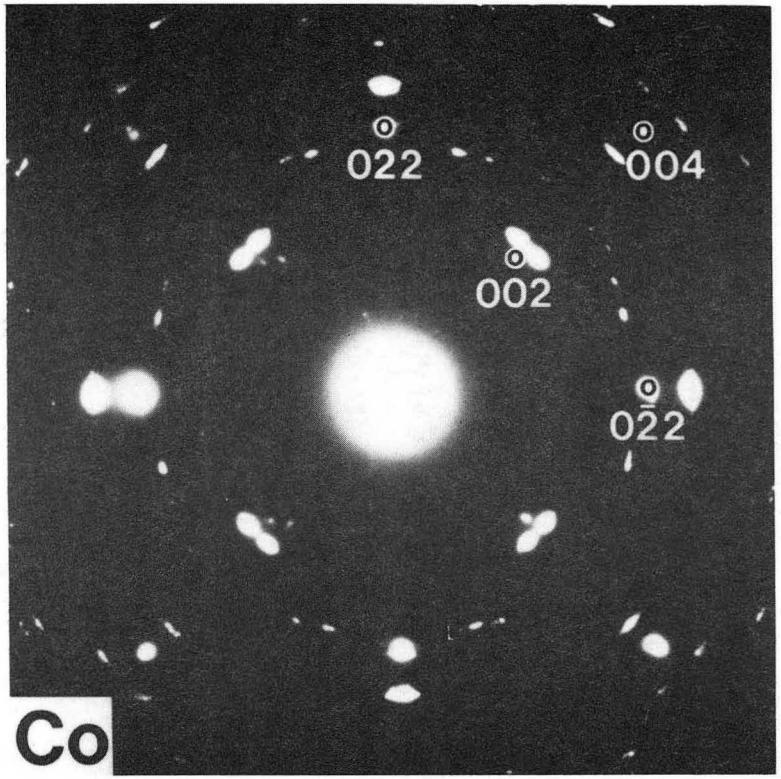

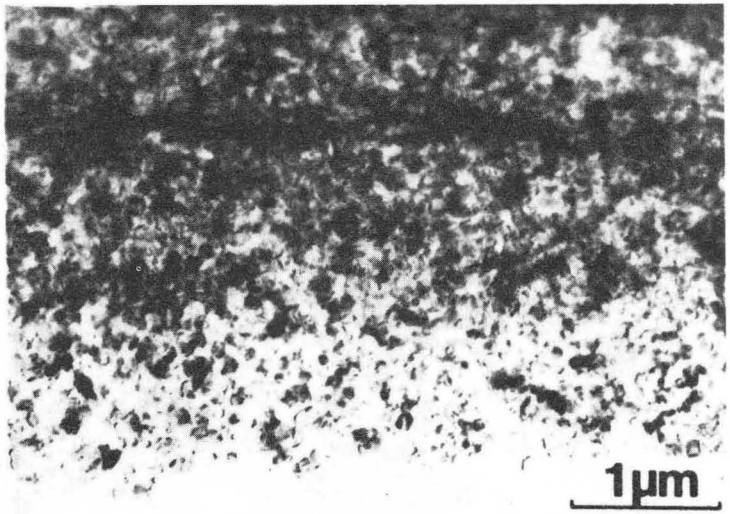

XBB 873-2136

loosely connected network of fine grains (~1000 Å in diameter) of CoGa and CoAs. The fact that both the Ga and As surface signals are present in the HIRBS spectra together with the appearance of strong crystallographic texture for both CoGa and CoAs phases in the TED patterns for samples annealed at temperatures higher than 500°C lead to the conclusion that the two binary phases are not vertically separated and that both phases are in intimate contact with the GaAs substrate. The following orientation relationships are observed from the TED patterns:

$$\langle 100\rangle_{CoGa} \parallel \langle 100\rangle_{GaAs}$$

$$\{011\}_{CoGa} \parallel \{0\bar{1}1\}_{GaAs}$$

$$\langle 010\rangle_{CoAs} \parallel \langle 011\rangle_{GaAs}$$

$$\{101\}_{CoAs} \parallel \{011\}_{GaAs}$$

These binary phases are the stable final phases which are formed from the disintegration of the ternary phase at high temperatures (>500°C).

The rate of the solid-state reactions of the Co/GaAs system is also measured with HIRBS by monitoring the amount of GaAs reacted for samples undergoing isochronal annealing. Figure 3.4 illustrates the result of one of these measurements at 300°C. It shows that the rate of the substrate GaAs consumed during the reaction is proportional to the square root of the annealing time, i.e. we observed a parabolic reaction rate. The same law is observed for Co/GaAs samples annealed at 400, 450 and 500°C. This indicates that the Co/GaAs interface reactions are dominated by a diffusion limited process. Diffusivities

Figure 3.3 (previous page) Transmission electron diffraction (TED) pattern with the corresponding bright field image of 120 Å Co/GaAs sample annealed at 600°C for 20 min.

D which are direct functions of the diffusion coefficients for different temperatures are deduced from the slopes of the plots such as the one shown in Figure 3.4. An activation energy of ≈1.68±0.10 eV is obtained from the slope of the Arrhenius plot of D as a function of the annealing temperature measured in degree Kelvin.

RBS measurements on Co/GaAs samples annealed at >400 °C without oxide capping show that cobalt oxide layers are present on the top surface of the samples. In fact, a bluish layer which is believed to be Co_2O_3 can be observed on these samples. This shows that oxide capping is essential for metal/GaAs annealing not only to reduce As vaporization but also in preventing oxidation of the more electro-positive metals (such as Co, Ni and the refractory metals).

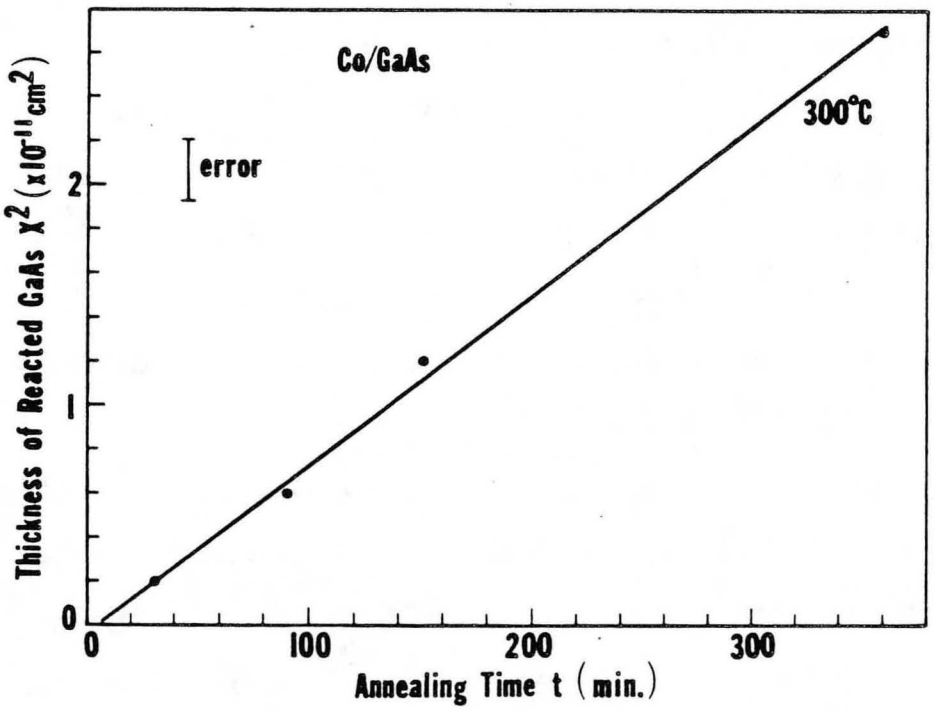

XBL 872-567

Figure 3.4 A plot of the square of the reacted GaAs thickness as measured by HIRBS versus the annealing time for Co/GaAs annealed at 300 °C. A linear relationship is observed in the plot indicating a diffusion controlled process.

3.2 Rh/GaAs

Figure 3.5(a) shows a series of glancing angle RBS spectra of 150 Å Rh/GaAs samples as deposited and annealed at 300, 400, and 500 °C for 20 min. An interface reaction is detected for the sample annealed at 300 °C for 20 min. It is estimated from the RBS spectrum that ~45 Å of Rh have reacted with ~75 Å of GaAs. The ratio of the amount of Rh to that of GaAs in the reacted layer is therefore ≈2.0±0.1. The deconvolution of the RBS spectrum of the sample annealed at 400 °C for 20 min is shown in Figure 3.5(b). We see that the entire 150 Å of Rh film have reacted in this sample resulting in the formation of a uniform layer containing all three constituents (Rh, Ga and As). Energy loss and yield ratio analyses of the spectrum give [Rh]:[Ga]:[As]≈2:1:1 for this reacted layer. RBS measurements on samples annealed at 500 °C for 20 min. show that a uniform reacted layer with [Rh]:[Ga]:[As]≈1.6:1:1 is formed. No new features are detected for samples annealed at temperatures greater than 500 °C. Our results suggest that the intermediate phase(s) formed at temperatures lower than 400 °C has an overall Rh concentration higher than that of the final phase(s) of the system.

HIRBS spectra of 600 Å Rh/GaAs samples as deposited and annealed at 700 °C for 20 min are shown in Figure 3.6. Complete reaction of the Rh film with the GaAs substrate is evident for the sample annealed at 700 °C for 20 min. The deconvolution of this spectrum shown in Figure 3.6 (dashed lines) indicates that two distinct layers of Rh-Ga and Rh-As compounds are formed on GaAs. Yield ratio and energy loss analyses

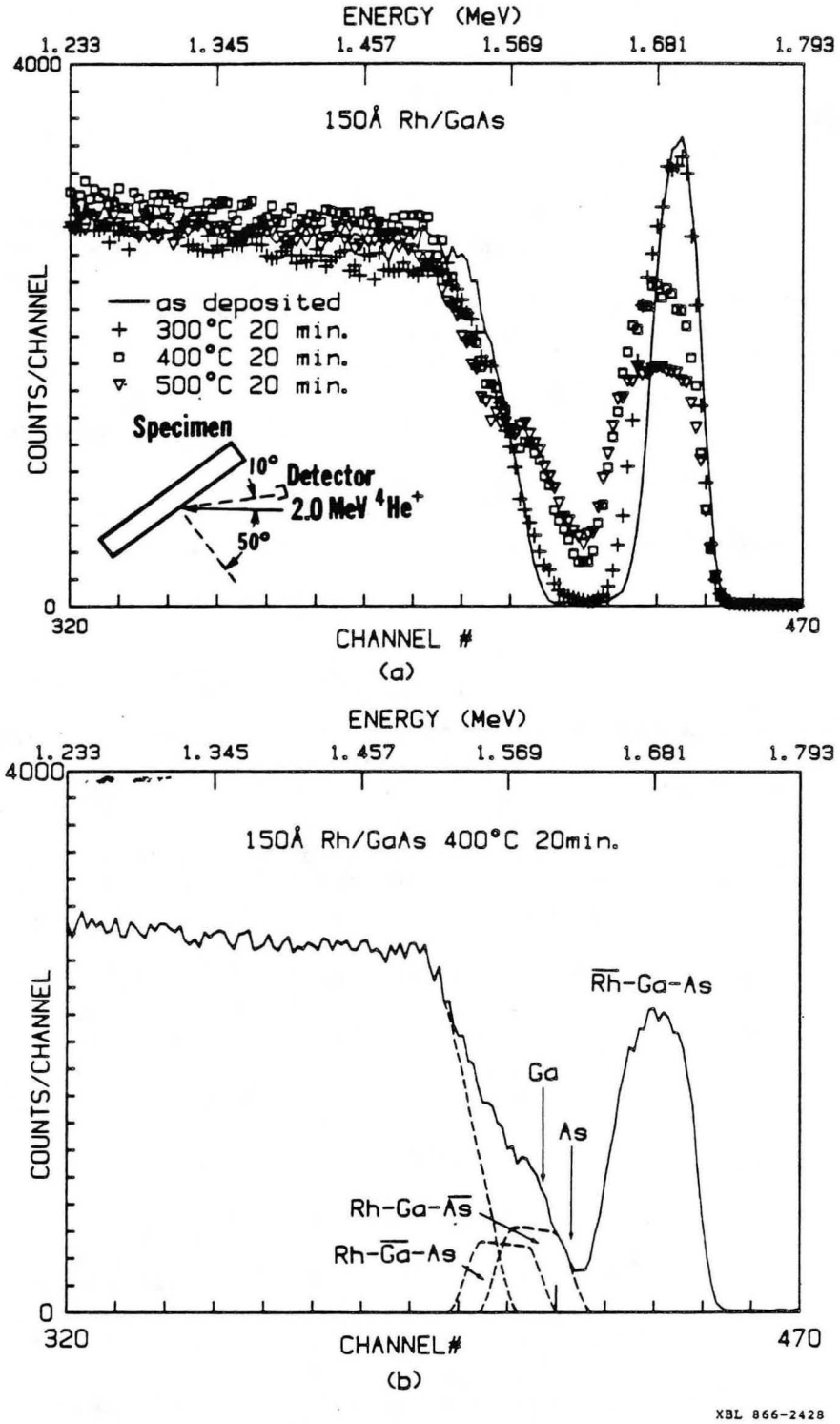

Figure 3.5 (a) Glancing angle RBS spectra of 150 Å Rh/GaAs samples as deposited and annealed at 300, 400 and 500 °C for 20 min. The back-scattering geometry is also shown in this figure. (b) Deconvolution of the RBS spectrum of the sample annealed at 400 °C for 20 min.

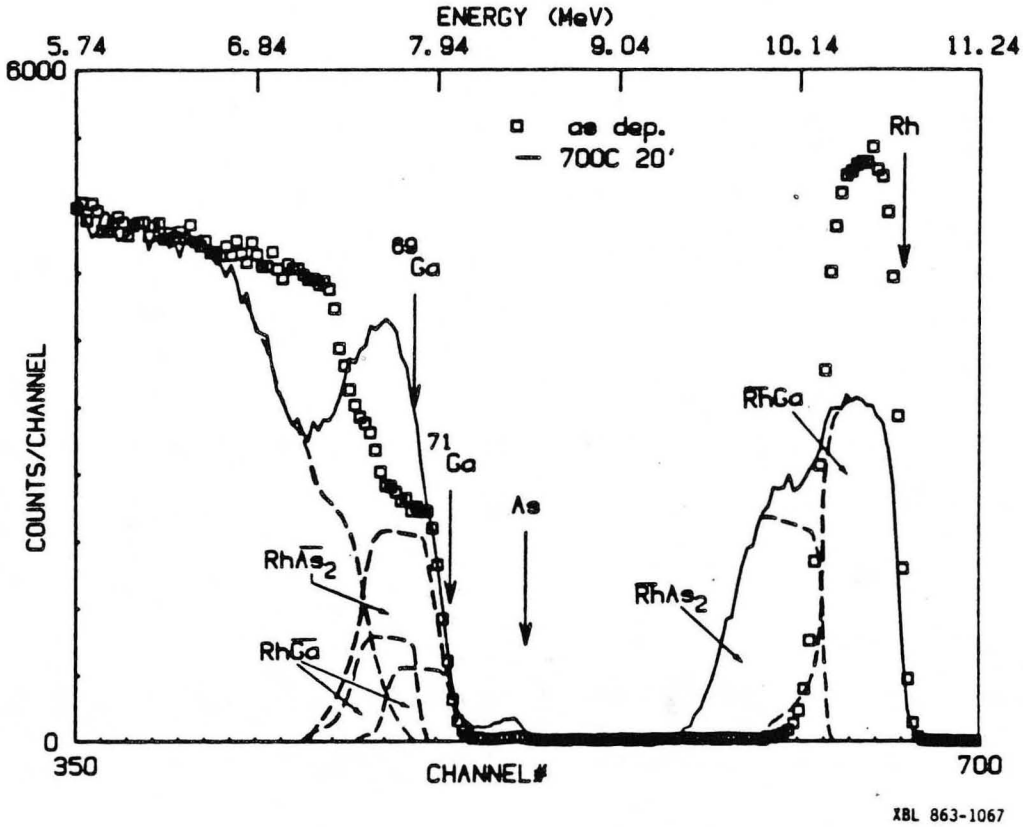

Figure 3.6 HIRBS spectra of 600 Å Rh/GaAs samples as deposited and annealed at 700 °C for 20 min. Deconvolution of the spectrum of the annealed sample is also shown (dashed lines).

of the HIRBS spectrum suggest that the top layer is primarily a compound of Rh and Ga with [Rh]:[Ga]≈1:1 while the interface layer is composed mainly of Rh and As with [Rh]:[As]≈1:2. The ratio of the amount of reacted Rh to that of GaAs deduced from the spectrum is ≈1.5. Therefore the reaction:

$$3\ Rh + 2\ GaAs \rightarrow 2\ RhGa + RhAs_2$$

is consistent with the HIRBS measurement for the sample annealed at 700 °C. This is in good agreement with the results of the 150 Å Rh/GaAs sample which give an end phase(s) with [Rh]:[GaAs]≈1.6:1. In addition

to the layered structure detected by HIRBS, as much as 15% of RhGa is found in the $RhAs_2$ layer. Similarly ~10% of the As (possibly in the form of $RhAs_2$) is found in the RhGa layer.

The XRD spectrum from the 600 Å Rh/GaAs sample annealed at 350°C for 120 min shows the existence of two new phases, namely RhGa (CsCl structure with a_o=3.01 Å) and RhAs (orthorhombic structure with a_o=5.62 Å, b_o=3.58 Å and c_o=6.00 Å) with a large amount of unreacted Rh. Only two phases are detected in the XRD spectrum from the sample annealed at 700°C: RhGa and $RhAs_2$ (monoclinic structure with a_o= 6.041 Å, b_o=6.080 Å, c_o=6.126 Å and β=114°20').

Fine grains (500 Å in diameter) are observed for the reacted layer in the TEM BF image of the 150 Å Rh/GaAs annealed at 600°C for 20 min shown in Figure 3.7. Electron diffraction from this film shows strong texture for RhGa with orientation relationship,

$$\langle 0\bar{1}1\rangle_{RhGa} \parallel \langle 011\rangle_{GaAs}$$

$$\{011\}_{RhGa} \parallel \{100\}_{GaAs}.$$

Note that this orientation relationship is different from the isostructural compound CoGa. The only obvious explanation for this difference is that the misfit between $\{100\}_{MGa}$ and $\{100\}_{GaAs}$ is sufficiently greater for RhGa (6.5%) than for CoGa (1.8%) so that the simple unrotated orientation relationship with GaAs is not energetically favorable for RhGa. The second reacted phase identified by TED is $RhAs_2$, in agreement with the XRD data. The $RhAs_2$ phase shows only very weak crystallographic texture.

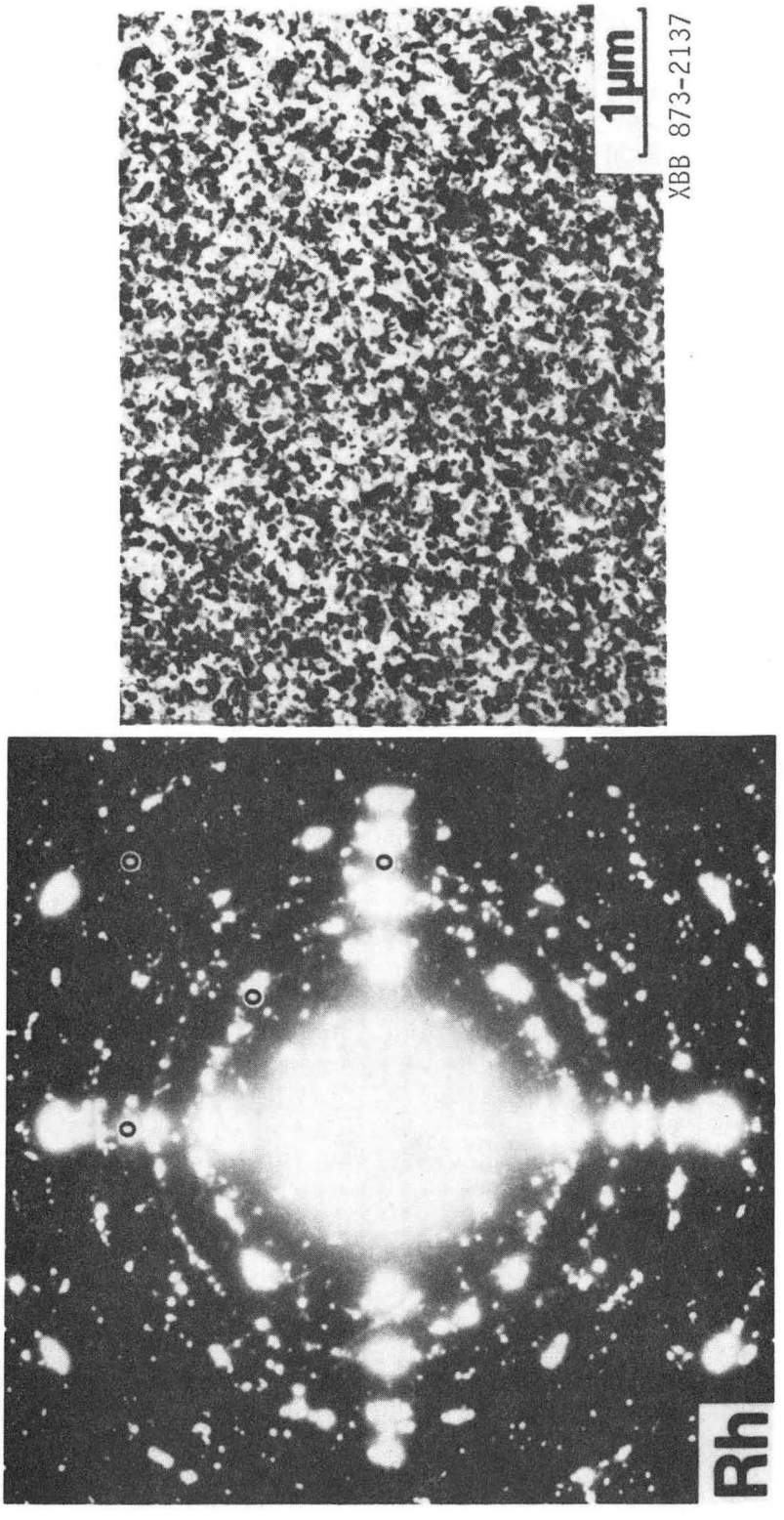

XBB 873-2137

The RBS, HIRBS, XRD and TEM results from the 150 Å and 600 Å Rh films indicate that the system starts to react at annealing temperature as low as 300°C. The initial reaction products are RhGa and RhAs. Annealing at higher temperatures (>400°C) results in the nucleation of a new phase $RhAs_2$. The $RhAs_2$ phase continues to grow at the interface at the expense of the RhAs phase until finally a RhGa/$RhAs_2$/GaAs structure is formed. For thin Rh films (~150 Å) these three phases are laterally separated in order to minimize interface energy when the grain size of these phases is comparable to or greater than the film thickness. This effect of grain size on phase stratification is also observed in other systems and will be discussed in more detail later.

Plots of the square of the reacted GaAs thickness in as a function of the annealing time for different temperatures are shown in Figure 3.8. A parabolic reaction rate is evident from this figure. The Arrhenius plot of the diffusivity D and the annealing temperature T shown in Figure 3.9 follows an exponential expression of the form $D \sim \exp(-\Delta E/kT)$ where ΔE is the activation energy of reactions and k is the Boltzmann constant. The slope of this plot yields an activation energy of $\approx 1.65 \pm 0.20$ eV for Rh/GaAs reactions which is similar to that obtained for Co/GaAs.

Figure 3.7 (previous page) TED pattern and the corresponding bright field image of 150 Å Rh/GaAs sample annealed at 600°C for 20 min indicating fine grains (~500 Å) of RhGa and $RhAs_2$ phases.

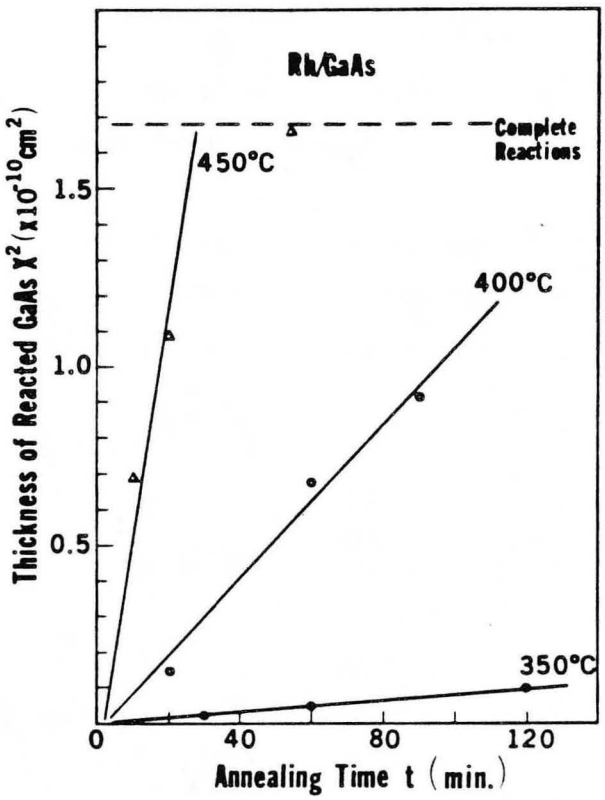

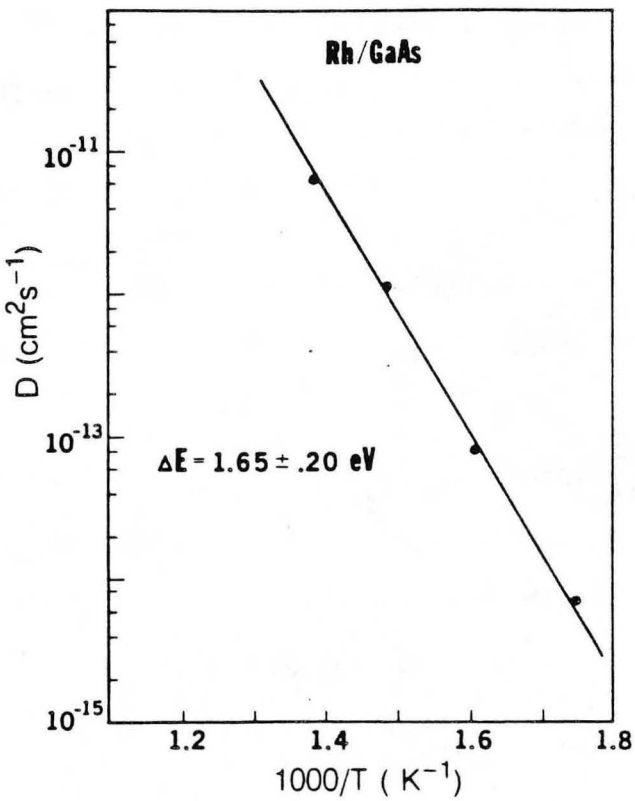

Figure 3.8 Figure 3.9

Figure 3.8 Plots of the square of the reacted GaAs thickness as measured by HIRBS versus the annealing time for 600 Å Rh/GaAs samples annealed at 350, 400 and 450 °C.

Figure 3.9 A plot of ln D, the diffusivity for Rh/GaAs reactions deduced from the slopes of the plots in Figure 3.8 versus the reciprocal of the annealing temperature in degree Kelvin.

3.3 Ir/GaAs

A two stage reaction is detected with conventional RBS in the 550 Å Ir/GaAs system. Initial interfacial interaction starts during annealing at 500 °C. Complete consumption of the entire Ir film is observed for the sample annealed at 650 °C for 80 min (stage 1). The

final reaction is completed after annealing at 700°C for 16 min (stage 2). Figure 3.10 shows the RBS spectra from 550Å Ir/GaAs samples as deposited, annealed at 650°C for 80 min and 700°C for 16 min. It can be deduced from the Ir signals in the spectra that two-layer structures are formed in both of the annealed samples. The interface layers in these two annealed cases have similar Ir content while the top layer in the sample annealed at 650°C has higher Ir content than that of the sample annealed at 700°C. The GaAs signals in the backscattering spectra show no significant amount of As present in the top layers in both annealed samples. The deconvolutions of the RBS spectra from the two annealed samples are shown in Figure 3.11. Well defined structures with Ir-As phase at the interface and Ir-Ga phase on top are evident.

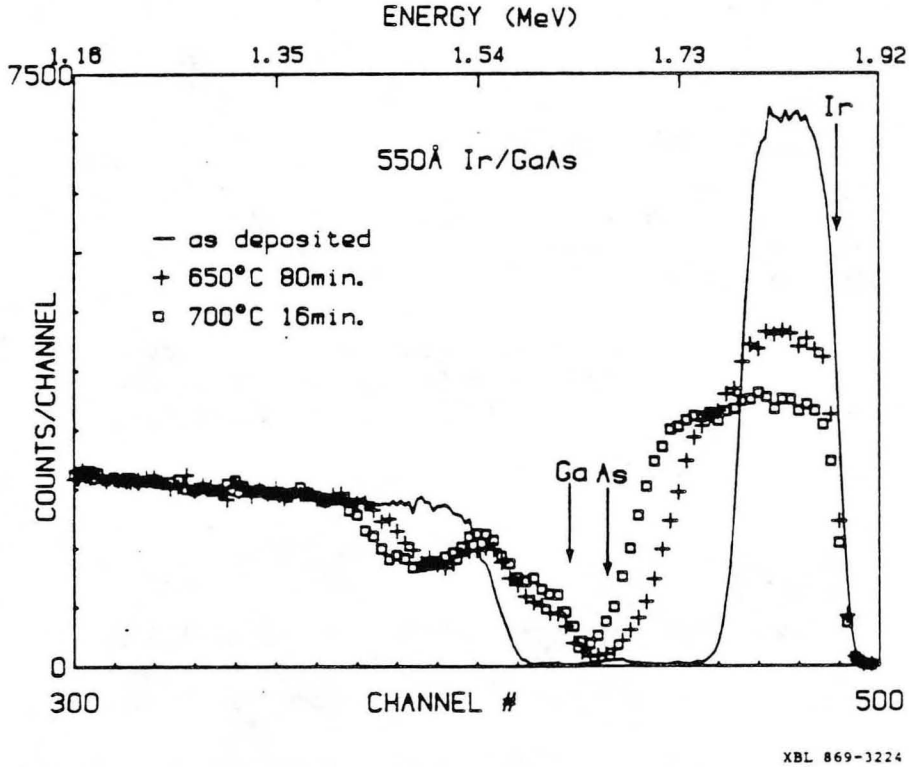

Figure 3.10 A series of RBS spectra of 550 Å Ir/GaAs samples as deposited, annealed at 650°C for 80 min and at 700°C for 16 min.

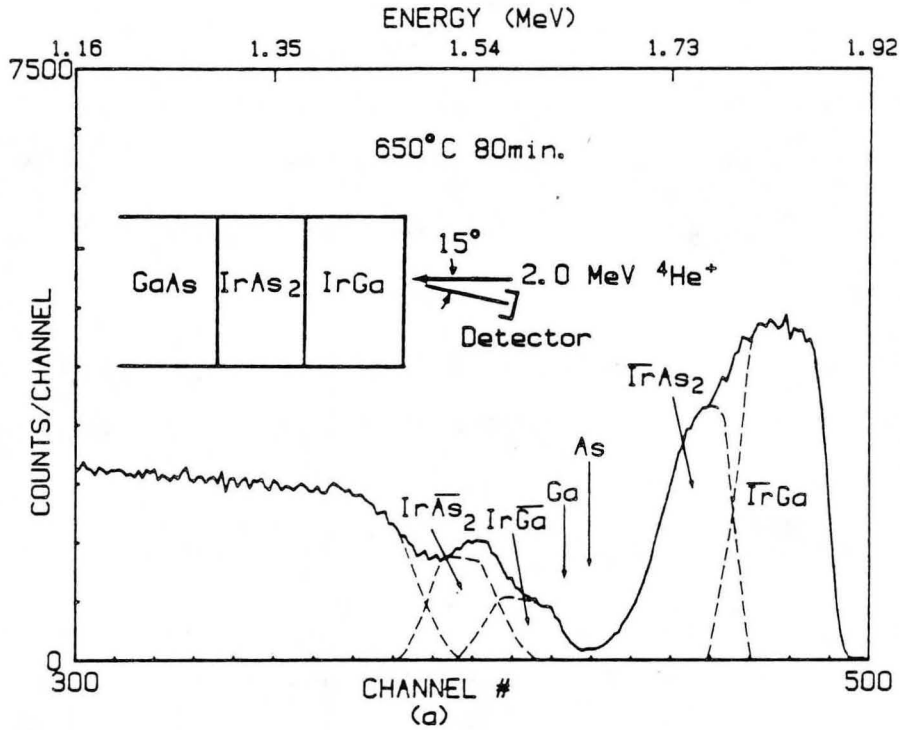

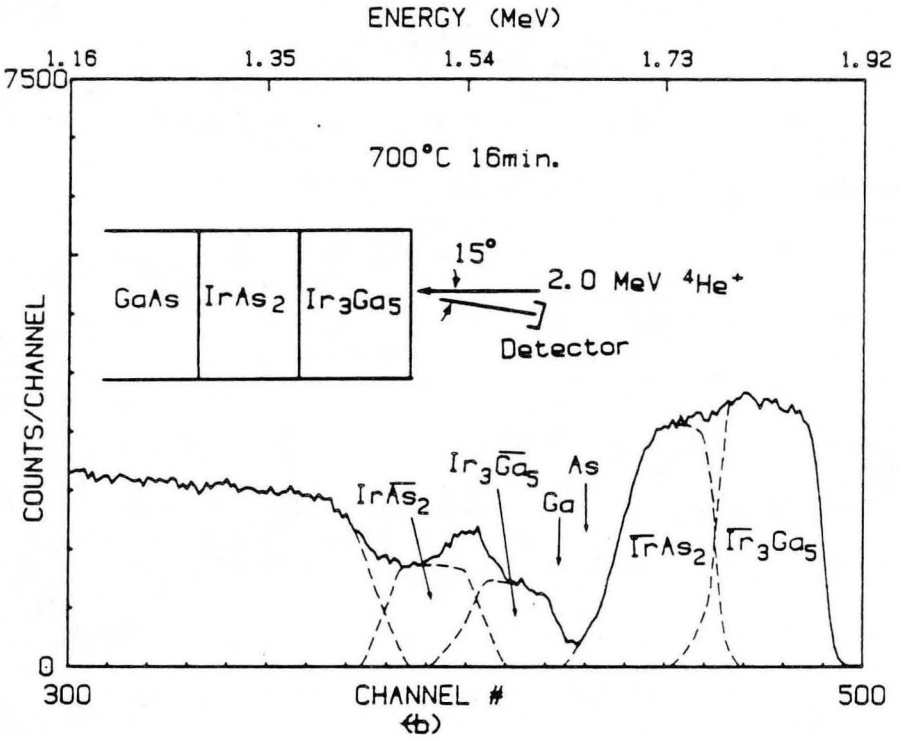

XBL 8612-4949

Figure 3.11 Deconvolution of the RBS spectra of 550 Å Ir/GaAs samples annealed at 650 °C for 80 min (a) and at 700 °C for 16 min (b). The inserts show the structures of the corresponding samples and the back-scattering geometry.

Height ratio analyses of the RBS spectra gives [Ir]:[Ga]≈1:1 and [Ir]:[As]≈1:2 for the sample annealed at 650°C for 80 min and [Ir]:[Ga]≈0.6:1 and [Ir]:[As]≈1:2 for the sample annealed at 700°C for 16 min. Overall ratios of the reacted Ir and GaAs are also obtained from energy loss analysis of the two RBS spectra in Figure 3.11 and they yield [Ir]:[GaAs]≈1.5:1 for stage 1 reactions and ≈1.1:1 for stage 2 reactions. These data are consistent with the following reactions:

$$3\ Ir + 2\ GaAs \rightarrow 2\ IrGa + IrAs_2 \text{ (stage 1), and}$$

$$11Ir + 10\ GaAs \rightarrow 2Ir_3Ga_5 + 5IrAs_2 \text{ (stage 2).}$$

XRD measurements on 550 Å Ir/GaAs samples annealed at temperatures ranging from 500 to 650°C indicate the existence of two phases : cubic IrGa (a_o=3.004 Å) with CsCl structure and monoclinic $IrAs_2$ (a_o=6.060 Å, b_o=6.071 Å, c_o=6.158 Å and β=113°16'). Figure 3.12 (a) and (b) show two XRD spectra from samples annealed at 650°C for 20 and 80 min. Note that the IrGa and $IrAs_2$ diffraction peaks grow at the expense of the Ir peaks for longer annealing time at 600°C. After annealing at 700°C for 16 min the IrGa diffraction peaks disappear in the XRD spectrum as shown in Figure 3.12(c). A new set of diffraction peaks appears in this spectrum. This set of diffraction data is in reasonable agreement with those of the tetragonal Ir_3Ga_5 phase[4] (a_o=5.823 Å and c_o=14.20 Å).

The RBS and XRD results suggest that the final stable phases for thin film Ir/GaAs solid phase reactions are the Ir_3Ga_5 and $IrAs_2$ phases. Intermediate phase IrGa decomposes at temperatures higher than 650°C. Moreover, vertical phase separation with a layer of $IrAs_2$ in intimate contact with GaAs and the Ir-Ga phase on top of the $IrAs_2$ layer is always observed in this system.

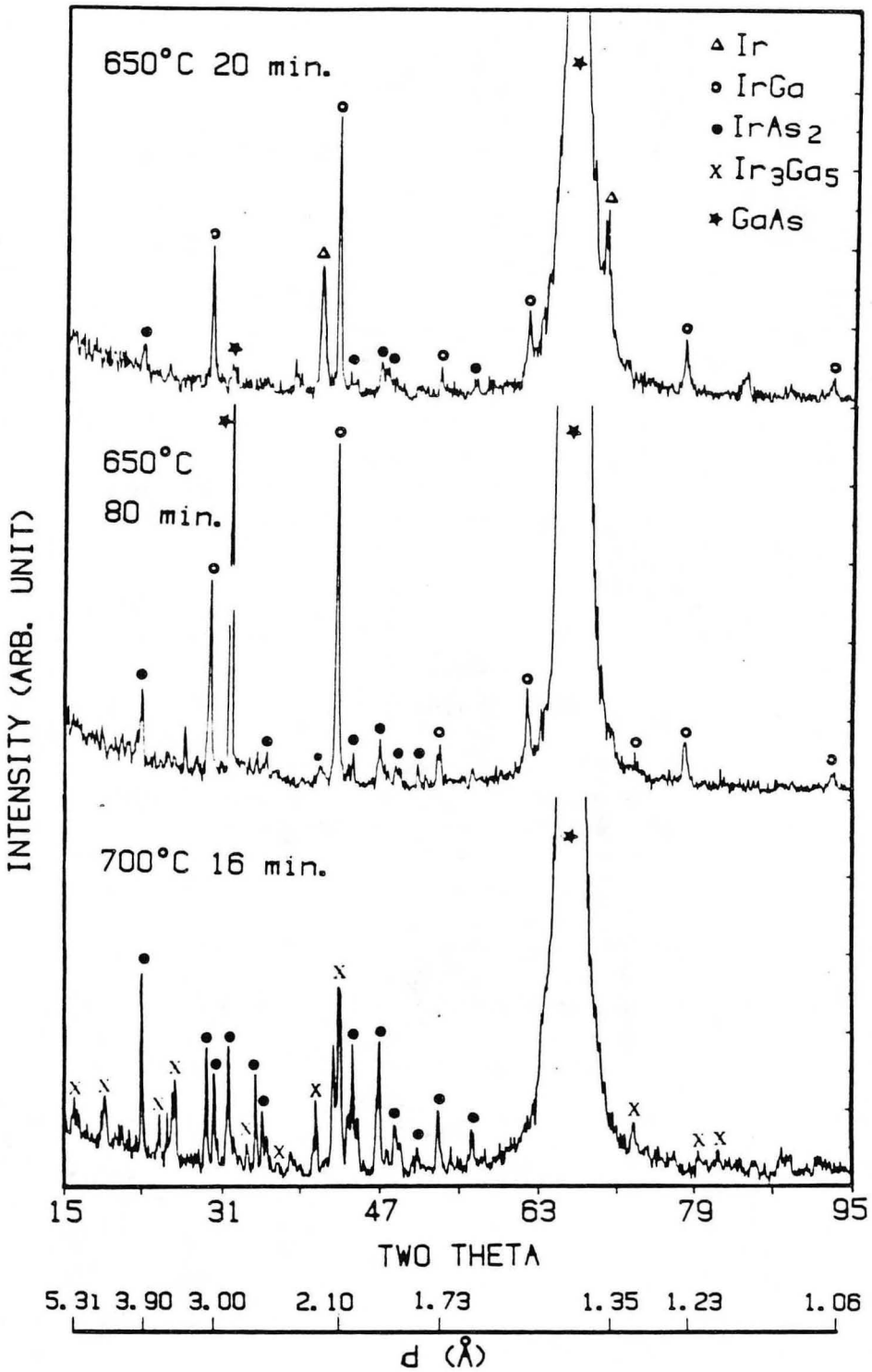

XBL 8612-4948

Figure 3.12 XRD spectra of 550 Å Ir/GaAs samples annealed at 650°C for 20 min (a), at 650°C for 80 min (b) and at 700°C for 16 min (c).

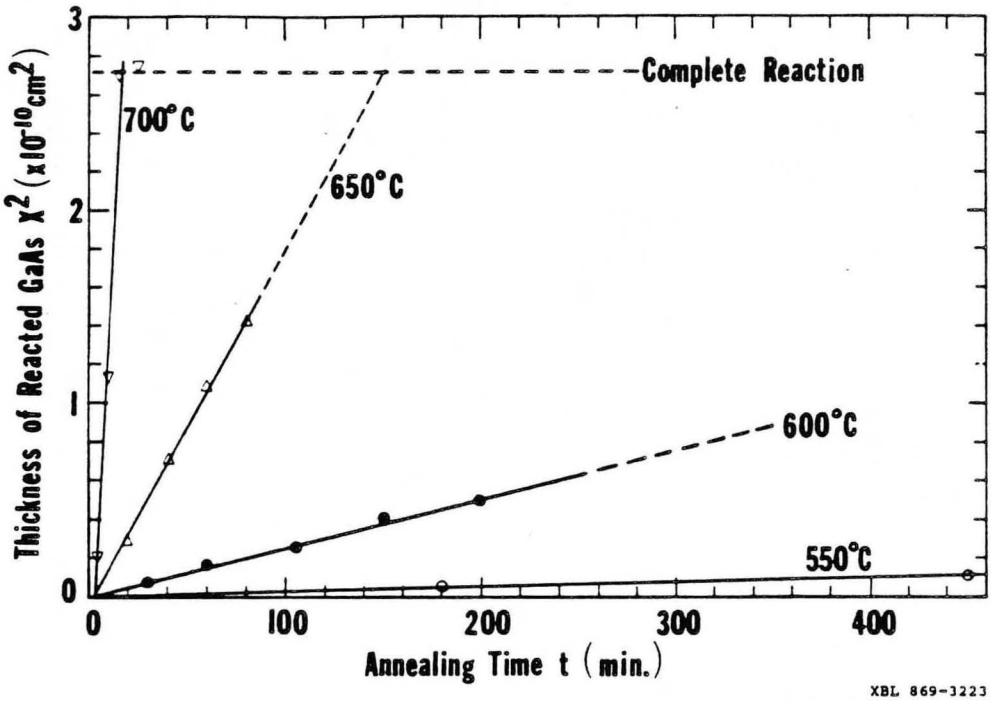

Figure 3.13 Plots of the square of the reacted GaAs thickness measured by RBS as a function of the annealing time for Ir/GaAs samples annealed at different temperatures.

Figure 3.13 shows plots of the square of the reacted GaAs thickness in cm measured by RBS as a function of the annealing time for different temperatures. All three plots in this figure show a linear dependence indicating that the reactions at the Ir/GaAs interface follow parabolic rates and thus follow a diffusion controlled process. A plot of ln D versus the inverse absolute annealing temperature shown in Figure 3.14, gives an activation energy of 3.15±0.20 eV for Ir/GaAs solid phase reactions. This value of ΔE is significantly higher than those measured for other near noble metal/GaAs reactions. Comparisons and discussions of the kinetics of different system will be given at the end of this chapter.

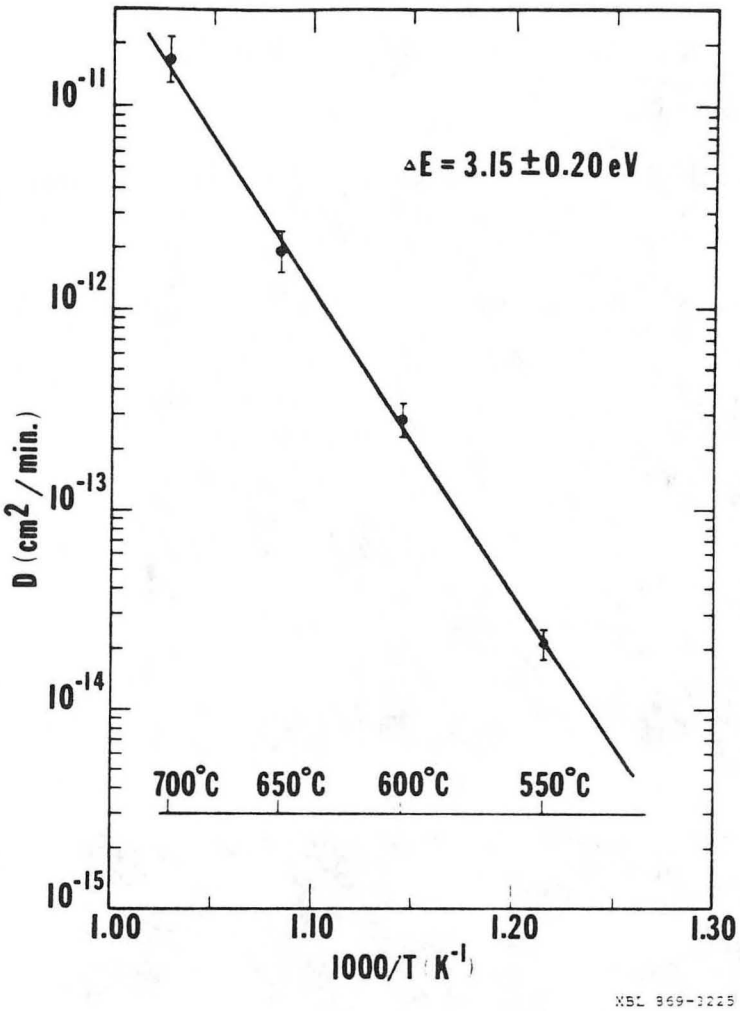

Figure 3.14 A plot of ln D, the diffusivity for Ir/GaAs reactions deduced from the slopes of the plots in Figure 3.13, versus the reciprocal of the annealing temperatures in degree Kelvin.

XRD spectra from the 550 Å Ir/GaAs samples annealed at 700°C for 9 min (not shown) and 16 min (Figure 3.12(c)) reveal that unreacted Ir, IrGa and $IrAs_2$ are present in the former but Ir_3Ga_5 and $IrAs_2$ result in the latter sample. The fact that the formation of the Ir_3Ga_5 layer forms at such a rapid rate suggests that the process may be nucleation controlled. This has been observed in the formations of $NiSi_2$ [Reference 5], $IrSi_3$ [Reference 6], Rh_4Si_5, Rh_3Si_4 [Reference 7] and

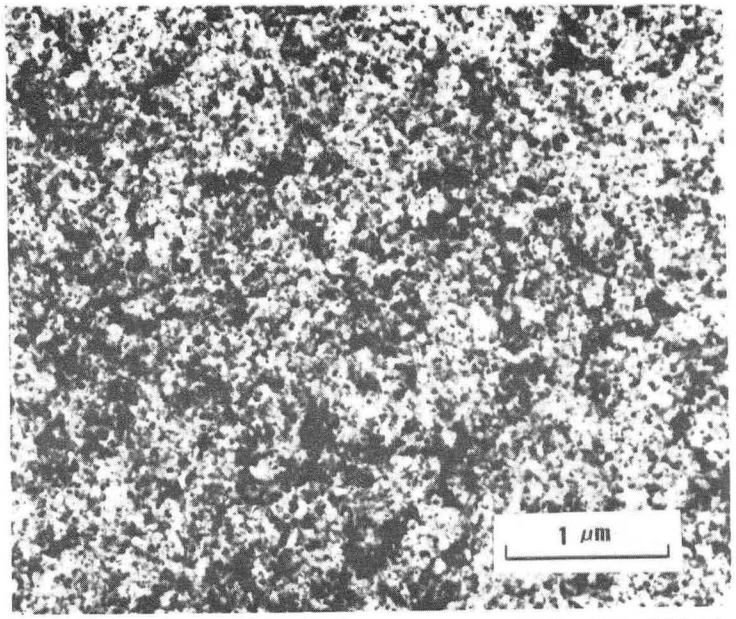

XBB 868-6001A

the rare earth metal silicides[8,9]. This process happens at high temperatures (usually higher than 700 °C except for the rare earth metal silicides) when the diffusing atoms are so mobile that diffusion is very rapid. As a result the growth is no longer controlled by diffusion but is controlled by the nucleation process which starts suddenly at the interface.

The electron diffraction pattern and the BF image obtained with TEM on 100 Å Ir/GaAs sample annealed at 600 °C for 20 min are shown in Figure 3.15. The presence of the Ir_3Ga_5 and the $IrAs_2$ phases are revealed from the TED pattern. Since thinner film promotes a higher rate of reaction, it is not surprising to find the final stable phases at temperatures below 700 °C. Very fine grains (~100 to 200 Å) are formed in the reacted layer as noticed in the BF image in Figure 3.15. Strong texturing is observed in the diffraction pattern only for the $IrAs_2$ phase with the orientation relationship:

$$\langle 5\bar{2}1\rangle_{IrAs_2} \parallel \langle 100\rangle_{GaAs}$$
$$\{11\bar{3}\}_{IrAs_2} \parallel \{011\}_{GaAs}$$

The fact that the Ir_3Ga_5 phase bears no orientation relationship with the GaAs substrate suggests a layer sequence of $Ir_3Ga_5/IrAs_2/GaAs$ for this sample.

Figure 3.15 (previous page) TED pattern of 100 Å Ir/GaAs sample annealed at 600 °C for 20 min with the corresponding TEM bright field image.

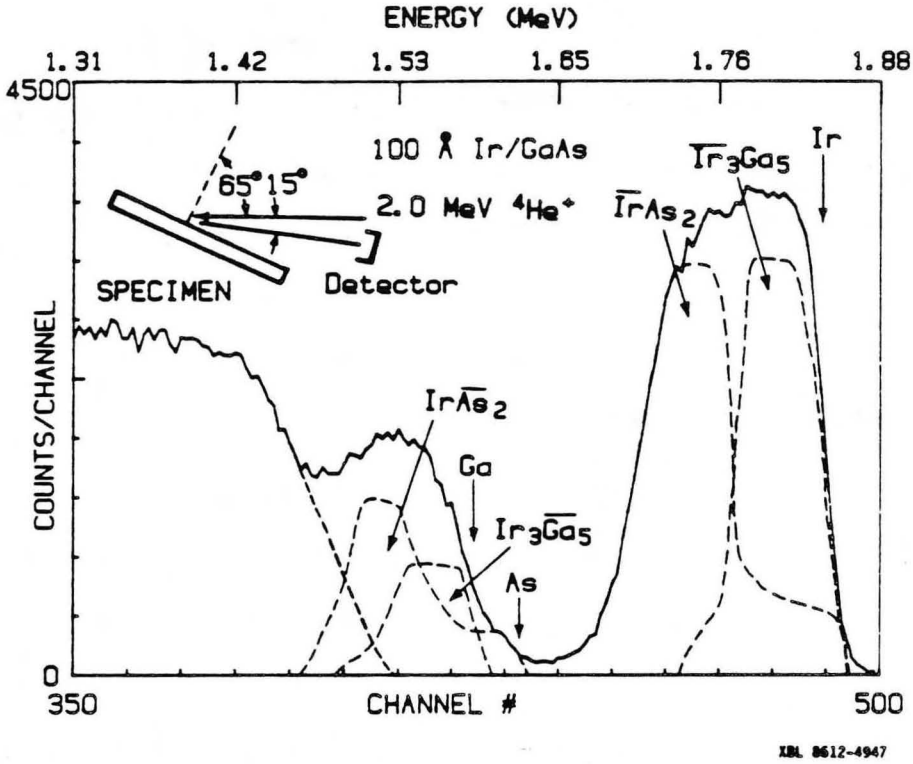

Figure 3.16 Glancing angle RBS spectrum of 100 Å Ir/GaAs sample annealed at 600 °C for 20 min. The deconvolution of the spectrum is also shown in the figure (dashed spectrum). The insert shows the backscattering geometry.

A glancing angle RBS spectrum from 100 Å Ir/GaAs sample annealed at 600 °C for 20 min is shown in Figure 3.16. Deconvolution of the spectrum (dashed spectrum) clearly confirms the layered structure as interpreted from the TEM results. Interpenetration of the two phases can also be deduced from the spectrum. Comparing with the thicker film case in which a distinct layered structure is always preserved, perfect distinction between the layers is lost in the very thin films. This indicates that interface energy plays an important role in the distribution of the phases. When the reacted film thickness becomes comparable to the grain size, phase stratification becomes thermodynamically

less favorable. This effect has also been observed in the thin film Rh/GaAs and Co/GaAs systems discussed in the last two sections. Since the reacted film in this system has a thickness of ~400 Å and the grain size of the reacted phase(s) is ~150 Å in diameter, phase stratification results.

3.4 Ni/GaAs

Because of the success in the fabrication of Au-Ge-Ni alloyed ohmic contacts on n-GaAs [References 10-12], the contact metallurgy of this system has generated a lot of interest in the materials science community[13-15]. In order to understand the role of nickel in the ohmic behavior of this contact, investigations on the solid phase reactions of the Ni/GaAs system has attracted much attention recently.

In this study, a thin nickel film of 600 Å thick is found to react completely with the GaAs substrate after annealing at 200°C for 10 min. Figure 3.17 shows the HIRBS spectra of the Ni/GaAs samples as deposited and after annealing at 200°C for 10 min. A uniformly reacted layer with [Ni]:[Ga]:[As] ≈ 3:1:1 can be deduced from the spectrum of the annealed sample in Figure 3.17. The XRD spectrum obtained with the same annealed sample has only two diffraction peaks at d=2.80 Å and 1.40 Å. These peaks can be indexed as the (0111) and (0222) peaks of the hexagonal ternary phase Ni_xGaAs with a_o= 3.90 Å and c_o=5.01 Å. From this XRD pattern, a tentative orientation relationship of :

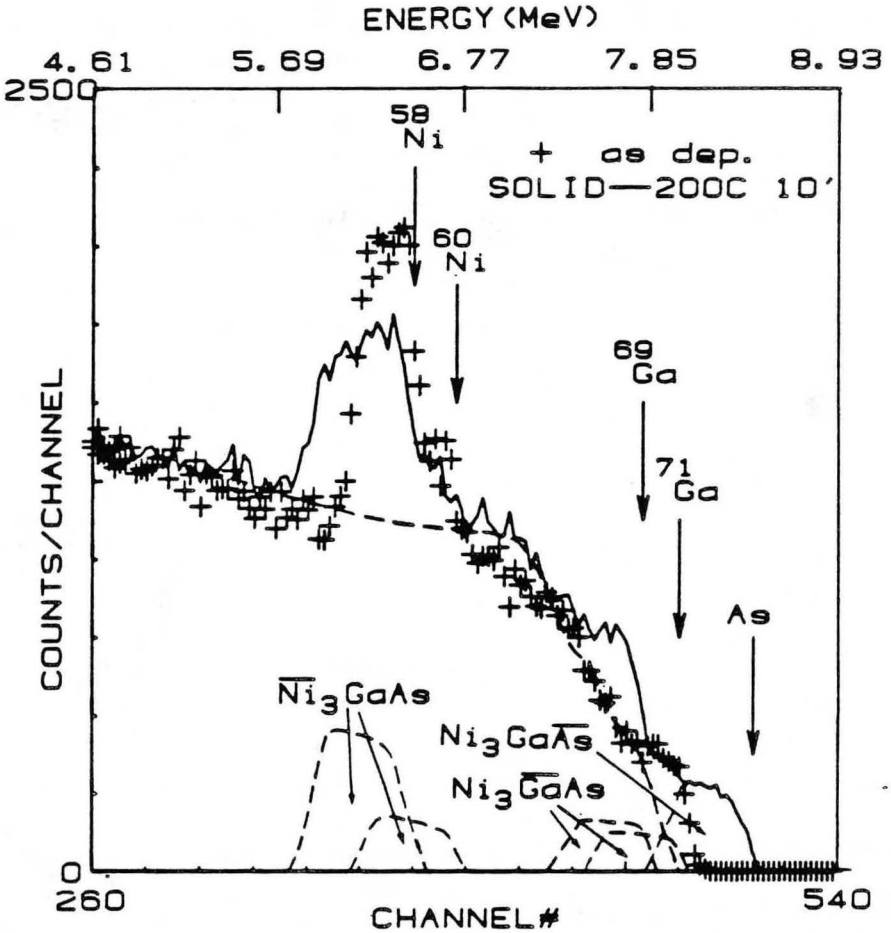

XBL 863-1064

Figure 3.17 HIRBS spectra of 600 Å Ni/GaAs before and after annealing at 200 °C for 10 min. The dashed line shows the deconvoluted spectrum of the annealed sample.

$$\langle 2\bar{1}\bar{1}0\rangle_{Ni_xGaAs} \parallel \langle 011\rangle_{GaAs}$$

$$\{01\bar{1}2\}_{Ni_xGaAs} \parallel \{0\bar{1}1\}_{GaAs}$$

can be established. This orientation relationship agrees well with results reported in the literature[14,16-18].

The deconvolution of the HIRBS spectrum in Figure 3.17 indicates that this ternary phase has a nominal composition Ni_3GaAs. This result

is in good agreement with the findings of Sands et al[17,18] but disagrees with the Ni_2GaAs phase detected by Ogawa[14] and Lahav et al[16] who used sputtering Auger electron spectroscopy (AES) for depth profiling. It is difficult to obtain quantitative results with the AES technique which may be the source for the discrepancy. However, further study would be necessary to unanimously resolve this discrepancy.

HIRBS and XRD measurements on the samples annealed at 400°C for 10 min indicate that the same ternary phase is present in the sample but it becomes less rich in nickel with nominal composition $Ni_{2.4}GaAs$. This result tends to support the hexagonal B8 crystal structure for the Ni_xGaAs phase suggested by Sands et al[17,18] which could possibly tolerate variations in nickel concentration from x=2 to 4. Figure 3.18 is the HIRBS spectrum of the Ni/GaAs sample annealed at 600°C for 10 min. The [Ni]:[Ga]:[As] ratio in the reacted layer can only be estimated from this spectrum and is ~2:1:1. Because the Ni and Ga backscattering signals overlap, this ratio can only be regarded as a rather rough estimate. Two binary phases, hexagonal NiAs (a_o=3.619 Å and c_o=5.034) and cubic β-NiGa (a_o=2.887 Å) are detected by XRD. Since both Ga and As signals are observed at the surface in the HIRBS spectrum, there can be no vertical phase separation of the two binary phases.

TEM investigations on the stable final phase(s) of the Ni/GaAs system have also been carried out. Figure 3.19 shows the TED pattern and the BF image of 120 Å Ni/GaAs system after annealing at 600°C for

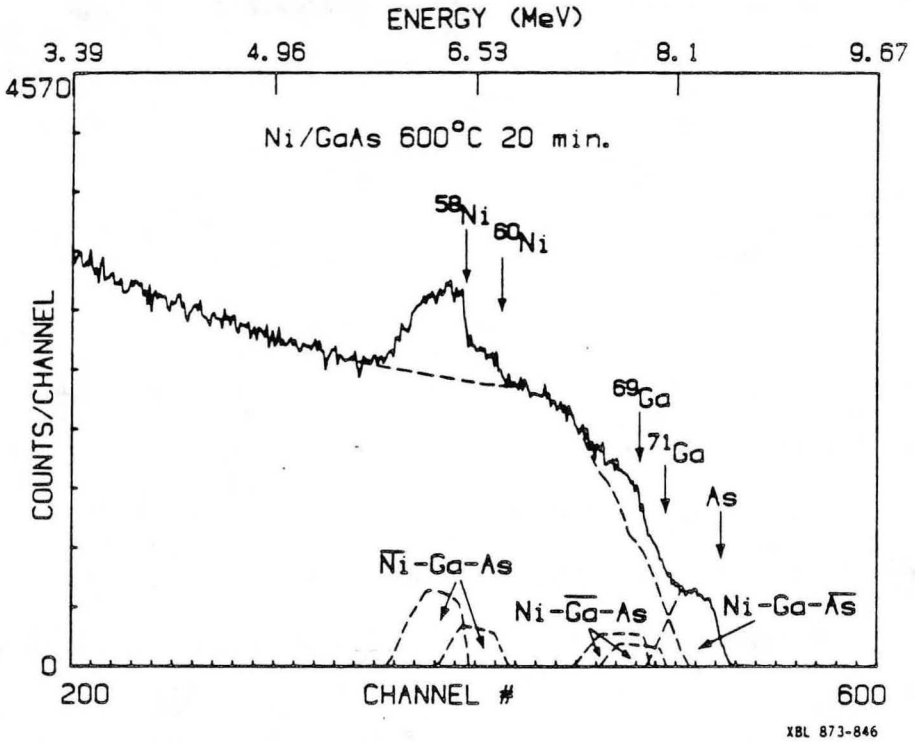

Figure 3.18 HIRBS spectrum of 600 Å Ni/GaAs sample annealed at 600 °C for 20 min. Deconvolution of the spectrum is also shown (dashed lines) indicating the presence of a reacted layer with Ni, Ga and As.

20 min. The presence of the binary NiGa and NiAs phases is confirmed by the TED pattern. The TEM BF image of the sample shows that large grains (~0.5 μm) of NiAs and NiGa are formed during annealing at 600 °C for 20 min. Both binary phases strongly textured, indicating that they are in intimate contact with the GaAs substrate. The following orientation relationships can be established:

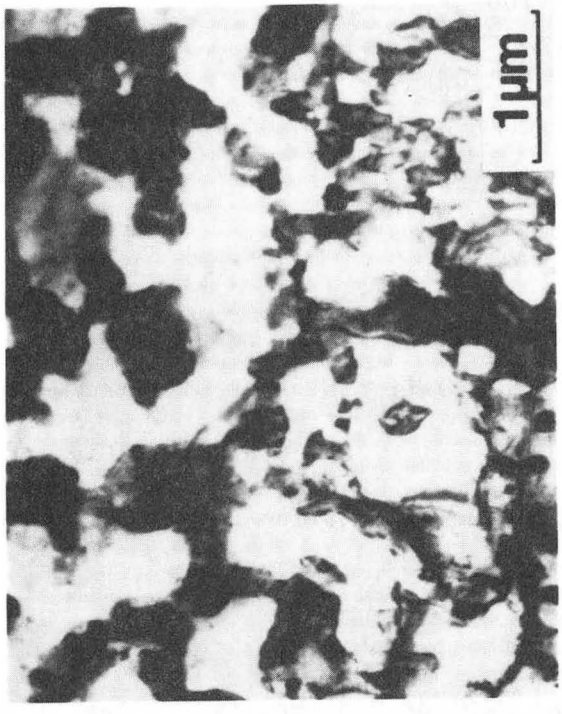

XBB 873-2134

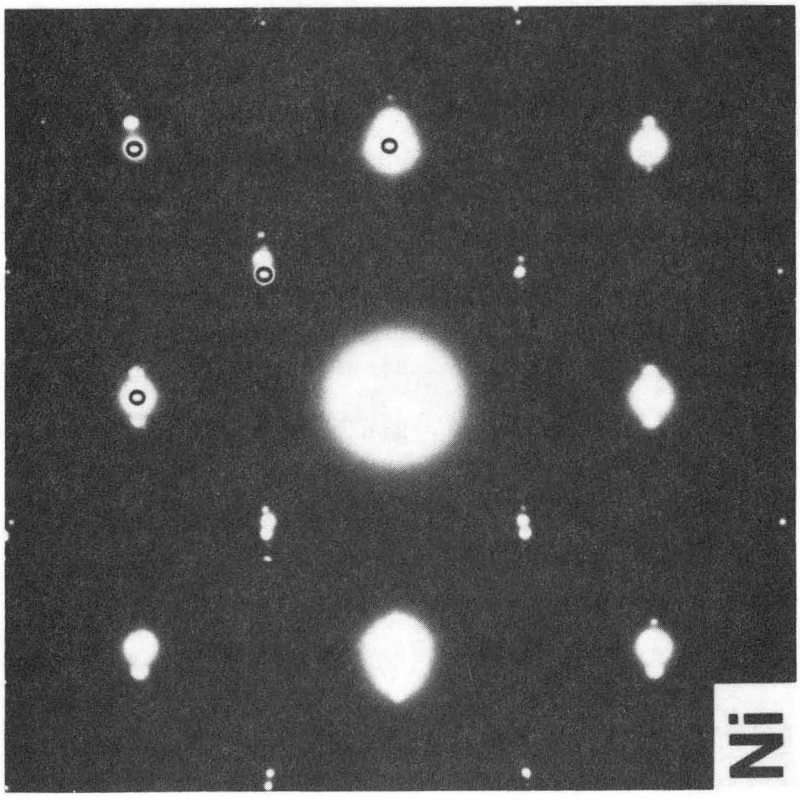

$$\langle 100\rangle_{NiGa} \parallel \langle 100\rangle_{GaAs}$$

$$\{011\}_{NiGa} \parallel \{011\}_{GaAs}$$

and

$$\langle 2\bar{1}\bar{1}0\rangle_{NiAs} \parallel \langle 011\rangle_{GaAs}$$

$$\{01\bar{1}2\}_{NiAs} \parallel \{0\bar{1}1\}_{GaAs}$$

The simple orientation relationships of both the NiGa and CoGa phases with GaAs exist because that they both have CsCl structure with $a_o(MGa) \approx 0.5a_o(GaAs)$. The orientation relationship between the NiAs and GaAs is identical with that of the ternary Ni_3GaAs phase because of the similar structure of the two phases.

From the HIRBS, XRD and TEM results, it can be concluded that the Ni/GaAs contacts are extremely reactive. In fact Sands et al[18] has observed that Ni reacts with GaAs during deposition. The present study reveals that an intermediate phase, Ni_3GaAs is formed during annealing at 200°C. The metal concentration in this ternary phase decreases as the annealing temperature increases up to ~500°C. Above 500°C the ternary phase is unstable and transforms into two binary phases, NiAs and NiGa. Because of the large grain size of these final stable phases, they are only laterally separated. Due to the highly reactive nature of this system, the solid phase reaction kinetics cannot be measured with HIRBS.

Figure 3.19 (previous page) TED pattern and TEM bright field image of 120 Å Ni/GaAs sample annealed at 600°C for 20 min.

3.5 Pd/GaAs

Recently many studies have been carried out on the Pd/GaAs interface because of the following reasons:

1. The development of "sintered" multi-elemental ohmic contacts to GaAs with palladium as one of the components (for example, Pd-Ge/GaAs by Marshall et al[19]) has been very successful; and

2. The Pd-GaAs ternary phases at Pd/GaAs interface during low temperature annealing have been identified. Since these ternary phases are very metal rich, they may be useful in the development of shallow junction contact to GaAs[18,20-23].

Despite the large amount of work done on the Pd/GaAs system, there is still no general agreement on the compositions of the intermediate ternary phases and the stable final binary phases formed in this system.

Interactions between palladium films 130 Å and 700 Å thick and a GaAs substrate have been investigated in this study. HIRBS spectra of 700 Å Pd film on GaAs as deposited and annealed at 350, 400 and 500°C for 10 min respectively are shown in Figure 3.20(a). After annealing at 350°C for 10 min, the entire Pd film has reacted with the GaAs substrate, forming a layer containing all three constituents (Pd, Ga and As). The deconvolution shown in Figure 3.20(b) indicates that the HIRBS data are consistent with the interpretation of a uniform reacted layer with a composition of [Pd]:[Ga]:[As] ≈ 4:1:1. An XRD spectrum from this sample shown in Figure 3.21, indicates that the reacted layer

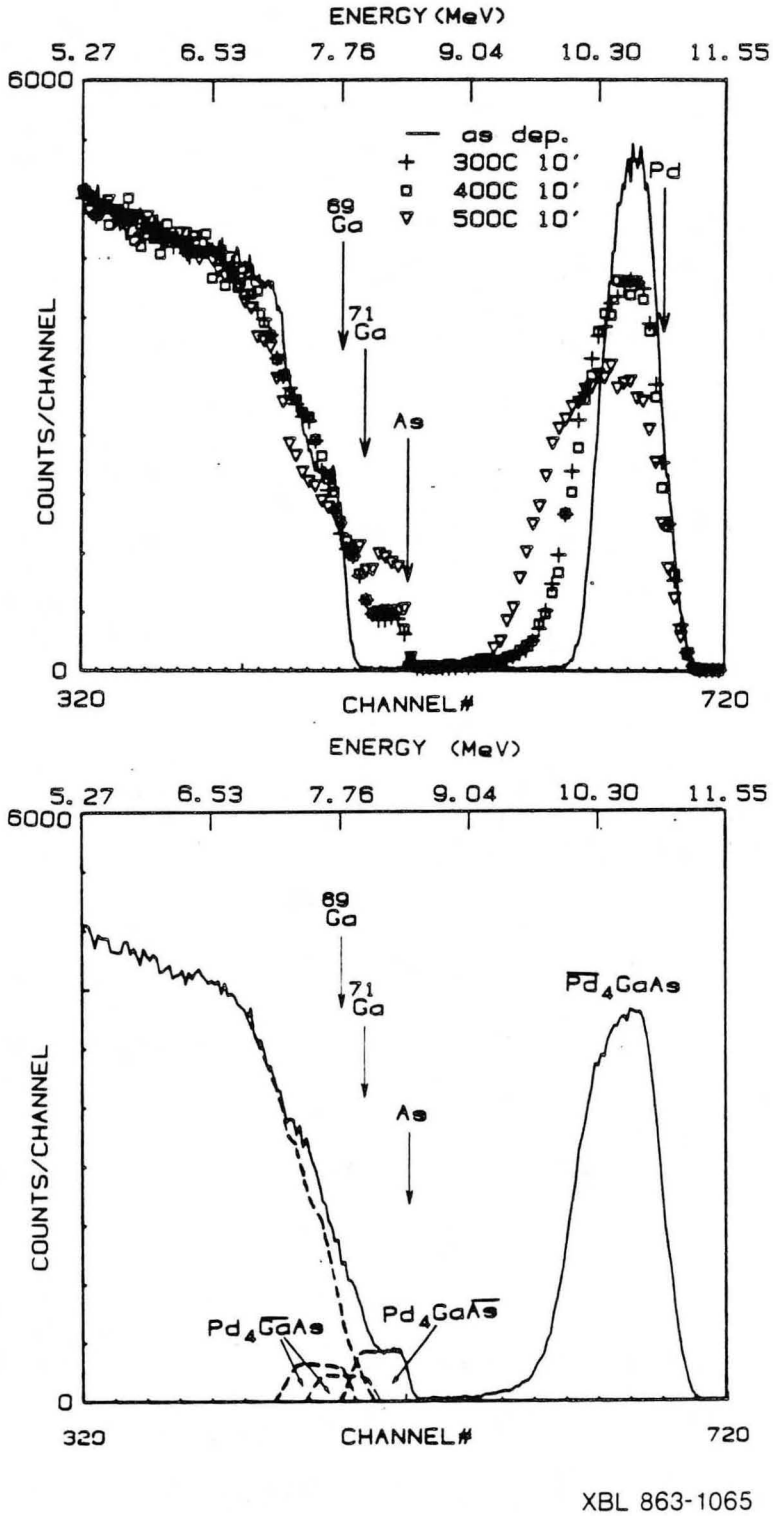

XBL 863-1065

Figure 3.20 (a) HIRBS spectra of 700 Å Pd/GaAs as deposited and after annealing at 350, 400 and 500 °C for 10 min. (b) Deconvolution of the HIRBS spectrum of Pd/GaAs sample annealed at 350 °C for 10 min.

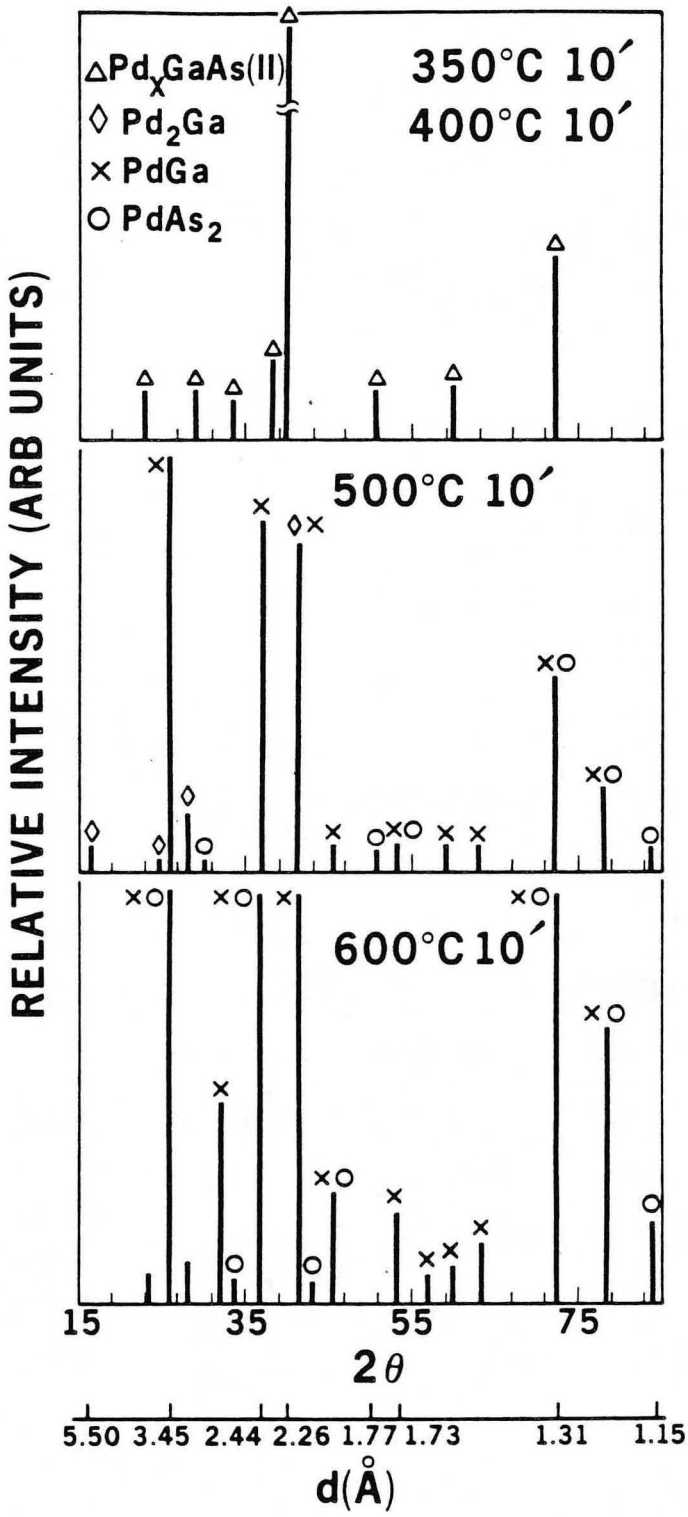

XBL 864-1423

Figure 3.21 XRD spectra of Pd/GaAs samples annealed at various temperatures.

is a ternary phase which had been identified previously by Kuan et al[21] and Sands et al[18,22-24] as $Pd_xGa_{(1+y)}As_{(1-y)}$ using TEM. This so called Phase II has a hexagonal structure (a_o=9.47 Å and c_o=3.74 Å) with a wide range of compositions (x ranging from 2 to 4 and y from 0 to 0.3) depending on the thickness of the Pd film and the annealing conditions [Reference 18] The reacted layer becomes less rich in Pd after annealing at 400°C for 10 min. A composition of [Pd]:[Ga]:[As]≈3.2:1:1 is measured. The XRD spectrum taken from this sample shows that this layer still has Phase II character.

Glancing angle RBS measurements on 130 Å Pd/GaAs couple show that ~30 Å of Pd have reacted with the substrate during metal deposition. However, the composition of this thin layer cannot be determined with RBS. Glancing angle RBS spectra for 130 Å Pd/GaAs samples annealed at 250°C and 350°C for 20 min are shown in Figure 3.22. [Pd]:[Ga]:[As] ratios for the reacted layers in the two samples are ≈4:1.1:0.9 and 3.3:1.1:0.9, respectively. Since the glancing angle RBS technique is relatively poor in spatial resolution, the compositions measured by this technique are averages over a large area and can be regarded as good estimates only for interfaces with uniform morphology.

Cross sectional TEM micrographs of 130 Å Pd/GaAs samples before and after annealing at 250°C and 350°C are shown in Figures 3.23 and 3.24. Approximately 90 Å of reacted phase is formed during TEM specimen preparation (maximum temperature ~80°C). This layer has hexagonal structure (a_o=6.73 Å and c_o=3.38 Å) and has been previously identified as a ternary phase, Phase I [References 22-24]. This Phase I layer is

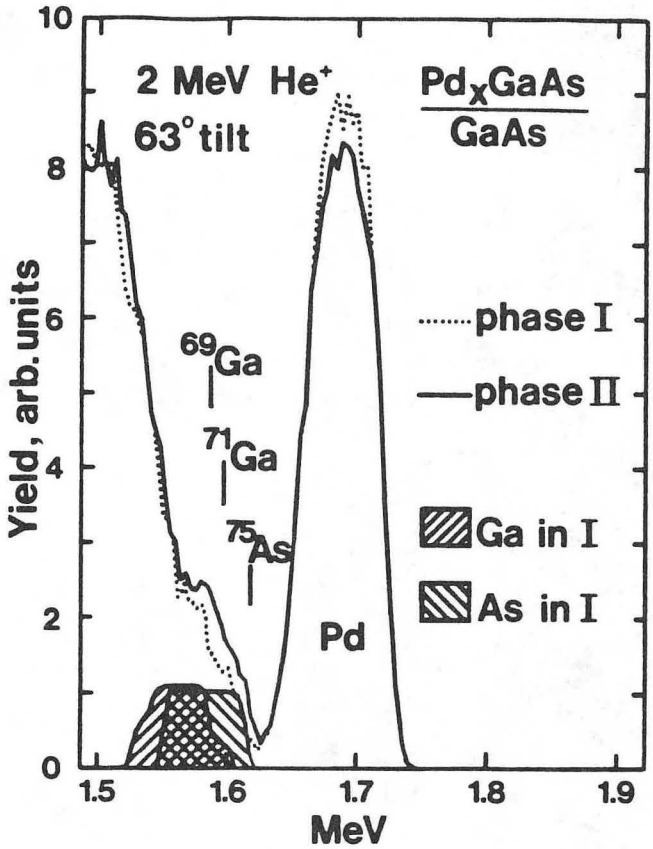

XBL 864-1505

Figure 3.22 Glancing angle RBS spectra of 150 Å Pd/GaAs after annealing. The dotted spectrum is from phase I formed during annealing at 250°C for 20 min. Deconvolution of this spectrum reveals signals from Ga and As in phase I. During additional anneal at 350°C for 20 min phase II is formed (solid spectrum).

nominally planar and monocrystalline. The region of light contrast between the Phase I layer and the unreacted Pd consists of dispersed patches of the original native oxide and voids resulting from the fact that Pd is the dominant moving species. At 250°C, the entire Pd film has reacted with the substrate resulting in a layer of ~170 Å of Phase I (Figure 3.24(b)). The [Pd]:[Ga]:[As] ratio in Phase I as determined by EDS analysis is ≈3.9:1.07:0.93 which is in perfect agreement with

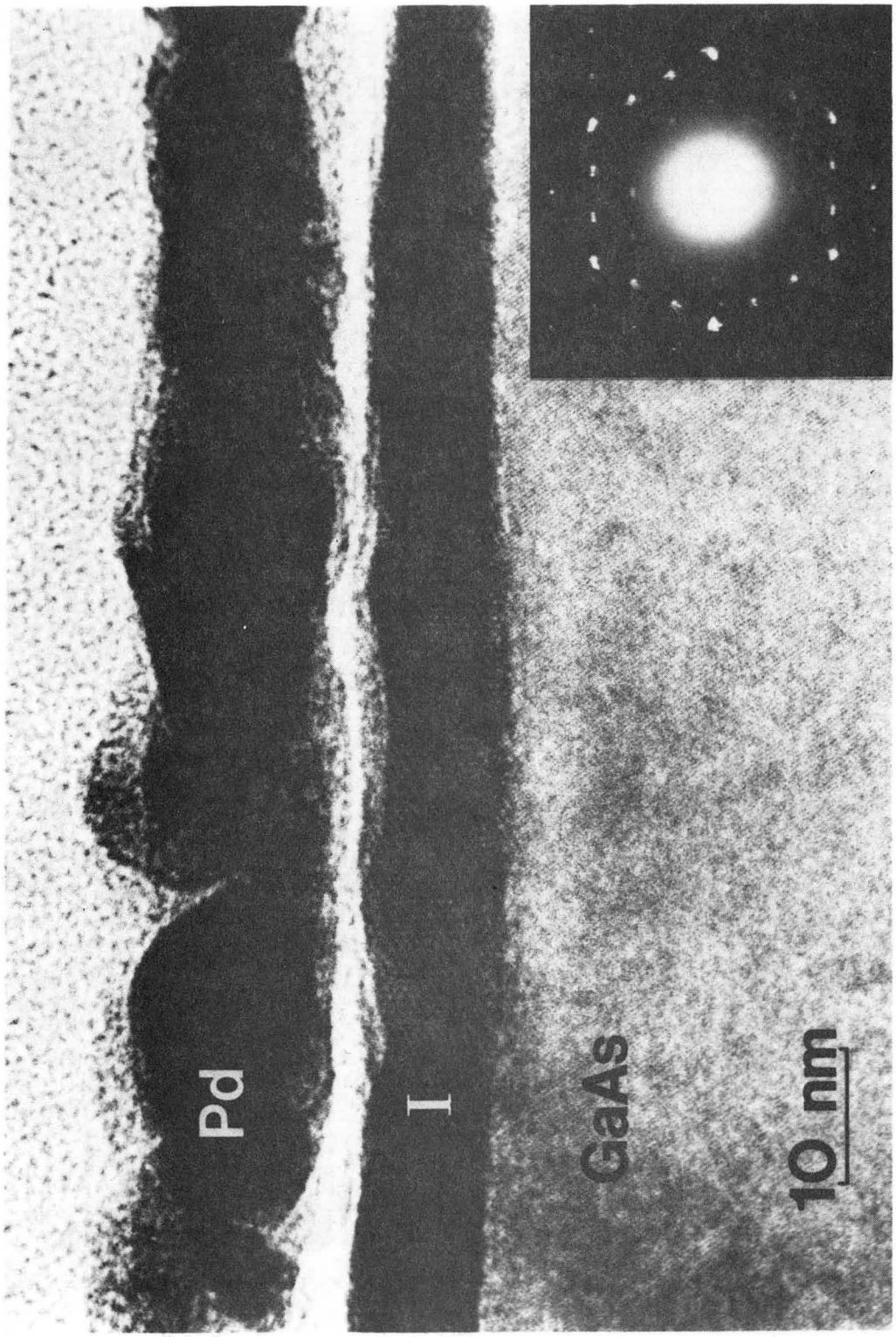

XBB 864-2701

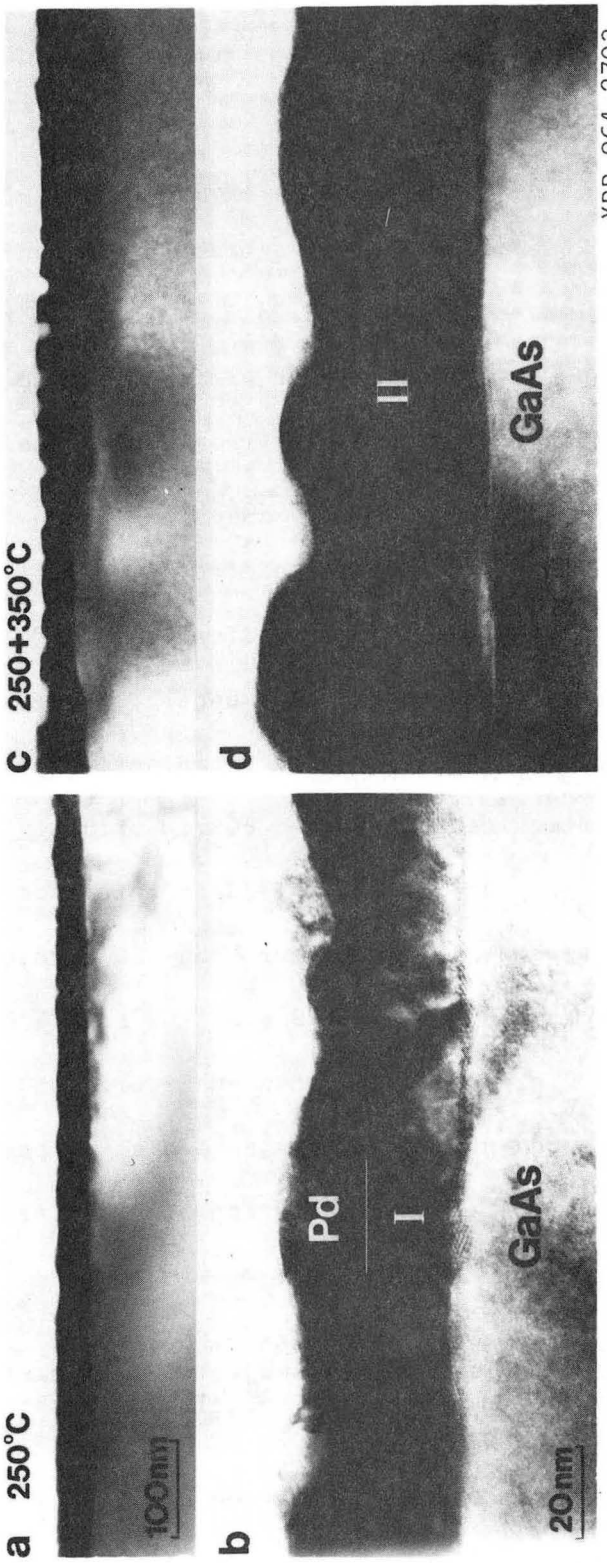

XBB 864-2703

the ratio given by RBS analysis. The composition of this phase I layer is, therefore, $Pd_{3.9}Ga_{1.1}As_{0.9}$.

Subsequent annealing treatment at 350°C converts the film to polycrystalline Phase II with only a trace of Phase I remaining. The cross sectional images in Figure 3.24 show that the Phase II/GaAs interface contains sharp cusps which are believed to result from the nucleation of Phase II in low angle grain boundaries in the Phase I film[24]. EDS analysis yields a composition of $Pd_{3.5}Ga_{1.2}As_{0.8}$ for Phase II. The availability of excess unreacted Pd which is very mobile[23] is important because it can laterally diffuse several microns at 350°C to the Phase II nucleation sites. Consequently, the resulting interface morphology is laterally nonuniform. The discrepancy in the composition of Phase II as determined by RBS and EDS is probably the result of the nonuniform morphology at the Phase II/GaAs interface.

Annealing at temperatures higher than 400°C results in further reactions of the system. The HIRBS spectrum of a 600 Å Pd/GaAs sample annealed at 500°C for 10 min is shown in Figure 3.20. It indicates that the three components of the system are still present in the reacted layer with surface concentration of [Pd]:[As]≈1.4:1. With XRD

Figure 3.23 (page 110) Cross-sectional TEM image of 150 Å Pd/GaAs before annealing. The sample was subjected to a maximum temperature of ~80°C during TEM specimen preparation. The diffraction pattern for this sample is also shown in the inset.

Figure 3.24 (page 111) Low magnification ((a) and (c)) and high magnification ((b) and (d)) TEM images of 220 Å Pd on GaAs after annealing at 250°C for 20 min ((a) and (b)) and after additional annealing at 350°C for 20 min ((c) and (d)). Images in (a) and (b) reveal relatively planar phase I

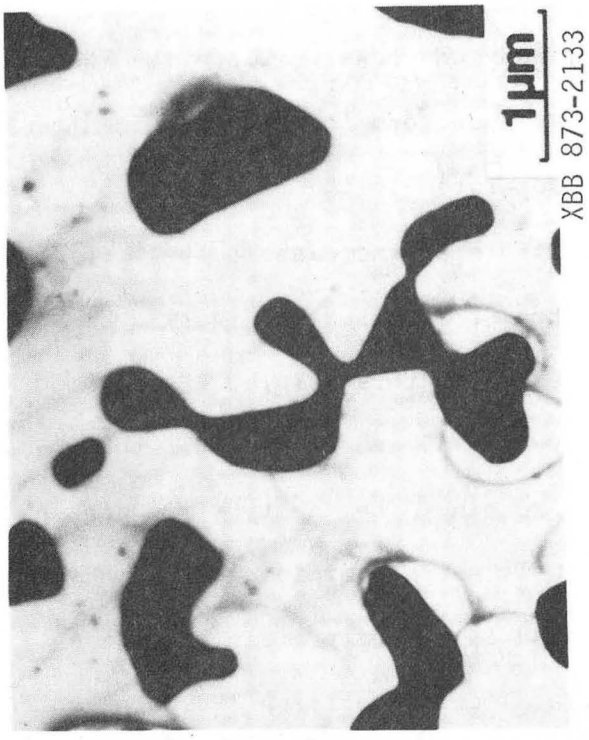
1μm
XBB 873-2133

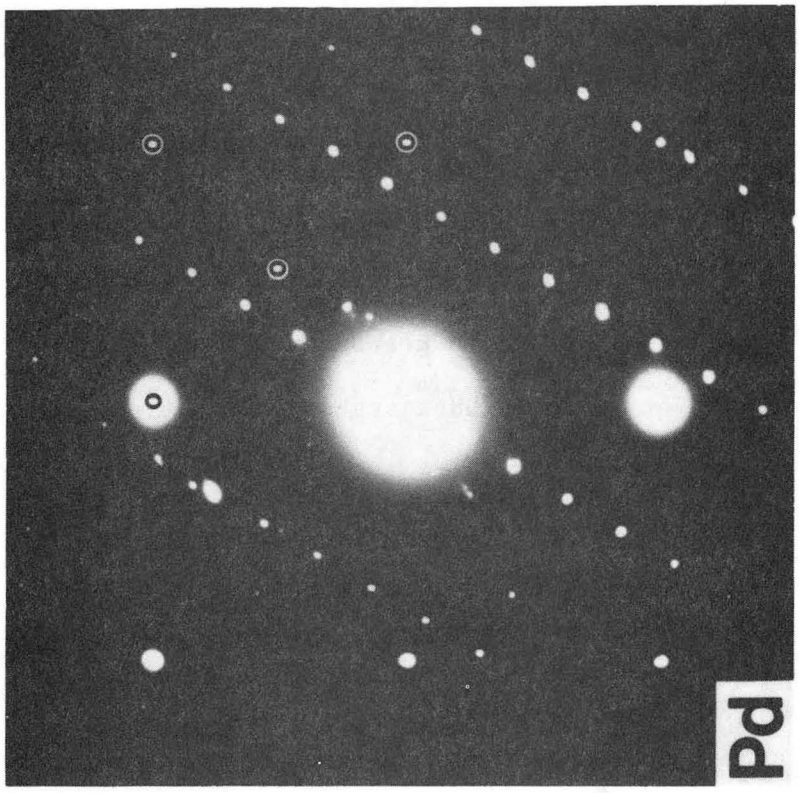
Pd

measurements on this sample (Figure 3.21) we can identify three binary phases, namely Pd_2Ga, PdGa and $PdAs_2$. Since the Pd signal in the HIRBS spectrum seems relatively uniform in height, it can be assumed that the phases are laterally separated in the reacted layer. Annealing at 600°C for 10 min results in an increase in the surface Pd concentration ([Pd]:[As]≈2.2:1). The XRD spectrum in Figure 3.21 shows that only PdGa and $PdAs_2$ are present in this sample.

Figure 3.25 shows the TED and BF image of the 130 Å Pd/GaAs sample annealed at 600°C for 20 min. The reacted film appears to be "balled up" with much of the GaAs surface exposed. TED and EDS analyses show that each reacted island is a single grain of hexagonal ternary phase (a_o=9.36 Å and c_o=3.70 Å) of composition ~Pd_5Ga_2As which is not very different from the Phase II detected at lower temperatures. This ternary phase has been reported by El-Boragy and Schubert[25] as a stable phase in the bulk Pd-Ga-As system at 600°C with a composition $Pd_{12}Ga_5As_2$. At thermodynamic equilibrium, the final phase predicted by El-Boragy and Schubert are PdGa and $PdAs_2$ which are the phases obtained for the 600 Å Pd/GaAs system in the present study. The fact that the final phase for the very thin Pd/GaAs system is the ternary Phase II can be understood if one consider the large surface-to-volume ratios in this system which alter the relative phase stabilities by excessive contributions of surface and interface energies.

Figure 3.25 (previous page) TED pattern and bright field image of 130 Å Pd/GaAs after annealing at 600°C for 20 min. The reacted film appears to be "balled up" with much of the GaAs surface exposed.

It should also be pointed out that very different results have also been reported on the Pd/GaAs system under different annealing conditions. Previous investigations of this system by Kuan et al[20,21] and Sands et al[22-24] showed that uncapped annealing in vacuum or forming gas ambients result in substantial losses of As at temperatures above 250°C. In fact Kuan et al[21] have observed that only the PdGa phase are present in 150 Å Pd/GaAs system annealed in vacuum at temperatures >350°C. Even with SiO_2 capping in the present study, a [Ga]:[As] ratio of 2:1 is observed for samples with thin palladium coverage (130 Å) annealed at 600°C. This is also important in the determination of the final stable phase(s) of the system.

3.6 Pt/GaAs

Figure 3.26 shows a series of HIRBS spectra of 1200 Å Pt/GaAs samples as deposited and annealed at 300, 400 and 500°C for 20 min. Reactions between Pt and GaAs at the interface are observed in the sample annealed at 300°C. Analysis of the spectrum using semi-empirical energy loss data for ^{16}O projectiles indicates that ~250 Å of Pt have reacted with the GaAs substrate. Significant Ga outdiffusion is also noted by HIRBS. The amount of Ga in the unreacted Pt film is estimated to be ~0.8 atomic percent. Kumar has reported this Ga outdiffusion phenomenon in the Pt/GaAs reactions and has related it to the difference in the electronegativity of Pt, Ga and As[26]. After annealing at 400°C for 20 min, the entire Pt film is fully reacted.

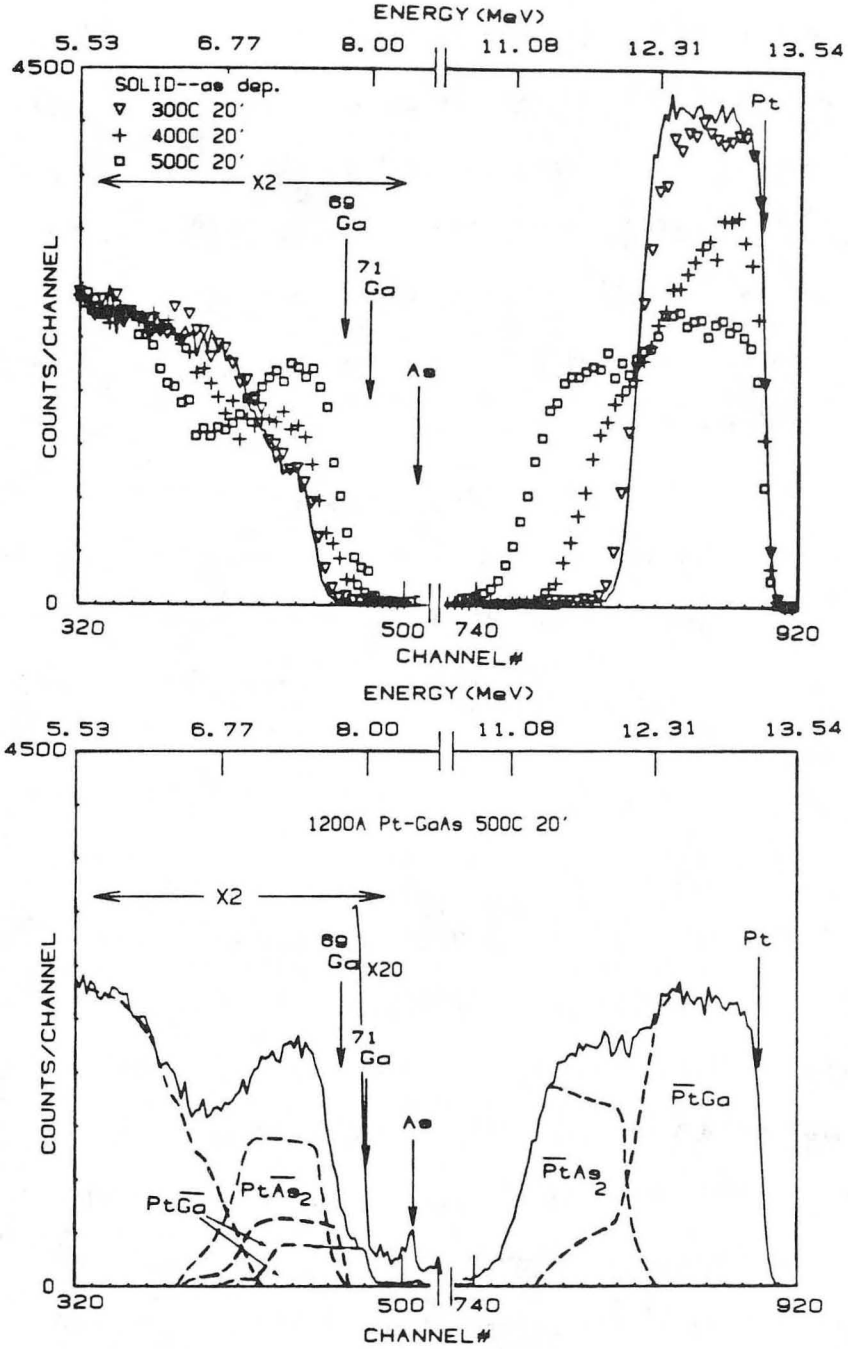

Figure 3.26 (a) HIRBS spectra of 1200 Å Pt/GaAs as deposited and annealed at different temperatures for 20 min. (b) HIRBS spectrum of the Pt/GaAs sample annealed at 500°C for 20 min. Deconvolution of this spectrum (dashed spectrum) shows the distribution of the different phases formed.

The high mass resolution of HIRBS unambiguously identifies that the top layer is composed of a compound of Pt and Ga with no detectable amount of As present, while the underlying layer at the GaAs interface is primarily a Pt-As compound. Annealing at 500°C for 20 min results in the reduction in Pt concentration in the top layer.

XRD measurements on the annealed Pt/GaAs samples identify three binary phases: cubic Pt_3Ga (Li_2 type, a_o=3.892 Å), cubic PtGa (FeSi type, ao=4.91 Å) and $PtAs_2$ (FeS_2 type, a_o=5.9665 Å). All three phases are also found in the sample annealed at 400°C for 20 min. For samples annealed at temperatures higher than 500°C (up to 800°C), only PtGa and $PtAs_2$ are found. Therefore, we conclude that the final stable phases for the Pt/GaAs system are the binary PtGa and $PtAs_2$ phases. Deconvolution of the HIRBS spectrum of the sample annealed at 500°C for 20 min (Figure 3.26(b)) clearly shows that the layer sequence of PtGa/$PtAs_2$/GaAs is consistent with the XRD results. It is also noticeable that ~15% of PtGa is present in the $PtAs_2$ layer while As with concentration of ~$10^{19}cm^{-3}$ is found at the surface of this sample. In the HIRBS spectrum of the sample annealed at 400°C for 20 min, the layer sequence of Pt_3Ga/PtGa/$PtAs_2$/GaAs is also detected. No new phase appears after annealing at temperatures higher than 500°C. For samples annealed at 800°C for 20 min, HIRBS measurement shows that a significant amount of Pt (~$10^{20}cm^{-3}$) diffuses into the GaAs substrate to a depth ≳1700 Å. This interdiffusion of Pt and As (Ga) at the interface may be the source for the electrical degradation of the Pt/n-GaAs Schottky diode after high temperature annealing (>500°C) observed in earlier investigations of this system[27].

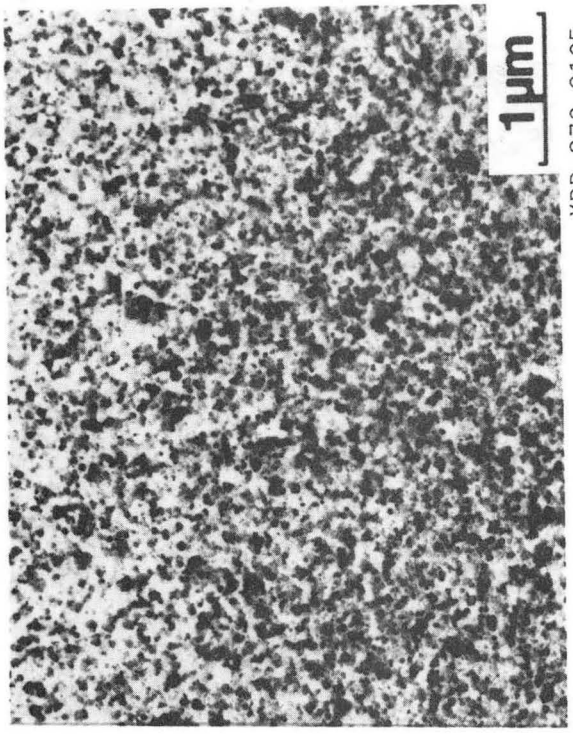

XBB 873-2135

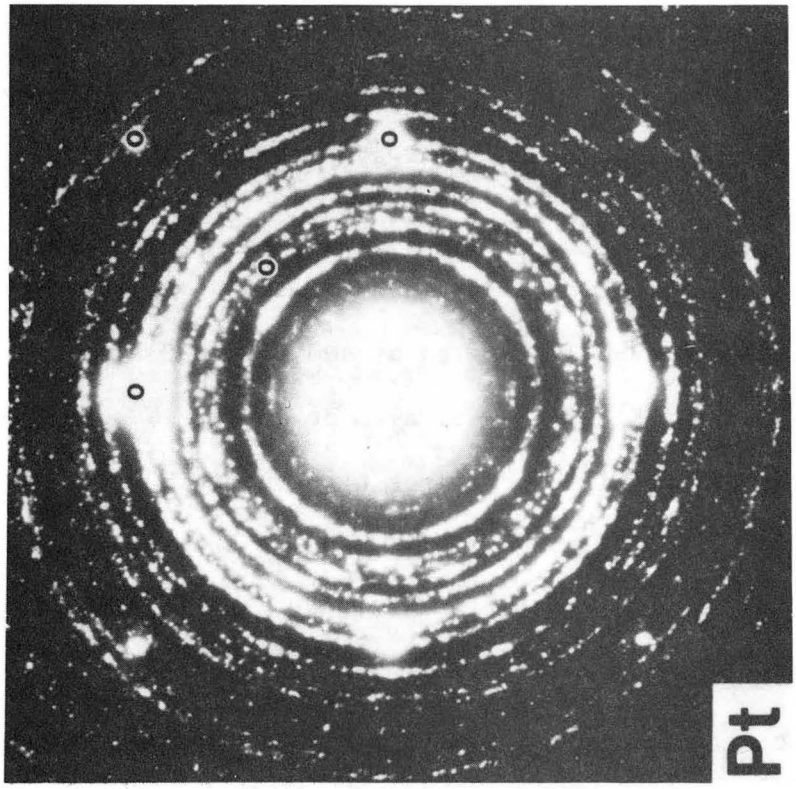

TEM investigation of very thin film (120 Å) of Pt on GaAs shows that the stable final phases are the binary PtGa and $PtAs_2$ phases. This is in perfect agreement with the HIRBS and XRD results on the thicker films. Figure 3.27 shows the TED pattern together with the BF image of the 120 Å Pt/GaAs sample annealed at 600°C for 20 min. Grain size of ~500 Å is detected in the reacted layer. Only very weak crystallographic texture for $PtAs_2$ on GaAs is observed. Glancing angle RBS analysis of this sample shows that there is a certain degree of vertical phase stratification in the reacted layer. This is consistent with the observation that the grain size of the reacted phases is comparable with the layer thickness after reactions.

The HIRBS, XRD and TEM results in the present study on the Pt/GaAs system are consistent with the results reported in the literature [References.18,26,28] The solid phase reactions of this system are expected to proceed as follows:

1. Electropositive Ga diffuses into the relatively electronegative Pt layer and dissolves in this layer.

2. In-diffusing Pt atoms react with the As atoms released by Ga outdiffusion forming stable $PtAs_2$ layer at the GaAs interface.

3. More interdiffusions of Pt and Ga results in the formation of the Pt_3Ga phase at the $PtAs_2$/Pt interface and the thickening of the $PtAs_2$ layer.

Figure 3.27 (previous page) TED pattern and bright field image of 120 Å Pt/GaAs annealed at 600°C for 20 min. Grain size of ~500 Å is observed in the reacted layer.

4. Since Pt_3Ga is not the stable final Pt-Ga phase, as more Ga diffuses out, Pt_3Ga is transformed into the stable PtGa phase. Diffusion controlled kinetics is measured by HIRBS for the Pt/GaAs reactions with an activation energy of ~1.6 eV. This result is in good agreement with that reported by Coleman et al[29].

3.7 Summary and Conclusions on Near Noble Metal/GaAs Reactions

3.7.1 Phase composition and structure

1) For metal films with a thickness >400 Å, the final stable phases are always found to be binary M_xGa and M_yAs phases with $x \geq 1$ and $y \leq 1$.
2) The ratios of the amount of reacted metal to GaAs, [M]/[GaAs] in the final reacted layers vary from 1.1 to 2. For Co and Ni, this ratio is 2; for Ir which reacts with GaAs at relatively high temperatures ($\geq$500°C), this ratio is 1.1; and for Pd, Rh and Pt [M]/[GaAs]=1.5.
3) Except for the relatively non-reactive Ir/GaAs interface, the final stable M-Ga phases are the cubic MGa phases (M=Co, Rh, Ni, Pd and Pt). Cubic IrGa is also detected but it is an intermediate phase which transforms into the more stable Ga rich tetragonal Ir_3Ga_5 phase at high temperatures (~700°C). The final stable M-As phases are MAs for the relatively more electropositive Co, Ni (X=1.8) and MAs_2 for the very electronegative Rh, Ir, Pd and Pt.

4) For the very reactive metals (Co, Ni and Pd), initial reactions at low temperatures ($\lesssim$300°C) result in the formation of ternary phases M_xGaAs with x ranging from 2 to 4. For the less reactive metals (Rh, Ir and Pt), the intermediate phases are binary phases (RhAs, IrGa and Pt_3Ga).

5) Pd/GaAs forms two ternary phases, Phase I and II at ~200 and 300°C, respectively. For very thin Pd films (~120 Å), the system is far from equilibrium and the As deficient Phase II can be the stable final phase.

3.7.2 Phase distribution and morphology

1) Vertical phase stratification is always observed for the less reactive M/GaAs systems (M=Rh, Ir and Pt) which react at temperatures $\gtrsim$300°C and a film thickness $\gtrsim$400 Å. For the more reactive Co, Ni and Pd which form ternary phases with GaAs, the final stable binary phases are only laterally separated so that both the M-Ga and M-As phases are in intimate contact with the substrate.

2) The phase stratification phenomenon is believed to be related to the grain size of the phases in the reacted layer. When the grain size becomes comparable to the reacted film thickness, due to the large contributions of interface energies phase stratification becomes energetically less favorable. The grain size has been found to be affected by the metal-metal (M-M) bond strength in the metal[30]: the stronger the M-M

bond, the finer will be the grain of the reacted phases. This M-M bond strength is manifested in the heat of vaporization of the metal. In other words, under the same annealing conditions, the grain size decreases with increasing heat of vaporization of the metal. The relationship of grain size and heat of vaporization is shown in Table VI.

3) For metals with strong M-M bonds (Rh, Pt and Ir), the grain sizes of the reacted phases in the M/GaAs systems are small ($\lesssim$500 Å). Therefore, abrupt uniform interfaces between stratified phases are formed with very little interpenetration of phases.

Table VI Correlation between heats of vaporization and grain size in reacted films after annealing 120 Å M/GaAs for 20 min at 600°C with SiO_2 cap.

M	Heats of Vaporization[a] of M (298K)(kcal/mol^{-1})	nominal grain size (Å)
Pd	90.0±0.5	10000
Ni	102.8±0.5	5000
Co	102.4±1	1000
Pt	135.2±0.3	500
Rh	133±1	500
Ir	160±1	150

[a] Compiled by J. A. Kerr and A. F. Trotman-Dickenson in *Handbook of Chemistry and Physics* (CRS, Cleveland, 1976).

4) For systems with stratified phases after reactions, the M-As phase is always found at the GaAs interface. Since As is relatively more electronegative (X=2.0) than Ga (X=1.6), Ga atoms, released by the thermal dissociation of interface GaAs, are attracted by the electronegative metal overlayer and thus has a stronger tendency to diffuse out to the overlayer. Therefore, the As atoms tend to be relatively immobile and stay at the GaAs interface forming a M-As phase.

3.7.3 Reaction kinetics

1) Parabolic reaction rates are found in all the near noble metal/GaAs interactions. Therefore, we conclude that diffusion controlled process dominates in the reactions of thin film near noble metal/GaAs interfaces. For the Pd/GaAs and Ni/GaAs interfaces the reaction kinetics cannot be measured with good accuracy due to the extremely reactive nature of these interfaces at low temperatures.

2) In the second stage reaction of Ir/GaAs at high temperature (~700°C) when atomic diffusion is so rapid that diffusion is no longer the rate controlling process, nucleation controlled kinetics dominates.

3) Except for the Ir/GaAs contact, activation energies measured in the solid phase reactions of thin film near noble metal/ GaAs systems are around 1.60-1.70 eV. These values are comparable to those obtained for the formations of near noble

metal silicides. For the relatively more stable Ir/GaAs system, the activation energy is ≈3.15 eV.

4) Only one activation energy is found for near noble metal/GaAs systems which undergo 2-stage reactions such as the Rh/GaAs and the Pt/GaAs couples. This implies that the activation free energies of reactions ΔG in the first stage reactions are larger than those for the second stage reactions. Therefore, the overall kinetics is dominated by the first stage reactions and the activation energy of which is measured experimentally. A schematic diagram showing the energy change of this type of 2-stage reactions is shown in Figure 3.28.

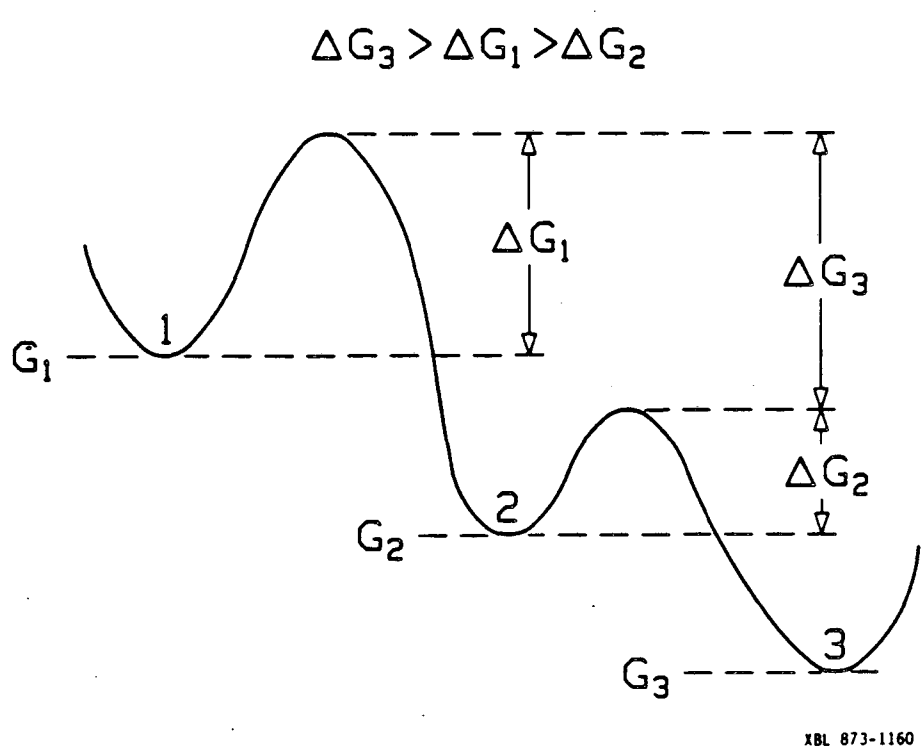

Figure 3.28 A schematic diagram showing the free energy change of the 2-stage reactions of near noble metal/GaAs contacts.

REFERENCES TO CHAPTER 3

1. R. S. Williams, J. R. Lince, T. C. Tsai and J. H. Pugh, Mat. Res. Soc. Symp. Proc. **54**, 335 (1986).

2. A. J. Yu, G. J. Galvin, C. J. Palmstrom and J. W. Mayer, Appl. Phys. Lett. **47**, 934 (1985).

3. A. J. Yu, G. J. Galvin, J. W. Mayer, C. J. Palmstrom, T. Sands and C. C. Chang, presented at the 1986 Spring Meeting of the Mat. Res. Soc., April 17, 1986, Palo Alto, Ca.

4. JCPDS powder diffraction file #19-490.

5. F. M. d'Heurle and P. Gas, J. Mat. Res. **1**, 205 (1986).

6. C. S. Petersson, J. E. Baglin, W. Hammer, F. M. d'Heurle, T. S. Kuan, I. Odhmari, J. deSousa Pires and P. A. Tove, J. Appl. Phys. **50**, 3357 (1979).

7. C. S. Petersson, R. Anderson, J. E. Baglin, J. Dempsey, W. Hammer, F. M. d'Heurle and S. J. LaPlaca, J. Appl. Phys. **51**, 373 (1980).

8. J. E. Baglin, J. M. d'Heurle and C. S. Petersson, Appl. Phys. Lett. **36**, 594 (1980).

9. R. D. Thompson, B. Y. Tsaur and K. N. Tu, Appl. Phys. Lett. **38**, 535 (1981).

10. K. K. Shih and J. M. Blum, Solid State Electron. **15**, 1177 (1972).

11. N. Braslau, J. B. Gunn and J. L. Staples, Solid State Electron. **10**, 38 (1967).

12. G. Y. Robinson, IEDM Tech. Dig. 253, Intern. Electron. Device Meeting, Washington D. C., Dec. 1973.

13. G. Y. Robinson, J. Vac. Sci. Technol. **13**, 884 (1976).

14. M. Ogawa, J. Appl. Phys. **51**, 406 (1980).

15. T. S. Kuan, P. E. Batson, T. N. Jackson, H. Rupprecht and E. L. Wilkie, J. Appl. Phys. **54**, 6952 (1985).

16. A. Lahav, M. Eizenberg and Y. Komen, Mat. Res. Soc. Symp. Proc. **37**, 641 (1985).

17. T. Sands, V. G. Keramidas, J. Washburn and R. Gronsky, Appl. Phys. Lett. **48**, 402 (1986).

18. T. Sands, V. G. Keramidas, A. J. Yu, K. M. Yu, R. Gronsky and J. Washburn, J. Mat. Res., in press (1987).

19. E. D. Marshall, W. X. Chen, C. S. Wu, S. S. Lau and T. F. Kuech, Appl. Phys. Lett. **47**, 298 (1985).

20. T. S. Kuan, Mat. Res. Soc. Symp. Proc. **31**, 143 (1984).

21. T. S. Kuan, J. L. Freeouf, P. E. Batson and E. L. Wilkie, J. Appl. Phys. **58**, 1519 (1985).

22. T. Sands, V. G. Keramidas, R. Gronsky and J. Washburn, Mat. Lett. **3**, 409 (1985).

23. T. Sands, V. G. Keramidas, R. Gronsky and J. Washburn, Thin Solid Films **136**, 105 (1986).

24. T. Sands, V. G. Keramidas, A. J. Yu, K. M. Yu, R. Gronsky and J. Washburn, Mat. Res. Soc. Symp. Proc. **54**, 367 (1986).

25. M. El-Boragy and K. Schubert, Z. Metallkde. **72**, 279 (1981)

26. V. Kumar, J. Phys. Chem. Solids **36**, 535 (1975).

27. A. K. Sinha, T. E. Smith, M. H. Read and J. M. Poate, Solid State Electron. **19**, 489 (1976).

28. C. Fontaine, T. Okumura and K. N. Tu, J. Appl. Phys. **54**, 1404 (1983).

29. D. J. Coleman, Jr., W. R. Wisseman and D. W. Shaw, Appl. Phys. Lett. **24**, 355 (1974).

30. T. Sands, V. G. Keramidas, K. M. Yu, J. Washburn and K. Krishnan, J. Mat. Res., in press (1987).

4. RESULTS AND DISCUSSIONS II: SOLID PHASE REACTIONS BETWEEN (100) GaAs AND REFRACTORY METAL FILMS

Recently, the fabrication of a high-speed metal GaAs MESFET using the self-aligned gate (SAG) technique has been proposed[1]. In the SAG process, the gate is used as an implantation mask for the formation of the source and drain regions. Implantation is followed by a high temperature annealing step (>850°C). This requires thermally stable (above 850°C) and process reproducible GaAs Schottky contacts.

The thermal stability of refractory metals[2] as well as the alloys[3], silicides[4-7] and nitrides[8,9] of refractory metals have been explored as gate materials for SAG GaAs MESFET. Despite all these studies focussing on the exploration of suitable gate materials for SAG GaAs MESFETs, very little is known about the interactions at the refractory metal/GaAs interfaces. In order to select better gate materials for GaAs SAG-MESFET in the future, the interfacial metallurgy of refractory metal/GaAs contact systems must be well understood. In the present study, the solid phase reactions between (100) GaAs and thin films of refractory metals including titanium, zirconium, vanadium, niobium, chromium, molybdenum and tungsten are investigated. Issues such as reaction kinetics and the distribution and composition of the reacted phases will be discussed. A summary of these results is given in Table VII.

Table VII Summary of the solid phase reactions between thin film refractory metals and (100) GaAs substrate.

Metal	Reaction Temp. (°C)	Phases formed	Phase Distribution	Reaction Rate[a)]	Activation Energy (eV)
Ti	>400	TiGa (Tetragonal) TiAs (Hexagonal)	TiGa/TiAs/GaAs	D	1.53 ±0.15
Zr	450	Zr_xGa } $x+y \approx 3$ Zr_yAs	$Zr_xGa/Zr_yAs/GaAs$	D	1.25 ±0.10
	700	Zr_5Ga_3 (Hexagonal) Zr_xAs; $x \approx 0.4$	$Zr_5Ga_3/Zr_xAs/GaAs$		
V	450	V_3Ga (Cubic) V_xAs; $x \approx 2$	$V_3Ga/V_xAs/GaAs$	D	2.10 ±0.10
	700	V_6Ga_5 (Hexagonal) V_4As_3 (Monoclinic)	$V_6Ga_5/V_4As_3/GaAs$		
Nb	550	Nb_xGa } $x<y$; Nb_yAs $x+y \approx 1.5$	$Nb_xGa/Nb_yAs/GaAs$ (non-abrupt interface)	D	2.60 ±0.30
Cr	≥450	Cr_3Ga (Cubic) CrAs (Orthorhombic)	$Cr_3Ga/CrAs/GaAs$	-	-
	550	CrGa (Rhombohedral) CrAs (Orthorhombic)	CrGa/CrAs/GaAs	-	-
Mo	≥650	Mo_3Ga (Cubic) Mo_5As_4 (Tetragonal)	$Mo_3Ga/Mo_5Ga_4/GaAs$	D, R	-
	≥850	Mo_xGaAs_y $MoAs_2$ (Monoclinic)	(?)	N	-
W	≥750	W_2As_3 (Monoclinic)	"ball up" forming islands of single grain W_2As_3.	-	-

a) D≡diffusion controlled growth; R≡interface reaction comntrolled growth and N≡nucleation controlled growth.

4.1 Ti/GaAs

Reactions between a Ti thin film and the GaAs substrate are observed at annealing temperatures above 400°C. Results of the HIRBS measurements on 1000 Å Ti/GaAs samples as deposited and annealed at 450 and 500°C for 20 min are illustrated in Figure 4.1. After annealing at 500°C for 20 min the Ti film is completely consumed by reacting with the GaAs substrate. Deconvolution of the HIRBS spectrum from the sample annealed at 500°C (Figure 4.1(b)) indicates a two layer phase sequence with the top layer composed primarily of Ti and Ga and the interface layer consisting of Ti and As. From the energy loss characteristics of the ^{16}O projectiles in Ti and GaAs, the atomic ratio of the reacted [Ti]:[GaAs] is estimated to be 2:1. Ratios of the backscattering yields from the individual element in the HIRBS spectrum gives [Ti]:[Ga]≈1:1 for the top layer and [Ti]:[As]≈1:1 for the layer at the interface. The presence of a large amount of As signals in the top layer in the spectrum indicates that the interface between the TiGa and TiAs phases is non-abrupt. XRD spectra from samples of Ti/GaAs annealed at 450 and 500°C for 20 min show that the products of thermally activated Ti/GaAs reactions in this temperature range are hexagonal TiAs (a_o=3.64 Å and c_o=12.06 Å) with 8 atoms per unit cell and tetragonal TiGa (a_o=c_o=3.97 Å). A summary of the XRD data together with the X-ray powder diffraction data from TiGa and TiAs standards are given in Table VIII.

HIRBS spectra from samples annealed at 500°C for longer times show that the Ga and As signals in the two layers start to intermix but

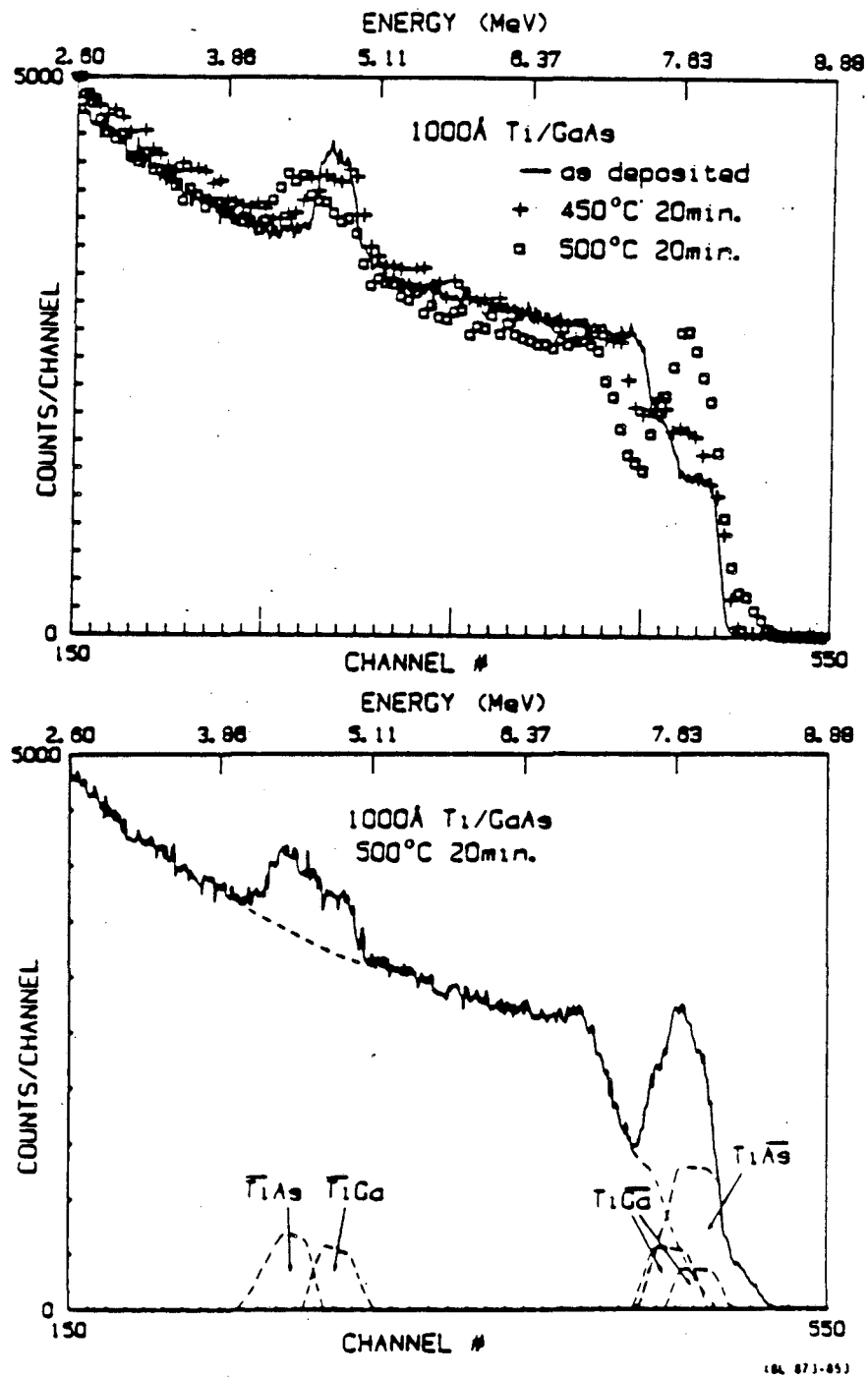

Figure 4.1 (a) HIRBS spectra of 1000 Å Ti/GaAs samples as deposited and annealed at 450 and 500°C for 20 min. (b) Deconvolution of the spectrum of the sample annealed at 500°C for 20 min showing a layer sequence of Ti-Ga/Ti-As /GaAs.

Table VIII Comparison of the XRD data[a)] for Ti/GaAs samples under different annealing conditions and the powder diffraction data of TiGa and TiAs from the JCPDS diffraction file.

XRD data		Powder diffraction data		
450 °C, 20 min.	500 °C, 20 min.	Ti[b)]	TiGa[c)]	TiAs[b)]
2.78 (w)	2.786 (m)		2.807(110)	2.79 (102)
	2.46 (w)			2.479(103)
2.28 (s)	2.2815(s)		2.292(111)	
	2.174 (w)			2.183(104)
	1.8154(m)			1.823(110)
	1.69 (w)			1.693(106)
	1.33 (w)		1.323(221)	1.320(205)
1.243(w)		1.247(112)		
	1.14 (w)		1.14 (222)	

a) All plane spacings are in Å. Powder diffraction data are indexed with hkl in paratheses. (w), (m) and (s) denote weak, medium and strong intensity diffraction peaks, respectively.
b) Powder diffraction data for Ti and TiAs are taken from JCPDS card # 5-0682 and 7-134, respectively.
c) Powder diffraction data for TiGa are calculated from the crystallographic parameters obtained from the equilibrium phase diagram of Ti-Ga.

without further consumption of the GaAs substrate. Moreover, no new phase is detectable in these samples by XRD. This can be interpreted as the effect of more interpenetration between the two phases which make their interface very rough. The interpenetration of phases at the interface can be explained by grain growth of the phases during extended annealing time. Further annealing at temperatures higher than 500°C (up to 800°C) does not result in new features in the HIRBS and XRD spectra. Therefore, TiGa and TiAs are the only and final products for the solid phase reactions between thin film Ti and GaAs with the layer sequence of TiGa/TiAs/GaAs when a short annealing time is used ($\leq$20 min).

Using the AES and XRD techniques, Wada et al[10] reported a layer sequence of Ti-Ga/Ti-As/GaAs as a result of Ti/GaAs reactions at elevated temperatures. This is consistent with the HIRBS results in the present study. They observed the presence of TiAs and Ti_2Ga_3 phases in samples of Ti/GaAs annealed at 480°C. At higher annealing temperatures, they also found Ti_5Ga_4 and Ti_5As_3 phases in addition to the other two phases. Since no capping had been applied to the Ti/GaAs samples during annealing in the study by Wada et al, it is likely that excess vaporization of As at elevated temperatures resulted in the formation of As deficient phase. However, with a limited amount of Ti (thin film) and a quasi-unlimited amount of GaAs, it is doubtful that the reaction will be driven from the more Ga (As) rich Ti_2Ga_3 (TiAs) phase(s) to the more Ti rich Ti_5Ga_4 (Ti_5As_3) phase(s).

The reaction kinetics for the Ti/GaAs system has also been explored with HIRBS. The reaction rate of the Ti/GaAs interface is found to be dependent on the square root of annealing time t, i. e. dominated by a diffusion process. The activation energy for the reactions is estimated from reaction rate curves and equals 1.53±0.15 eV. These kinetics are in good agreement with those measured by Wada et al who reported a slightly higher ΔE of ≈1.70 eV. However, it is worth pointing out that the AES technique employed by Wada et al for depth profiling is not quantitative and therefore depth information obtained by this method without appropriate standard cannot be con-sidered accurate.

4.2 Zr/GaAs

Interdiffusion at the Zr/GaAs interface is observed by HIRBS at temperatures around 450°C. Results of the HIRBS measurements on 1100 Å Zr/GaAs samples as deposited and annealed at different temperatures are presented in Figure 4.2. Deconvolution of these spectra are difficult due to the good mass resolution of HIRBS which partially resolves the different isotopes of Zr. In other words, the effects of the multiple isotopes of Zr on the HIRBS spectra are similar to those of an alloy film composed of many elements with similar masses. The spectra in Figure 4.2 show that the reactions at the Zr/GaAs interface proceed very slowly. The reactions are completed only after annealing at 700°C for 60 min. The atomic ratio of Zr and GaAs in this final stage of

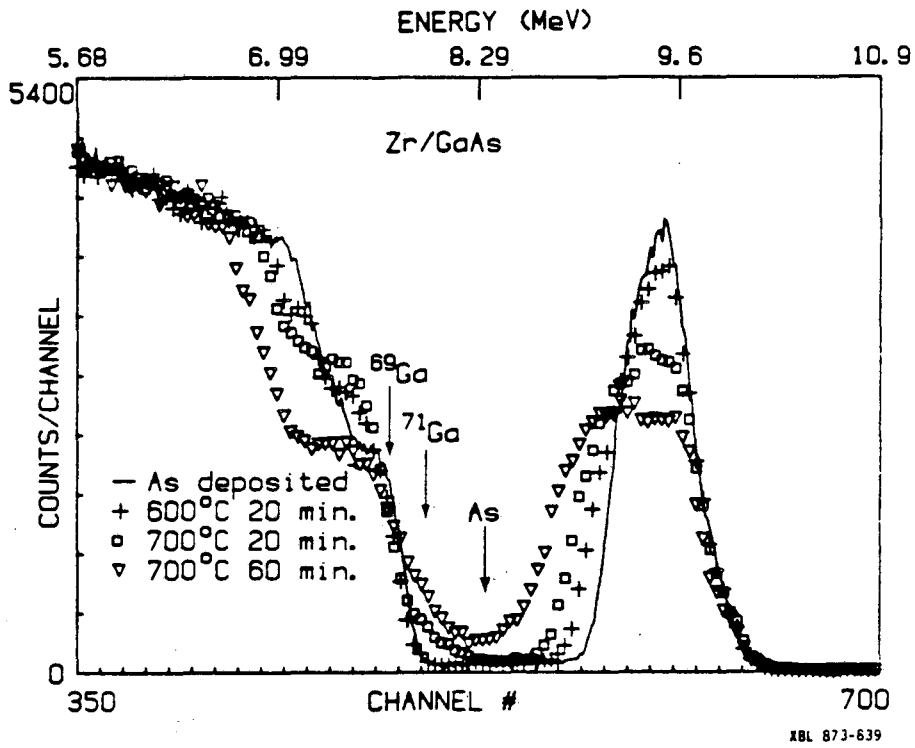

Figure 4.2 HIRBS spectra of 1100 Å Zr/GaAs samples as deposited and annealed at different temperatures.

reaction is measured by HIRBS and is ≈2:1. An intermediate stage in the Zr/GaAs reactions with [Zr]:[GaAs]≈3:1 is also observed at annealing temperatures around 650-700 °C. The relatively long annealing time required for reactions in this system promotes significant grain growth in the reacted layer. This is manifested by the absence of phase stratification as noticed in the HIRBS spectra.

Results of XRD measurements on the same set of samples are tabulated in Table IX. X-ray powder diffraction data on a Zr_5Ga_3 standard are also shown in the table. The Zr_5Ga_3 standard data match well with some of the diffraction peaks in the XRD spectrum from the

Table IX Comparison of XRD data[a)] for annealed Zr/GaAs samples with powder diffraction data for Zr_5Ga_3 from the JCPDS file.

Zr/GaAs XRD data		Powder diffraction data
650 °C, 30 min.	700 °C, 60 min.	Zr_5Ga_3[b)]
	3.1596 (m)	3.456 (200)
	2.975 (m)	
2.923 (w)		
	2.8237 (w)	
2.75 (m)		
2.68 (w)		
2.609 (s)	2.60 (m)	2.603 (210,102)
	2.30 (w)	2.299 (300,112)
	1.996 (m)	1.998 (220)
1.899 (w)	1.8997 (m)	1.918 (310,212) 1.881 (221)
1.561 (w)	1.54 (w)	1.536 (213,321)
1.30 (m)		
	1.2276 (w)	

a) All plane spacings are in Å. Powder diffraction data are indexed with hkl in paratheses. (w), (m) and (s) denote weak, medium and strong intensity diffraction peaks, respectively.
b) Powder diffraction data for Zr_5Ga_3 is taken from card # 12-82 of the JCPDS powder diffraction data file.

sample annealed at 700°C for 60 min. Therefore, it can be concluded that one of the reacted final phase is Zr_5Ga_3. Because of the lack of x-ray powder diffraction and equilibrium thermodynamic data for Zr-As phases, identification of Zr-As phase(s) by direct matching of the XRD results is not possible.

Figure 4.3 shows plots of the square of GaAs consumed (in cm) during reactions as measured by HIRBS versus annealing time for different annealing temperatures. The linear relationship shown in these plots indicate that all reactions are diffusion controlled. The activation energy of the reactions is estimated from the slope of the Arrhenius plot shown in Figure 4.4 and is 1.25±0.15 eV. The value of this energy is low compared to those obtained for other metal/GaAs systems.

Since minimization of the free energy G is the real driving force for a given reaction, the free energy change ΔG is of primary interest. From basic thermodynamics, ΔG can be expressed as:

$$\Delta G = \Delta E - T\Delta S$$

where T is the temperature and ΔS is the activation entropy of the reaction. Therefore, from the kinetic theory, the reaction rate can be written as:

$$\frac{dx}{dt} = K\exp\left(\frac{-\Delta G}{kT}\right) = K\exp\left(\frac{\Delta S}{k}\right)\exp\left(\frac{-\Delta E}{kT}\right), \qquad (4.1)$$

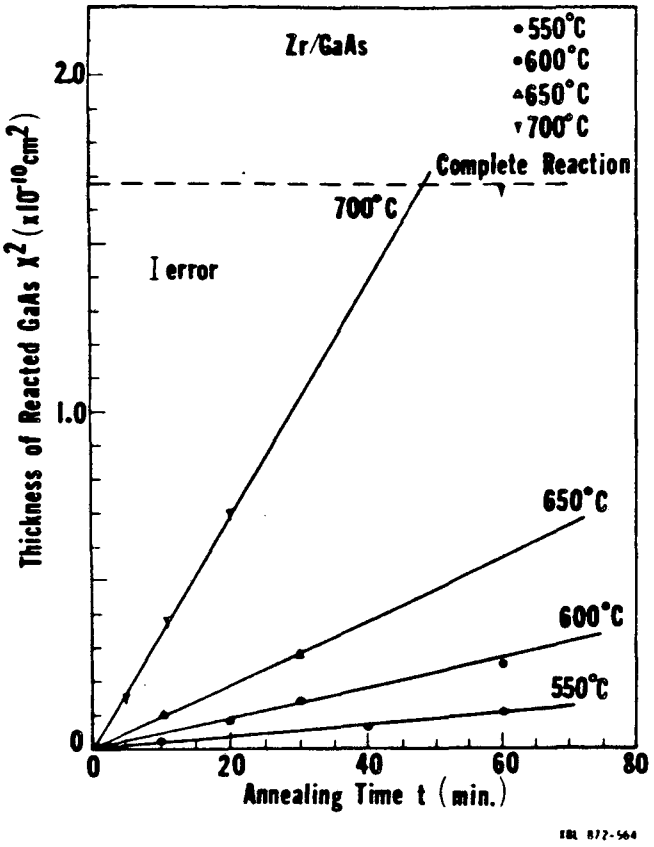

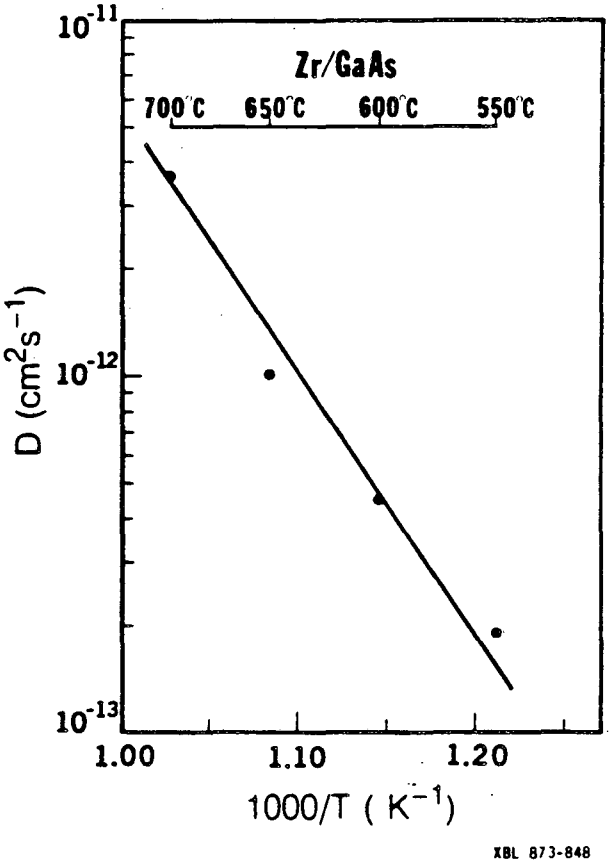

Figure 4.3 Figure 4.4

Figure 4.3 Plots of the square of GaAs consumed during Zr/GaAs reactions as measured by HIRBS versus annealing time for different annealing temperatures. The linear relationship shown in these plots indicate that the reactions are diffusion controlled.

Figure 4.4 An Arrhenius plot of the diffusivities as deduced from the slopes of the plots in Figure 4.3 versus the annealing temperatures in degree Kelvin. The activation energy of Zr/GaAs reactions is obtained from the slope of this plot and is =1.25±0.10 eV.

where K is a constant dependent on the frequency with which particles attempt to transform and the probability that during the time a particle or particles have the required energy to satisfy the geometrical or other conditions necessary for the change. The slow reactions rate

observed in this system despite its small activation energy thus lets us infer that the activation entropy ΔS for the Zr/GaAs reactions must be strongly negative so that the $\exp(\Delta S/k)$ term dominates in equation (4.1).

4.3 V/GaAs

Chemical reactions are detected at the V/GaAs interface by HIRBS during annealing at ~450 °C. HIRBS spectra from 1500 Å V/GaAs samples as deposited and annealed at 600 °C for 20 min and 700 °C for 30 min are displayed in Figure 4.5. The entire vanadium film is reacted in the sample annealed at 600 °C for 20 min. This is also confirmed by the XRD result on the same sample which shows no diffraction peak corresponding to unreacted V. The V signals in the HIRBS spectra from the two annealed samples indicate that two layer structures are formed in both cases with the top layer richer in vanadium than the interface layer. The presence of Ga signals in both samples at the surface can also be seen. Energy loss analysis shows reacted [V]:[GaAs] ratios ≈5:1 for the the sample annealed at 600 °C and ≈2.2:1 for the one annealed at 700 °C. Deconvolution of the HIRBS spectra from these two annealed samples are illustrated in Figure 4.6. Height ratio analysis of the backscattering yield from the individual element results in [V]:[Ga] ≈3:1, [V]:[As]≈2:1 and [V]:[Ga]≈1.2:1, [V]:[As]≈ 1.1:1 for the samples annealed at 600 °C and 700 °C, respectively.

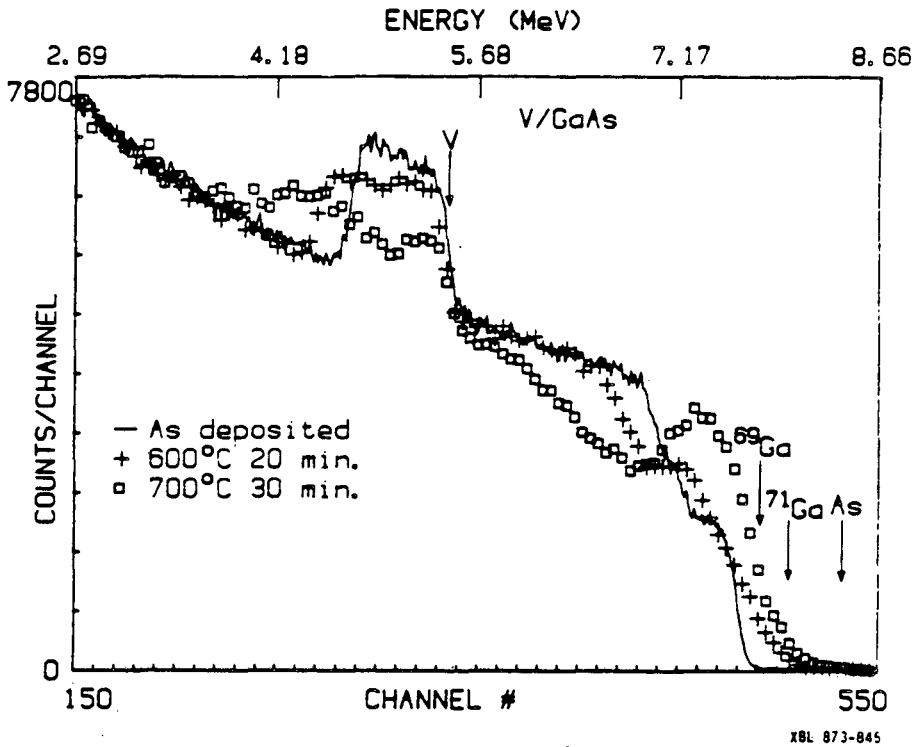

Figure 4.5 HIRBS spectra of 1500 Å V/GaAs samples as deposited and annealed at 600°C for 20 min and 700°C for 30 min.

X-ray diffraction patterns for the sample annealed at 700°C for 30 min match reasonably well with those for hexagonal V_6Ga_5 (a_o=8.496 Å and c_o=5.176 Å) and monoclinic V_4As_3 phase. For the sample annealed at 600°C for 20 min, only the cubic V_3Ga (a_o=4.8153 Å) phase can be identified by XRD. The other diffraction peaks in this XRD spectrum do not match with any of the available standard V-Ga or V-As patterns. From the HIRBS analysis, the other phase present in this sample is most probably V_2As. However, the structure of this V_2As phase is not known.

The HIRBS and XRD results show that the solid-state interactions at the V/GaAs interface proceed in two stages consistent with the following equations:

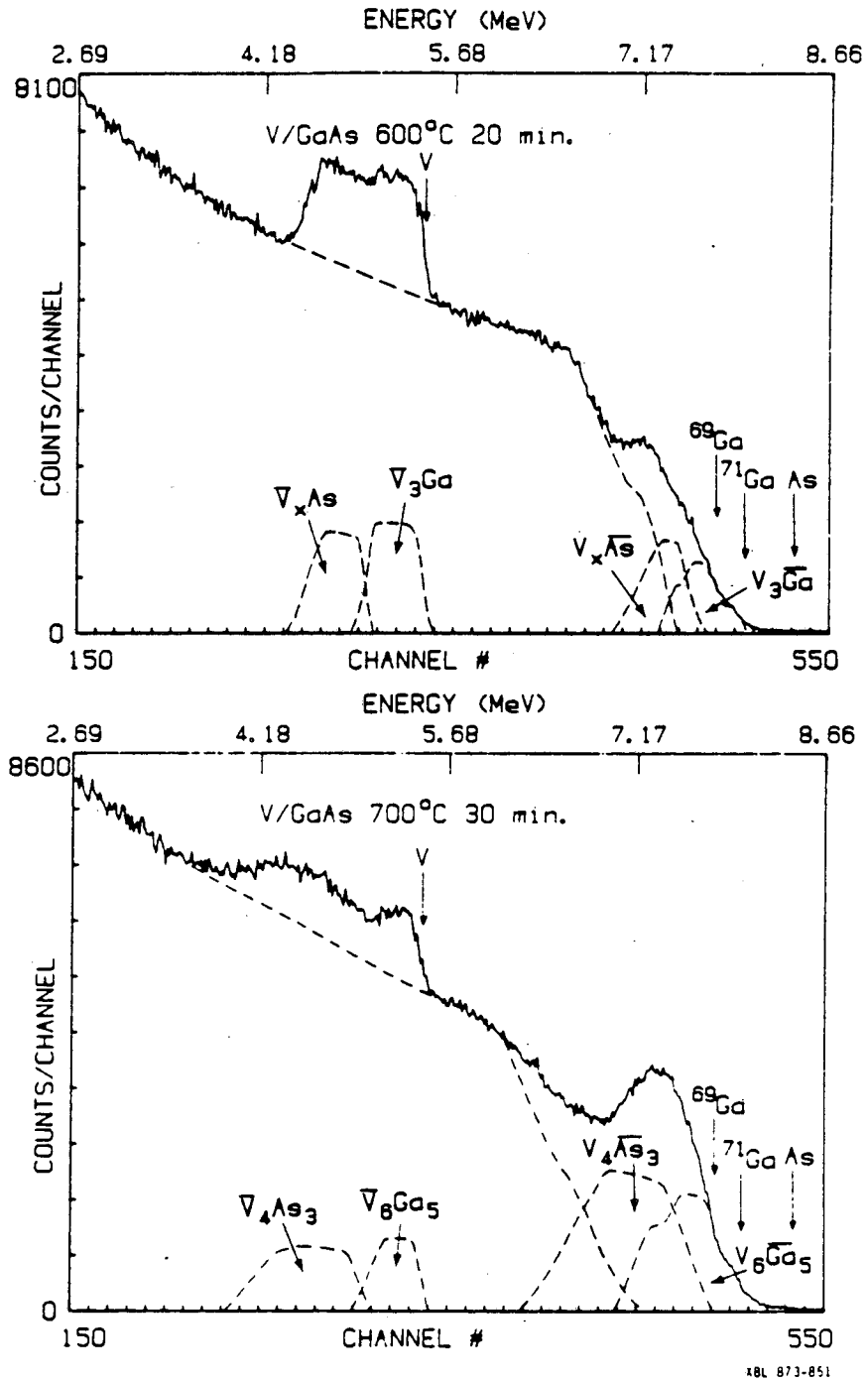

Figure 4.6 Deconvolution of the HIRBS spectra of the two annealed samples (600°C, 20 min and 700°C, 30 min) indicating layer sequence of V-Ga/V-As/GaAs for both samples with different V-Ga and V-As phases detected.

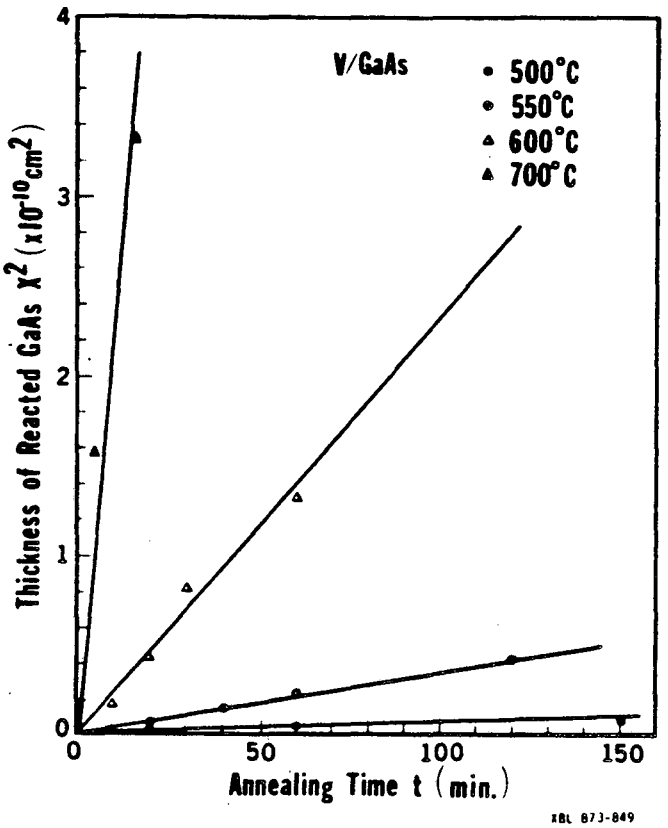

Figure 4.7

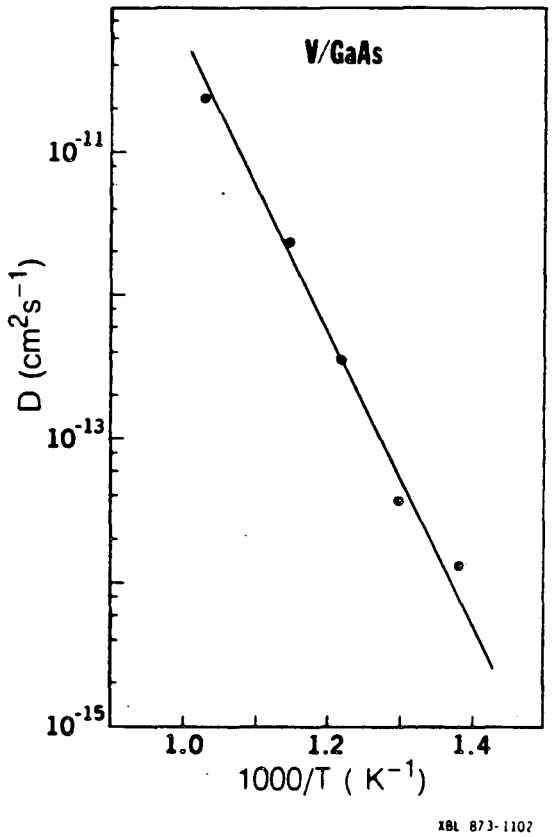

Figure 4.8

Figure 4.7 Plots of the square of GaAs consumed during V/GaAs reactions as measured by HIRBS versus annealing time for different temperatures.

Figure 4.8 An Arrhenius plot of the diffusivities versus the annealing temperatures for V/GaAs reactions. Activation energy obtained from this plot is =2.1±0.1 eV.

stage 1: $5\ V + GaAs \rightarrow V_3Ga + V_2As$, and

stage 2: $38V + 15GaAs \rightarrow 3V_6Ga_5 + 5V_4As_3$.

The fact that the ratio of the reacted [V]/[GaAs] for stage 2 reaction as measured by HIRBS is 2.2 instead of 2.5 is believed to be due to the effect arising from excessive energy straggling of the oxygen projectiles after passing through a thick layer. Table X summarizes the

HIRBS data for the 2-stage reactions of V/GaAs system. Layer sequence of V-Ga/V-As/GaAs is observed for all reacted layers in this system.

Measurements of the thickness of reacted GaAs in the annealed V/GaAs samples by HIRBS indicate that the reaction rate of this contact system is diffusion limited. The square root of time dependence of GaAs consumption during reaction is plotted in Figure 4.7. An Arrhenius plot of the diffusivities and annealing temperature is shown in Figure 4.8. The activation energy of the reactions estimated from these data is 2.1±0.1 eV. This high activation energy is consistent with the high annealing temperature (≥450°C) required to induce reactions at the interface.

Table X A summary of the HIRBS data from annealed V/GaAs samples showing 2-stage reactions.

	Reacted mater.	Atomic conc. in reacted phases	
	[V]/[GaAs]	[V]/[Ga]	[V]/[As]
stage 1	5.0±0.1	3.0±0.1	2.0±0.1
stage 2	2.2±0.2	1.2±0.1	1.1±0.1

4.4 Nb/GaAs

In contrast to the V/GaAs contact system, only one kind of reaction is observed in the Nb/GaAs system. Interactions between niobium metal film and GaAs are detected during annealing at 550 °C by HIRBS. Figure 4.9 shows the HIRBS spectra from 550 Å Nb/GaAs samples as deposited and annealed at 600 and 700 °C for 20 min. Total reactions of the 550 Å of Nb film is observed in the sample annealed at 700 °C for 20 min. The corresponding HIRBS spectrum shows that the surface is depleted of As and is relatively less rich in Nb concentration. The low energy tail of the Nb signal indicates that the interface between

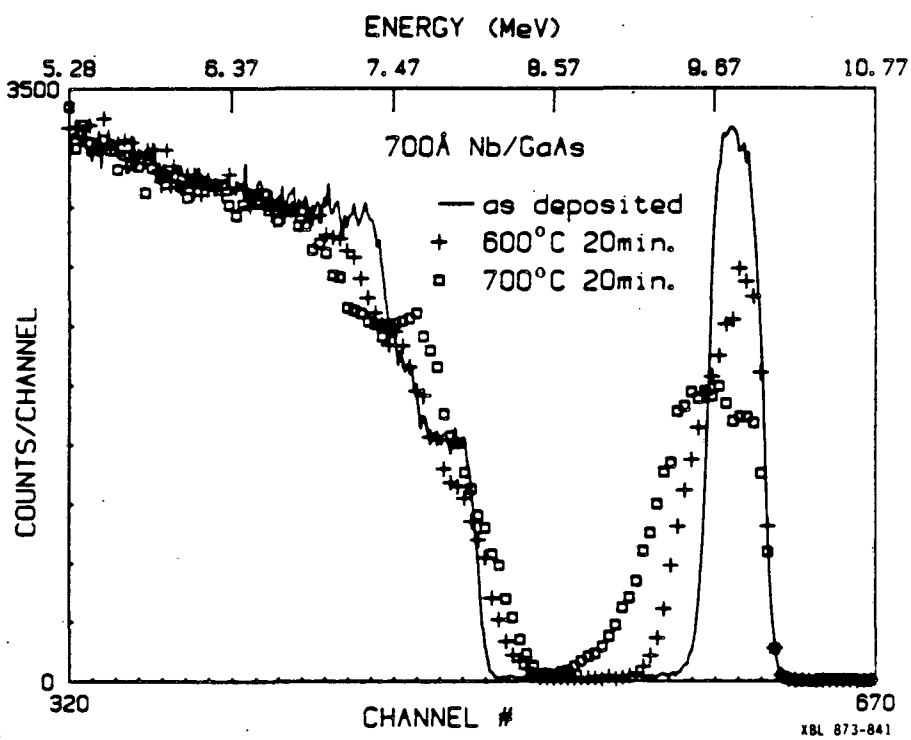

Figure 4.9 A series of HIRBS spectra of 550 Å Nb/GaAs samples as deposited and annealed at 600 and 700 °C for 20 min.

the reacted phases and the GaAs substrate is not uniform. Furthermore, the smoothness of the high energy signal of As is an indication of the fact that interpenetration of the top Nb-Ga and interface Nb-As phases occur.

The compositions of the reacted phases cannot be estimated from the HIRBS spectrum. The ratio of the total reacted Nb to GaAs is deduced from the spectrum and lies close to 1.55:1. XRD measurements on the sample annealed at 500°C shows a new set of diffraction peaks in addition to the vanadium diffraction peaks. This same set of peaks is also detected in the XRD spectra from the samples annealed at 600°C and 700°C and is observed to grow at the expense of the vanadium peaks. This indicates that there is only one set of stable phases in the Nb/GaAs reactions which gives rise to these diffraction peaks in the XRD spectra. However, no good match of this XRD pattern with any of the existing standard x-ray powder diffraction patterns from Nb-Ga and Nb-As phases can be found. From the XRD and HIRBS data, a schematic of the final structure of the Nb/GaAs contact after reactions is illustrated in Figure 4.10.

The amount of GaAs consumed during Nb/GaAs interface reactions is measured by HIRBS and is found to be dependent on the square root of the annealing time. This indicates that the reactions are controlled by a diffusion process. Because of the high annealing temperature (~550°C) needed in order to induce a reaction at the Nb/GaAs interface, the activation energy is expected to be high. HIRBS results yield an activation energy of ≈2.60 eV consistent with the observed annealing behavior of this system.

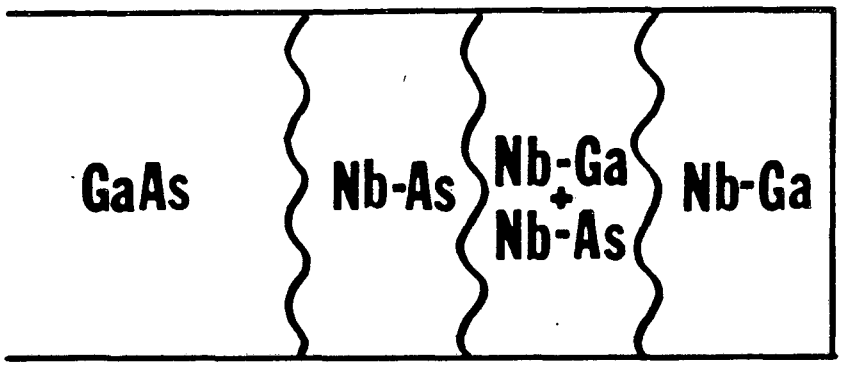

XBL 873-1105

Figure 4.10 A schematic diagram of the final structure of Nb/GaAs reactions as estimated from the HIRBS results.

4.5 Cr/GaAs

Interdiffusions and interactions at the Cr/GaAs interface are detectable by HIRBS during annealing at temperatures ≥450 °C. A set of HIRBS spectra from 1200 Å Cr/GaAs samples annealed at different conditions are shown in Figure 4.11. HIRBS spectra from the two annealed samples in the figure represent two stages of complete reactions of this system. Deconvolutions of the spectra from the two annealed samples are given in Figure 4.12. Layered structures are evident in the HIRBS spectra from both of the annealed samples.

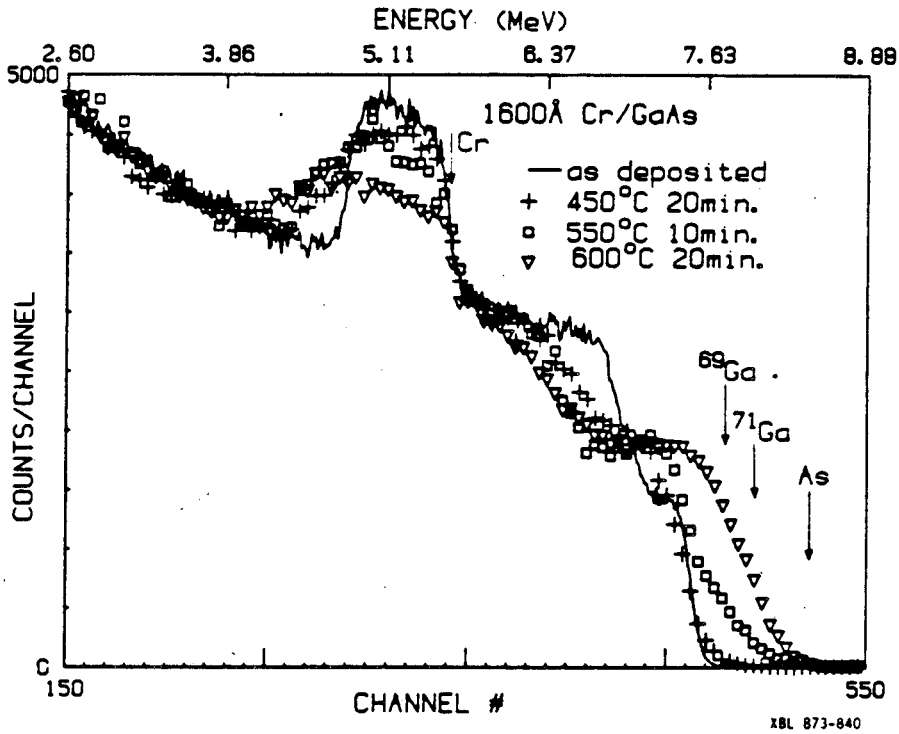

Figure 4.11 A series of HIRBS spectra of 1200 Å Cr/GaAs samples as deposited, annealed at 450°C for 20 min, 550°C for 10 min and 600°C for 20 min.

The first stage of complete reaction is observed in the sample annealed at 550°C for 10 min. In the HIRBS spectrum of this sample, the ratio of the reacted Cr to GaAs is estimated to be ≈3.9. Deconvolution of this spectrum yields [Cr]:[Ga]≈3:1 for the top layer and [Cr]:[As]≈1:1 for the layer at the GaAs interface. These results are consistent with the reaction:

$$4\ Cr + GaAs \rightarrow Cr_3Ga + CrAs,$$

and a layer sequence of Cr_3Ga/CrAs/GaAs. The second stage reactions are completed for this system after annealing at 600°C for 20 min.

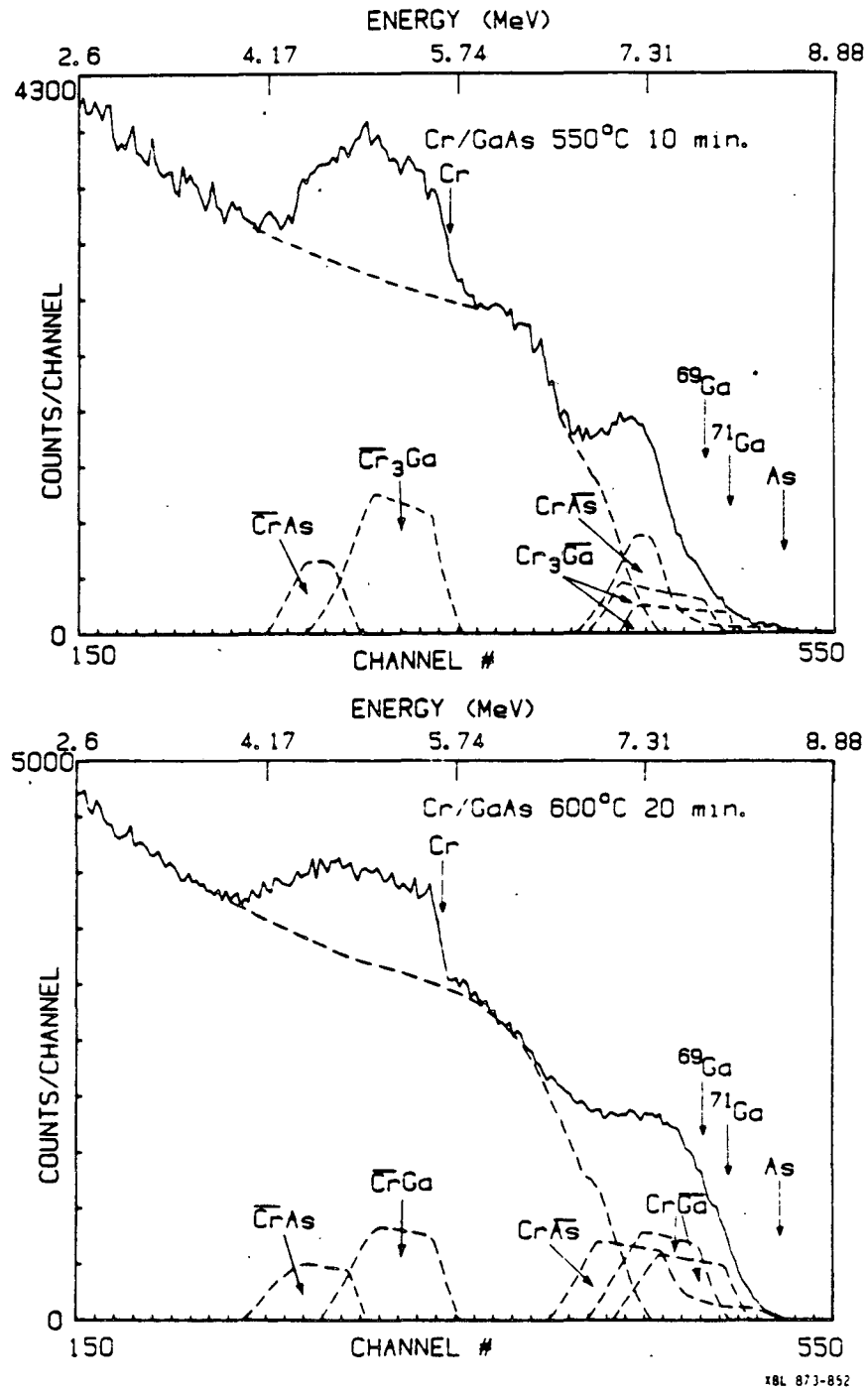

Figure 4.12 Deconvolution of the HIRBS spectra of Cr/GaAs samples annealed at 550°C for 10 min (a) and 600°C for 20 min (b) reveals the two layer structures in the samples. The two annealed samples represent two stages of complete reactions of the Cr/GaAs system.

Deconvolution of the HIRBS spectrum from this sample shown in Figure 4.12(b) reveals that the composition of the interface layer is similar to that of the stage 1 reactions. However, the [Cr]/[Ga] ratio in the top layer is changed from 3 to 1. Energy loss analysis gives a ratio of the reacted Cr to GaAs of ≈2.2 in this sample. These results are in good agreement with the reaction:

$$2\ Cr + GaAs \rightarrow CrGa + CrAs.$$

The layer sequence detected for this reaction is therefore CrGa/CrAs/GaAs. In both stages of reactions, a significant amount of As (10-20%), probably in the form of CrAs, is found in the top Cr-Ga layer.

Three phases are identified by XRD in Cr/GaAs samples annealed at temperature from 400°C to 700°C. Cubic Cr_3Ga of the β-W type (a_o=4.645 Å) and orthorhombic CrAs (a_o=3.486 Å, b_o=6.222 Å and c_o=5.741 Å) are the phases formed during stage 1 reactions in the temperature range of 450 to 550°C. At temperatures higher than 550°C, the Cr_3Ga phase becomes unstable and transforms into the more stable rhombohedral CrGa phase (a_o=9.01 Å and α=89°11'). XRD measurements on samples annealed at temperatures higher than 600°C do not show diffraction peaks different from those of the CrGa and CrAs phases. Therefore, the CrGa and CrAs phases are the stable final phases for the thin film Cr/GaAs contact system.

4.6 Mo/GaAs

HIRBS analysis on Mo/GaAs couples shows that the interface reaction is initiated at temperatures above 650°C. Figure 4.13 displays a series of HIRBS spectra from 1500 Å Mo/GaAs samples as deposited and annealed at 700°C for 40 min and 140 min. A well established layer structure is observed in the spectrum of a sample annealed at 700°C for 140 min in which complete reactions of the molybdenum film are observed. Figure 4.14 gives the deconvolution of this HIRBS spectrum which shows a layer sequence of Mo-Ga/Mo-As/GaAs formed after the reactions. The abruptness of the edges in the HIRBS spectrum infers that the interface between the two Mo phases and that between GaAs and Mo-As are rather sharp and uniform. This is consistent with the fact that the M-M bond for molybdenum is strong and thus producing fine grains in the reacted layer. In fact, Ling et al[13] measured an average grain size of ~100 Å using TEM for Mo/GaAs samples annealed at 700°C. XRD spectrum from this sample confirms that the entire Mo film is reacted with the substrate. HIRBS spectra from samples annealed at temperatures ranging from 750 to 850°C are identical to that from the sample annealed at 700°C for 140 min. This indicates that the phases formed at 700°C are thermally very stable.

From the Mo backscattered signal in Figure 4.14, it is obvious that the top Mo-Ga phase is richer in Mo than the interface Mo-As phase. Ratios of the backscattered yields give [Mo]:[Ga]≈2.5:1 for the top layer and [Mo]:[As]≈1.2:1. XRD results on samples annealed at temperatures ranging from 700 to 850°C show the presence of two phases:

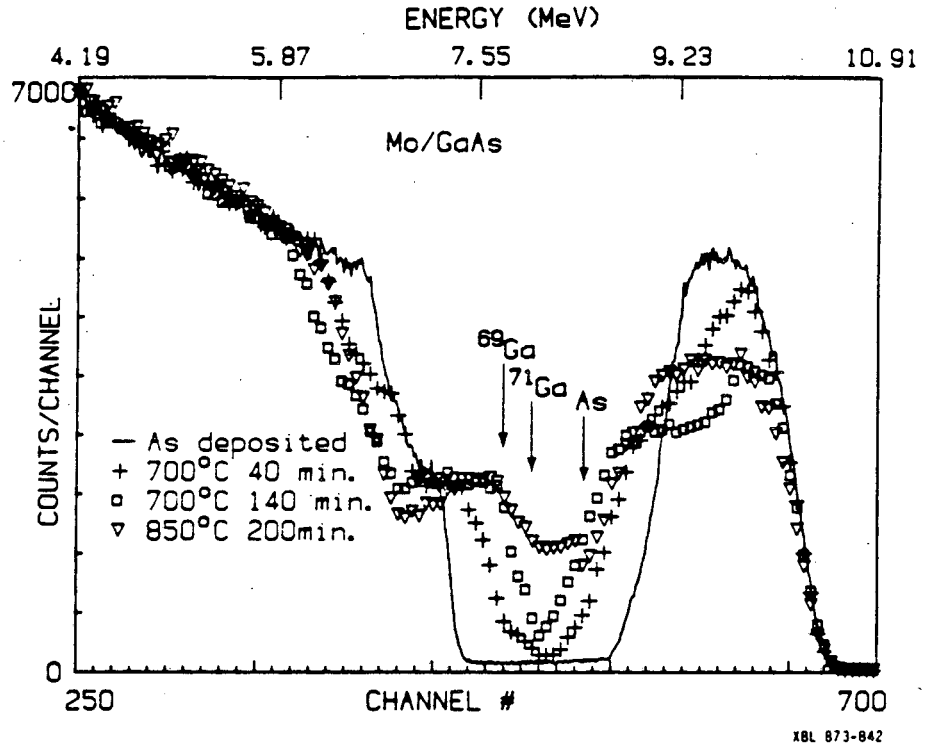

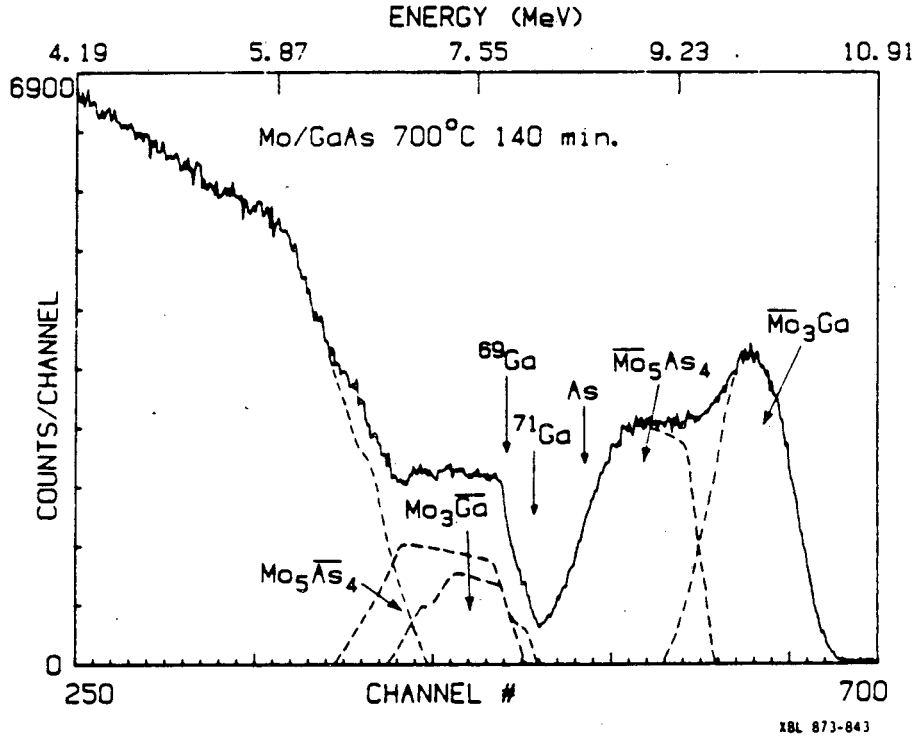

Figure 4.13 A series of HIRBS spectra of 1500 Å Mo thin film on GaAs samples as deposited, annealed at 700°C for 40 min, 700°C for 140 min and 850°C for 200 min.

Figure 4.14 Deconvolution of the HIRBS spectrum of the Mo/GaAs sample annealed at 700°C for 140 min. Well defined layer sequence of Mo-Ga/Mo-As/GaAs is clearly observed.

the cubic Mo_3Ga (a_o=4.943 Å) and the tetragonal Mo_5As_4 (a_o=9.6 Å and c_o=3.278 Å). The apparent discrepancy in the composition of the Mo-Ga phase as measured by HIRBS and XRD probably stems from the many Mo isotopes which are only partially resolved by HIRBS. This isotopic spread reduces the height of the Mo signal by ~15-20%. From the HIRBS and XRD results the structure of Mo_3Ga/Mo_5As_4/GaAs can be deduced for the Mo/GaAs reactions at the temperature range of 700 to 850°C.

Annealing the Mo/GaAs system at temperatures higher than 850°C shows drastic changes in the reacted layer as indicated in the HIRBS spectrum from the sample annealed at 900°C for 20 min (Figure 4.15). This spectrum indicates that both, Ga and As, are now present in the top layer while the Mo content in the reacted layer becomes more uniform. The uniform nature of the GaAs interface is still maintained. Deconvolution of this spectrum is very difficult because of the extensive signal overlapping. XRD analysis on this sample reveals that diffraction peaks from the Mo_3Ga phase disappear while new sets of diffraction peaks emerge. One set of the peaks can be identified as those from the monoclinic $MoAs_2$ phase (a_o=9.069 Å, b_o=3.2996 Å, c_o= 7.717 Å and β=119.37°) while the other set of peaks do not match with those of the existing powder diffraction data from any of the binary Mo-Ga or Mo-As phases.

Suh et al[14] have explored the high temperature annealing effects of the Mo/GaAs system. They found that at annealing temperatures higher than 850°C, a new phase is formed. Using AES and SIMS analysis, they concluded that this is a ternary phase with composition of

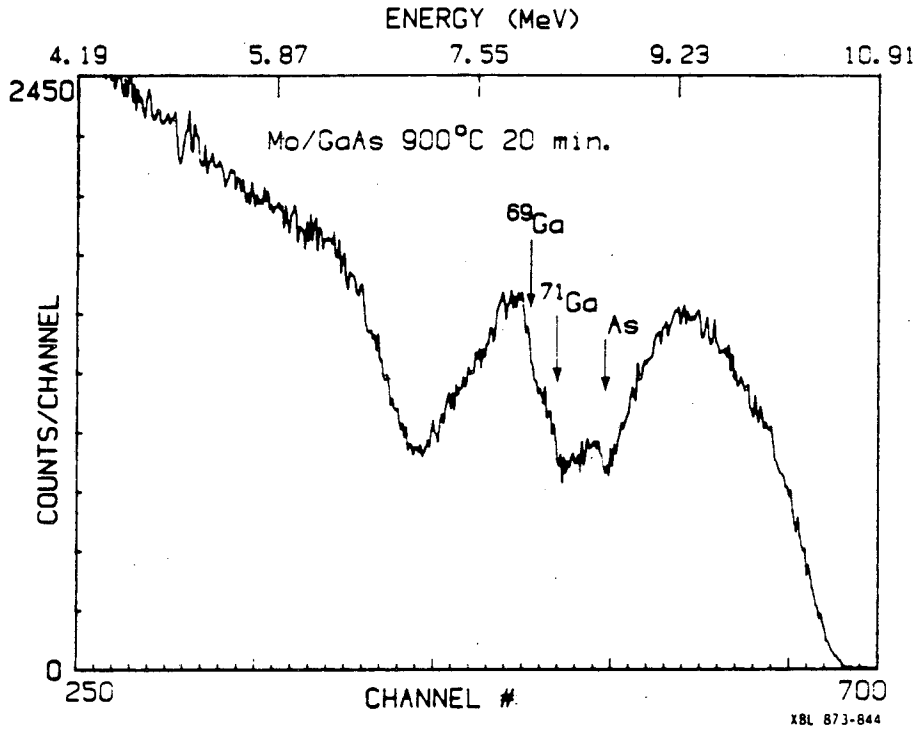

Figure 4.15 HIRBS spectrum of Mo/GaAs sample annealed at 900 °C for 20 min showing drastic changes in the features as compared to the spectrum of samples annealed at lower temperatures.

Mo_3GaAs_2. Their XRD results on this ternary phase match reasonably well with the new phase identified in the same temperature range in the present study. The structure and the exact composition of this ternary phase are still not well known. But from the HIRBS analysis, it is likely that this ternary phase is the result of the transformation of the Mo_3Ga phase as more As diffuses to the top layer at high temperatures.

HIRBS determinations of the quantity of reacted GaAs for Mo/GaAs system undergoing isochronic annealing at temperatures below 700 °C reveals that the rate of reaction bears a linear relationship with the

annealing time. Figure 4.16 shows plots of ln x versus ln t where x is the amount of reacted GaAs in molecules/cm^2 and t is the annealing time in min. Note that for 650°C annealing the slope of the plot is ≈1 indicating that the reaction rate is proportional to time. This linear reaction rate has been observed very often in the formation of many refractory metal disilicides such as $TiSi_2$, VSi_2, $CrSi_2$, $NbSi_2$, $MoSi_2$, WSi_2, etc. This type of reactions is said to be controlled by the rate of reaction at the M-MSi_2 interface[15-17]. The exact mechanism leading to this linear growth rate is still not understood. However, recent work of refractory metals[18] deposited on Si in high vacuum (<10^{-7} Torr) resulted in parabolic growth rate of the disilicide instead of the linear rate observed in previous studies. This led to the speculation that the presence of native oxide at the metal/silicon interface is responsible for the different growth rate for refractory metal silicides. For M/GaAs reactions, this linear growth rate has not been reported. This may be due to the fact that the native oxide on GaAs is thinner than that on Si and thus normally do not play an important role in M/GaAs reactions.

Figure 4.16 also shows a plot of ln x versus ln t for annealing at 700°C. The slope for this plot is ≈0.5 which shows that the reaction is diffusion controlled as observed for other metal/GaAs reactions studied in this work. The reactions at temperatures higher than 700°C proceed very rapidly. These are believed to be nucleation controlled reactions as observed in high temperature annealing of the Ir/GaAs case.

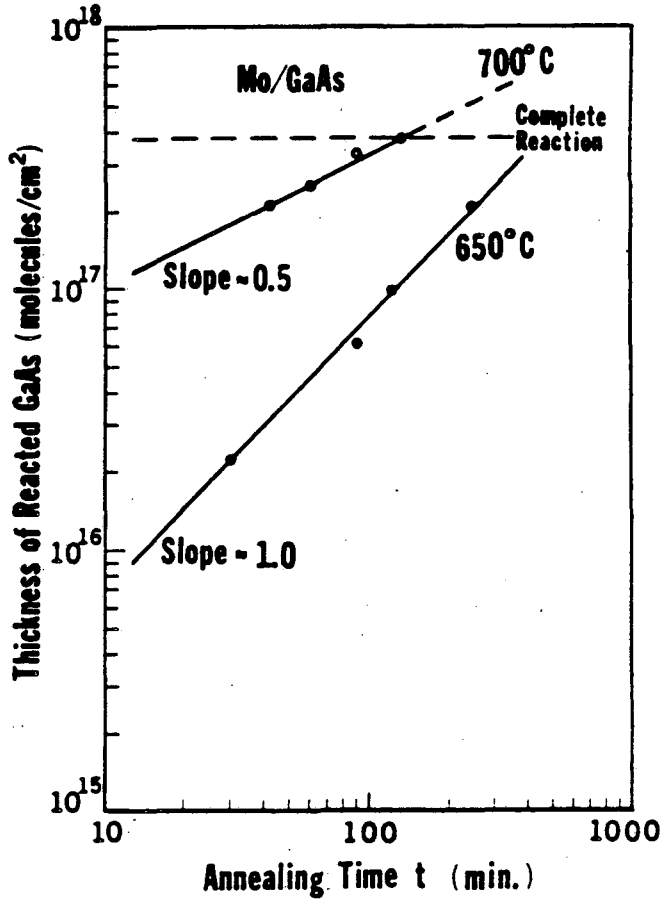

Figure 4.16 Plots of the reacted GaAs thickness as a function of the annealing time in the logarithm scale for Mo/GaAs reactions at 650 and 700 °C. The slopes of the plots indicate that the reactions at 650 °C (slope =1) are reaction rate limited and the reactions at 700 °C (slope=0.5) are diffusion limited.

4.7 W/GaAs

Glancing angle RBS spectra from samples of 180 Å W/GaAs as deposited and annealed at 650, 750, 800 and 900 °C are shown in Figure 4.17. Below 650 °C no changes can be detected in the RBS spectra. At annealing temperatures between 650 and 800 °C, interdiffusion of W and

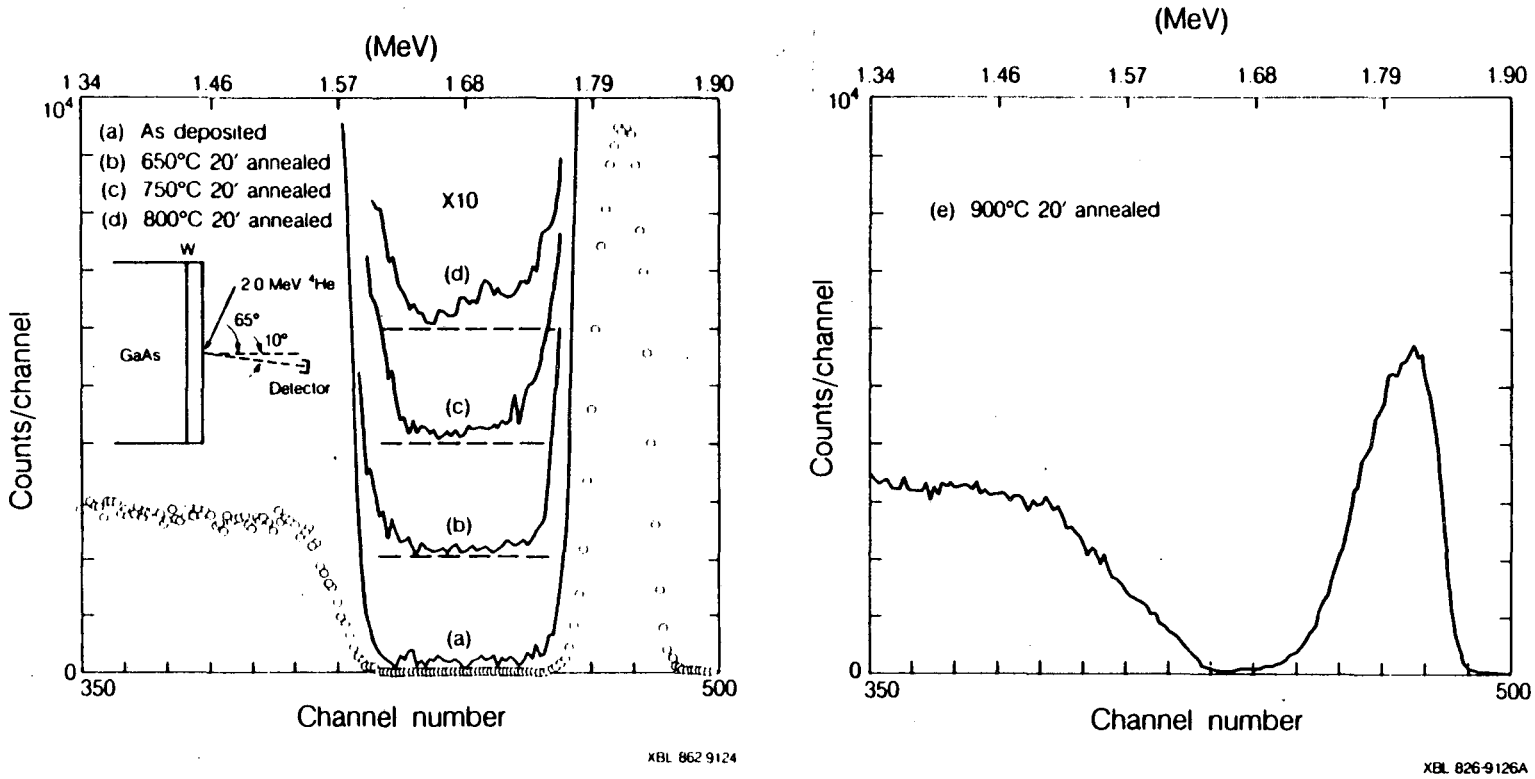

Figure 4.17 (a)-(e) Glancing angle RBS spectra of 180 Å W/GaAs samples as deposited and annealed for 20 min at 650, 750, 800, and 900 °C.

GaAs is observed. The W diffusion profiles in GaAs at various temperatures, as measured by RBS, are shown in Figure 4.18. Note that after annealing at 800°C for 20 min, there is ~0.2 at. % ($8X10^{19}cm^{-3}$) of W present at 600 Å below the W/GaAs interface. The distribution profiles of W in GaAs shown in Figure 4.18 are of the form $C(x)=C_o\exp(-x/\delta)$. For such a plot a characteristic distance δ can be defined and is determined from the inverse slope of the plot. A plot of δ versus square root of time for samples annealed at 700°C is shown in Figure 4.19. The linear relationship in this figure confirms that we observed a simple diffusion process with $\delta=2(Dt)^{1/2}$ where D is the diffusion constant of the diffusing species. From values of D obtained in this way, an Arrhenius plot of $\ln(D)$ versus $1/T$ is obtained and is shown in Figure 4.20. From the slope and intercept of the curve in Figure 4.20 and following the equation for diffusion $D=D_o\exp(E/kT)$, the activation energy of W diffusion in GaAs is found to be $\Delta E=1.87\pm0.65$ eV with the prefactor $D_o=7.3X10^{-7}cm^2/s$.

GaAs out-diffusion is also evident in the spectra at annealing temperatures between 650 and 800°C. It is obvious that As diffuses into the W overlayer. However, corresponding Ga out-diffusion cannot be identified by RBS measurements due to overlapping of Ga and As backscattering signals. Possible reactions between W and GaAs are observed for samples annealed at temperatures >850°C. Atomic compositions of the reaction products cannot be determined by RBS because of the non-abrupt nature of the backscattering spectra.

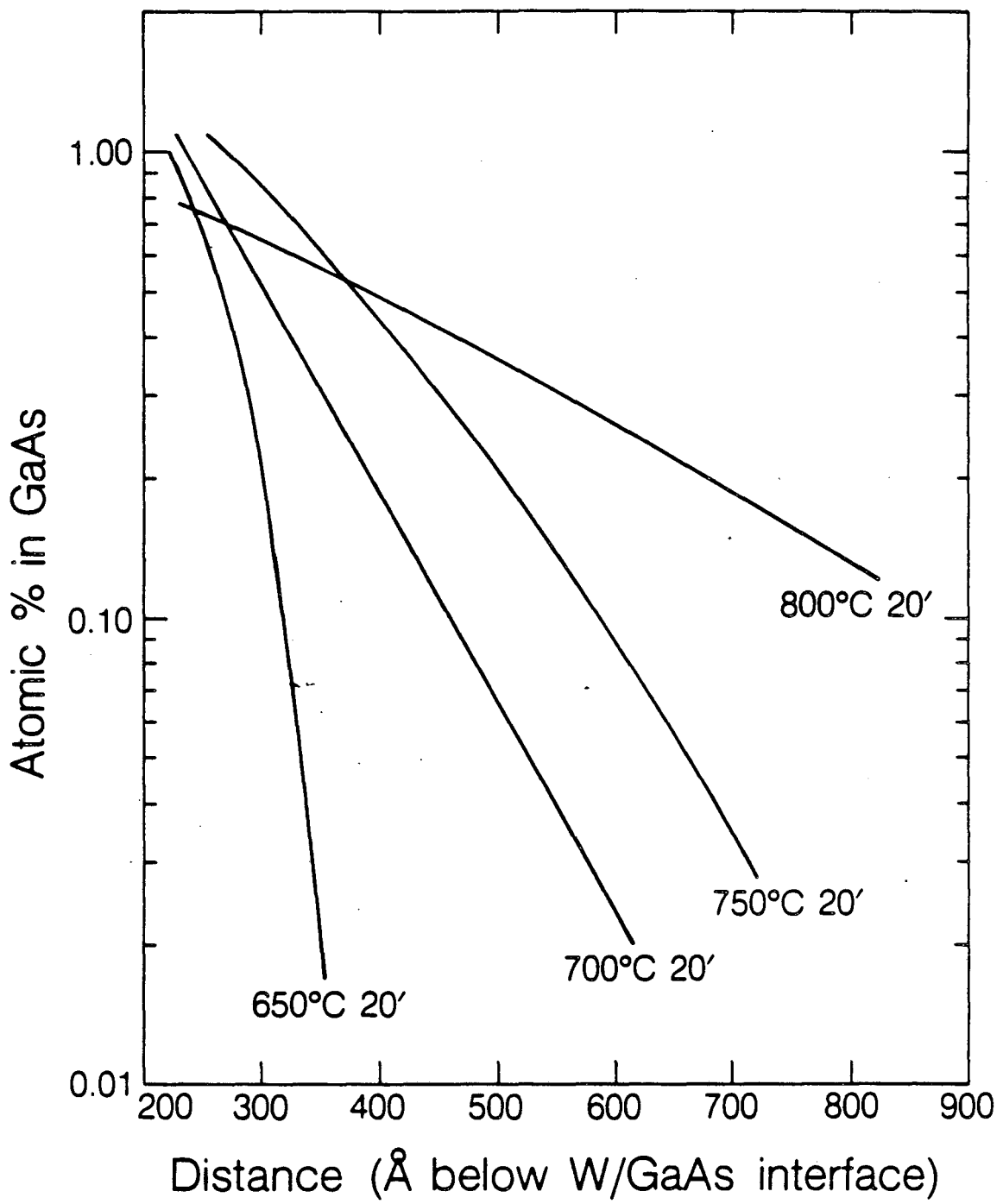

XBL 862-9133

Figure 4.18 W diffusion profiles in GaAs at various temperatures as measured by RBS.

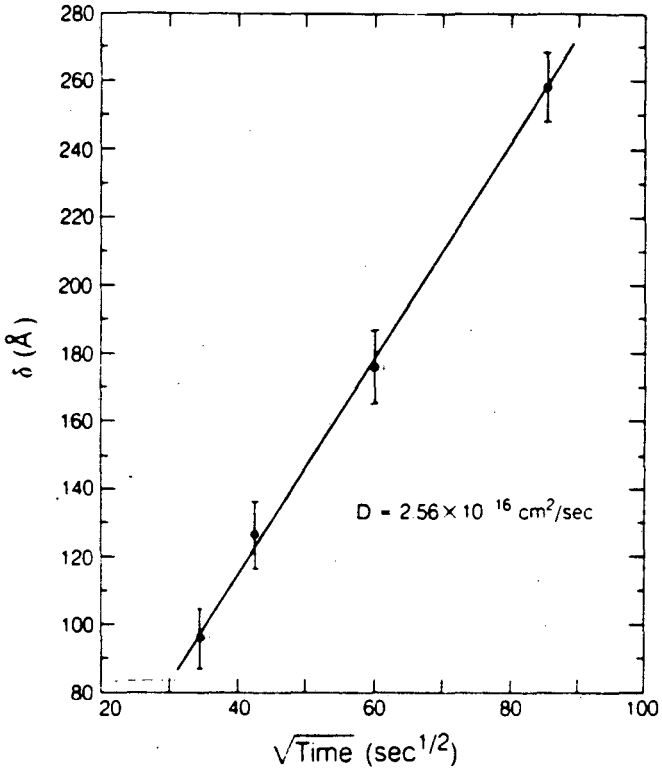

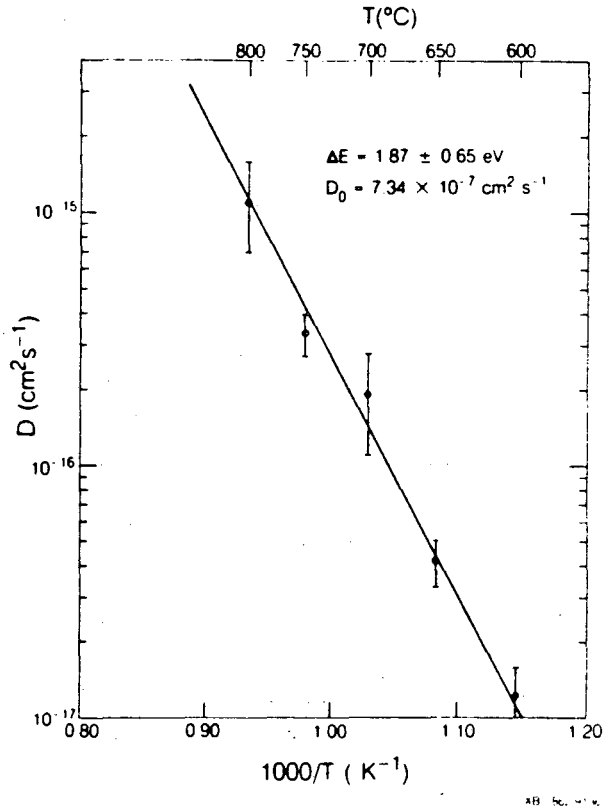

Figure 4.19 Figure 4.20

Figure 4.19 Characteristic diffusion depth δ versus √time for W/GaAs samples annealed at 700 °C for various time durations.

Figure 4.20 A plot of diffusion coefficient D calculated from Figure 4.18 versus the reciprocal of annealing temperature in degree Kelvin.

RBS spectra from the thick W layer (1800 Å) on GaAs as deposited and annealed at 900 °C are shown in Figure 4.21. No change is observed for the outer 1500 Å of W. Reactions between W and GaAs are confined to the ~300 Å of W at the interface.

Figure 4.22 shows a series of scanning electron micrographs for W/GaAs samples as deposited and annealed at 300, 700 and 900 °C. A

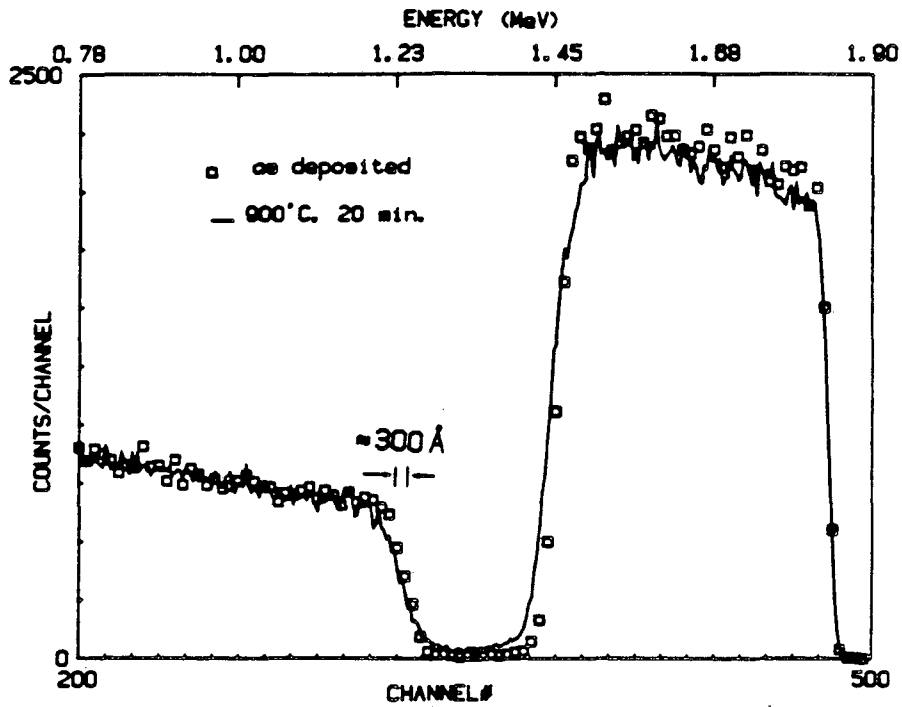

Figure 4.21 RBS spectra of 1800 Å W/GaAs samples before and after annealing at 900 °C for 20 min indicating interactions at the interface after annealing.

morphologically smooth W film on the GaAs substrate is observed in the sample annealed at 300 °C. After 700 °C annealing, the edge between the W film and the GaAs substrate starts to form voids, indicating that the W/GaAs interface is becoming "rough." Annealing at 900 °C results in more voids at the interface and a nonuniform W film with holes appearing at the W surface.

Electron diffraction patterns for thin (~180 Å) W layers in GaAs as deposited and annealed at 750 and 900 °C with their corresponding bright field images are shown in Figure 4.23. The as deposited film shows a fine grain size of ~70 Å. From the diffraction pattern this

as deposited

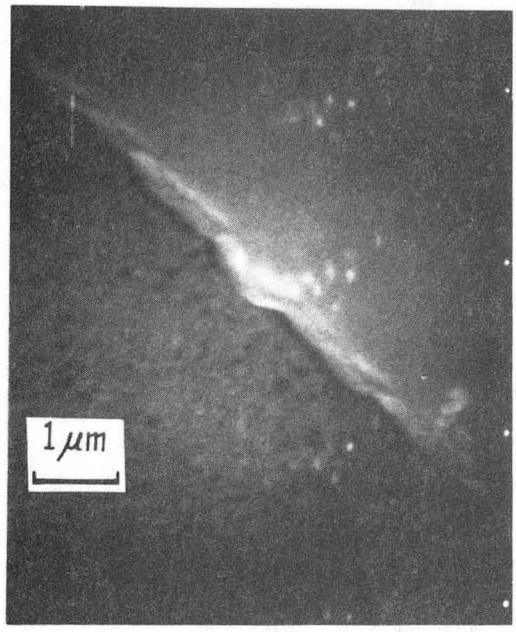

300C 20min.

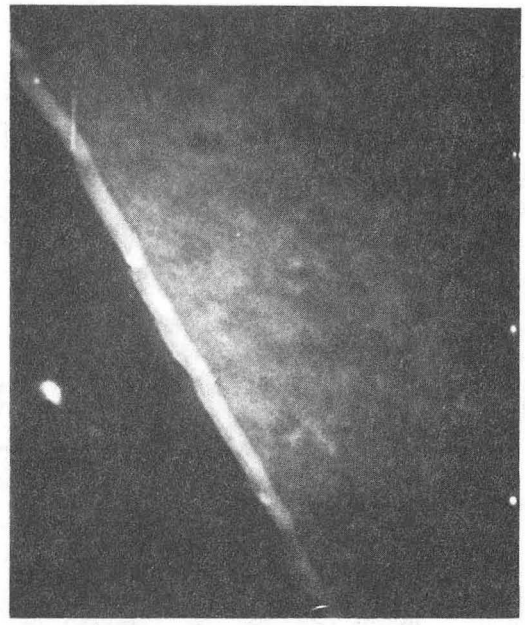

700C 20min.

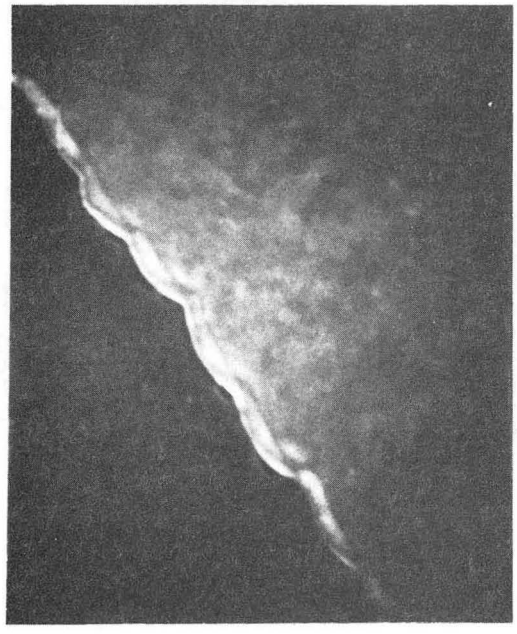

900C 20min.

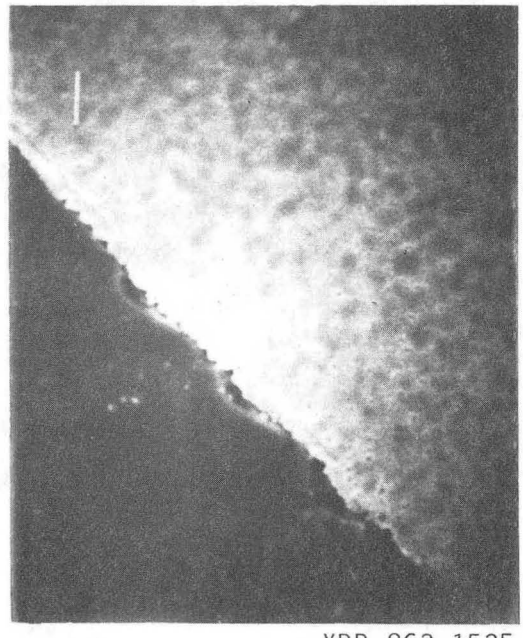

XBB 863-1535

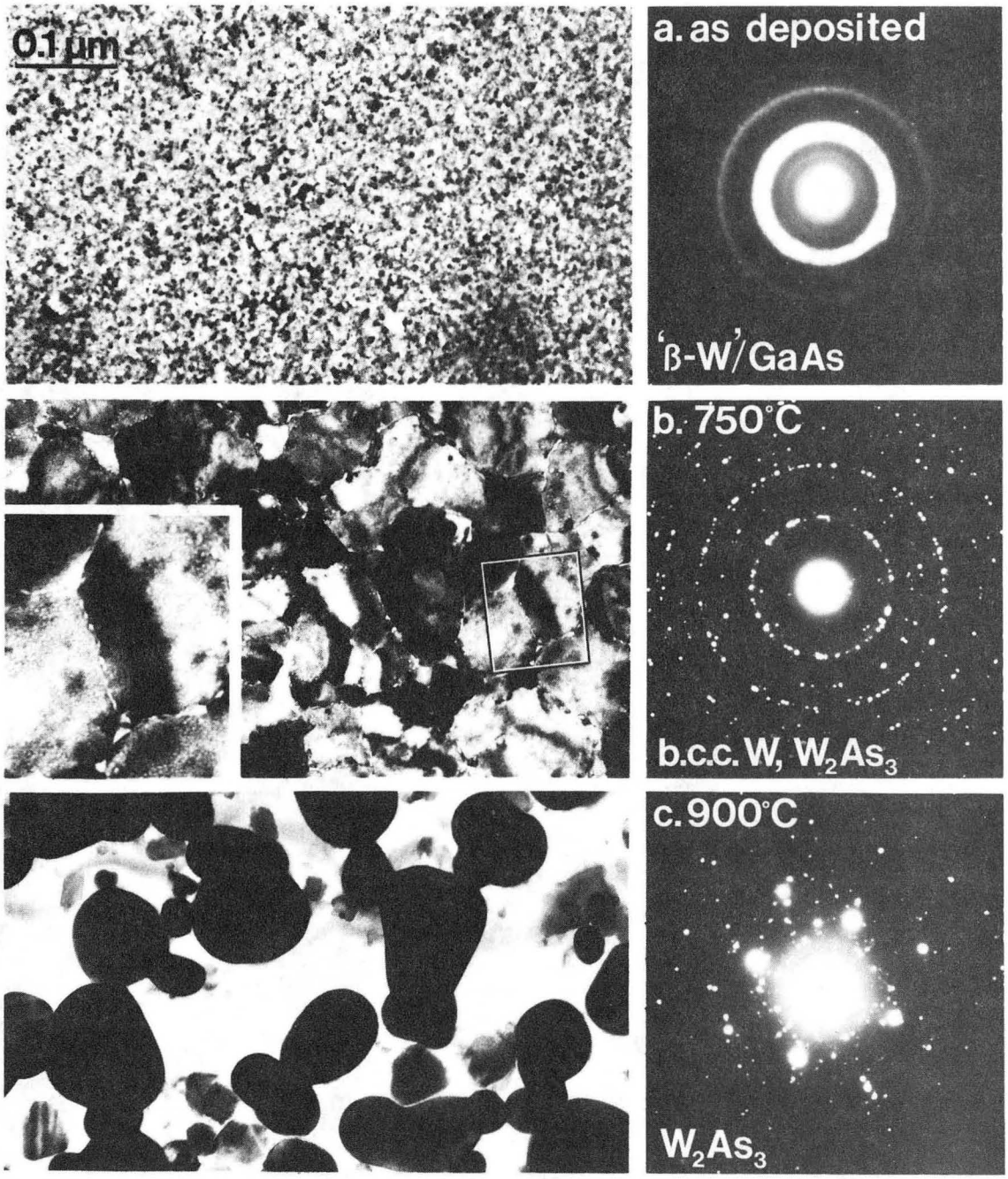

XBB 863-1792

fine-grained layer is identified as β-W phase with A15 crystal structure[19]. However, the (100) and (110) diffraction rings which are kinematically forbidden in a perfect A15 structure, are faintly visible in the diffraction pattern. This suggests that the sputtered W film may contain defects (vacancies, interstitials or impurities) at a high concentrations. After annealing at 750°C for 20 min, the film transforms into bcc α-W with large grain size (~900 Å). The electron diffraction pattern of this sample indicates that a small amount of W_2As_3 is present. Small voids also appear at the grain boundaries covering ~1% of the total surface.

Micrographs for samples annealed at 900°C for 20 min show that the W film balls up and forms spherical grains of ~1000 Å in diameter on the GaAs substrate. About 60% of the GaAs surface is exposed. Diffraction patterns of the individual grain indicate that these islands formed are single grains of W_2As_3 with a monoclinic structure. Since a diffraction data file for other W-Ga or W-Ga-As phases is not available for comparison, the presence of these phases as reaction products cannot be ruled out. The electron diffraction data for the samples as deposited and annealed at 750 and 900°C are shown in Table XI. X-ray diffraction data for the α-W, β-W and W_2As_3 phases taken from the JCPDS powder diffraction file are also shown in the table.

Figure 4.22 (page 161) Scanning electron micrographs of 1800 Å W on GaAs samples as deposited and annealed at 300, 700, and 900°C.

Figure 4.23 (a)-(c) (page 162) TED patterns for W/GaAs samples as deposited and annealed at 750 and 900°C with their corresponding TEM bright field images.

TABLE XI. Electron diffraction data[a] of W/GaAs samples as-deposited and annealed at 750°C and 900°C for 20 min. X-ray powder diffraction data of α-W, β-W and W_2As_3 phases taken from the JCPDS diffraction file are also shown for comparison.

Transmission Electron Diffraction Data			X-Ray Powder Diffraction Data [b]		
as-deposited	750°C 20 min	900°C 20 min	β-W	α-W	W_2As_3
	0.79				0.787(001)
	0.58	0.59			
	0.56				0.548(200)
0.507(w)			0.504(100)[c]		
	0.473	0.467			0.472(20$\bar{2}$)
	0.424				
0.359(w)	0.366		0.356(110)[c]		0.363(201)
	0.330				0.330(40$\bar{2}$)
0.257(m)	0.264	0.262	0.252(200)		0.263(311,003)
		0.233			0.232(20$\bar{4}$)
0.229(s)	0.225(s)	0.226	0.225(210)	0.224(110)	0.227(31$\bar{3}$)
0.206(m)			0.206(211)		0.207(51$\bar{2}$)
	0.175				0.179(312)
	0.158	0.157		0.158(200)	0.156–0.159(220, 60$\bar{6}$,601,40$\bar{6}$)
	0.151	0.151			0.151(022,11$\bar{5}$)
0.146(w)			0.145(222)		
	0.142				0.142(512,42$\bar{3}$)
0.140(m)			0.140(320)		
0.135(w)			0.134(321)		
	0.130(s)	0.129		0.129(211)	

[a]All plane spacings are in nm. X-ray data is indexed with hkl in parentheses. (w), (m) and (s) denote weak, medium and strong intensity diffraction rings, respectively.

[b]X-ray data for α-W, β-W and W_2As_3 are from cards 2-1138, 4-806 and 18-1415 of the JCPDS powder diffraction file.

[c]These reflections are kinematically forbidden for a perfect A15 structure.

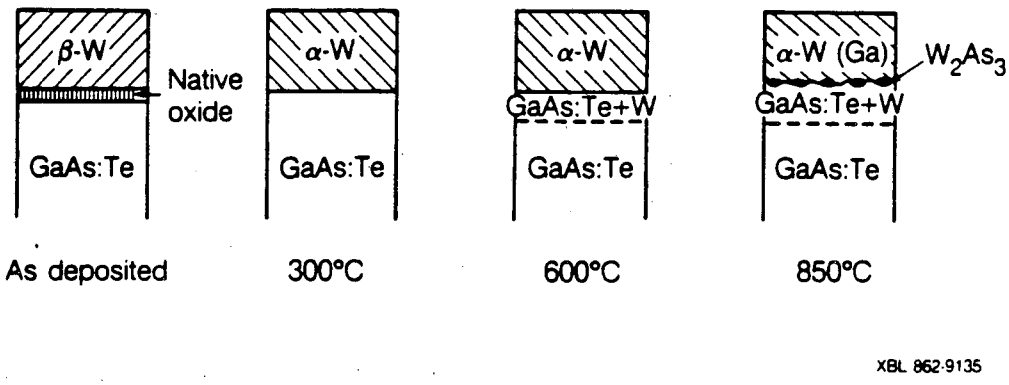

Figure 4.24 Schematic diagrams for the structural evolution of the W/GaAs contact as it proceeded through ever higher annealing temperatures.

From the RBS, SEM and TEM results on the W/GaAs system, it can be concluded that this contact is thermally very stable. Interdiffusion of W and GaAs occurs at the interface at temperatures higher than 600 °C. Upon heat treatment at temperatures higher than 800 °C, macroscopic reactions are initiated at the interface forming islands of W_2As_3 phase resulting in a very rough interface. A schematic diagram for the structure of the contact as it proceeds through ever higher annealing temperatures is shown in Figure 4.24.

4.8 Summary and Conclusions on Refractory Metal/GaAs Reactions

4.8.1 Phase composition and structure

1) Except for Mo, the final stable phases are always binary (M_xGa and M_yAs where $x \geq 1$ and $y \leq 1$). For Ti, Zr and V the stable M_xGa phases have hexagonal structure with x ranging from 1 to 1.7.

The stable phases for the Mo/GaAs system are believed to be the binary $MoAs_2$ and the ternary Mo_xGaAs_y with $x \approx 3$ and $y \approx 2$. The exact composition and structure of this ternary phase is still unknown.

2). The ratio of the amount of reacted metal to GaAs, [M]/[GaAs] in the final reacted layer is normally ≥ 1.5. This does not apply to the W/GaAs system since it is thermally very stable and the reactions occur at the interface at high temperatures are nonuniform. For Ti, Zr, V and Cr, this ratio is 2.

3) For systems which react in two stages, the intermediate phases formed are binary phases. These intermediate phases are most commonly the cubic M_3Ga phases as observed for the V, Cr and Mo cases.

4.8.2 Phase distribution and morphology

1) Vertical phase distribution is always observed for all refractory metal/GaAs systems except for W/GaAs. This can be explained by the M-M bond strength argument given in the last chapter. Since refractory metals have stronger M-M bonds, and therefore larger heats of vaporization, grain size in the reacted layer is smaller. Thus phase stratification is energetically more favorable.

2) The phase in intimate contact with the GaAs substrate is usually the M-As phase. This may seem to be a peculiar phenomenon for metals such as Ti and Zr which have electronegativity numbers (X=1.5) lower than that of Ga. However, it

can be argued that it is the electropositive metal atoms which are strongly attracted to the electro-negative As (X=2.0) giving rise to the observed M-Ga/M-As/GaAs structure. Therefore, the electronegativity argument still holds for refractory metal/GaAs reactions.

3) The interfaces between different phases are normally non-uniform. This is not surprising since the refractory metals normally have electronegativity in between those of Ga and As so that in many cases they are attracted to both the Ga and As atoms.

4.8.3 Reaction kinetics

1) Initial reactions at refractory metal/GaAs interfaces do not begin at temperatures lower than 450°C. This high reaction temperature is also a result of the electropositive nature of these metals. Therefore, the refractory metal/GaAs interfaces are said to be relatively inert.

2) A parabolic reaction rate is observed for most systems except for the Mo/GaAs indicating that for most of the systems the diffusion process dominates the interface reactions.

3) For Mo/GaAs, the reactions at 650°C exhibit a linear relationship with time. This interface reaction rate controlled process has been observed for the formations of many refractory metal disilicides but has not been observed in any metal/GaAs systems. For high temperature reactions of the Mo/GaAs

system, the reaction rate is very rapid and is believed to be nucleation controlled.

4) Similar to the near noble metal/GaAs interface reactions, only one activation energy ΔE is found for each system with values of ΔE ranging from 1.25 to 2.6 eV. The single activation energy for systems which undergo 2-stage reactions such as V/GaAs and Zr/GaAs can also be explained by the same free energy argument given in section 2.7.3 and Figure 3.28 for the near noble metal/GaAs interface reactions.

REFERENCES TO CHAPTER 4

1. N. Yokoyama, T. Minura, M. Fukuta and H. Ishikawa, 1981 International Solid State Circuits Conference Digest of Technical Papers, p.218 (1981).

2. K. Matsumoto, N, Hashizume, H. Tanoue and T. Kanayama, Jpn. J. Appl. Phys. **21**, L393 (1982).

3. N. Yokoyama, T. Ohnishi, K. Odani and M. Abe, IEEE International Electron Devices Meeting Technical Digest, p. 80 (1981).

4. W. F. Tseng and A. Christou, IEEE International Electron Device Meeting Technical Digest, p. 174 (1982).

5. J. K. Truman and P. H. Holloway, J. Vac. Sci. Technol. **A3**, 992 (1985).

6. N. Yokoyama, T. Ohnishi, T. Nukamura and H. Nishi, Mat. Res. Soc. Symp. Proc. **54**, 401 (1986).

7. T. Ohnishi, N. Yokoyama, H. Onodera, S. Suzuki and A. Shibatomi, Appl. Phys. Lett. **43**, 600 (1983).

8. J. R. Waldrop, Appl. Phys. Lett. **43**, 87 (1983)

9. H. Yamagishi, Jpn. J. Appl. Phys. **23**, L895 (1984).

10. O. Wada, S. Yanagisawa and H. Takanashi, Appl. Phys. Lett. **29**, 263 (1976).

11. S. D. Mukherjee, D. V. Morgan, M. J. Howes, J. G. Smith and P. Brook, J. Vac. Sci. Technol. **16**, 138 (1979).

12. S. D. Mukherjee, C. J. Palmstrom and J. G. Smith, J. Vac. Sci. Technol. **17**, 904 (1980).

13. P. Ling, J-K. Chang, M-S. Lin and J-C. Lou, Mat. Res. Soc. Symp Proc. **48**, 137 (1985).

14. K. Suh, H. K. Park and K. L. Moazed, J. Vac. Sci. Technol. **B1**, 365 (1983).

15. K. N. Tu and J. W. Mayer, "Silicide Formation" in *Thin Film-Interdiffusion and Reactions*, eds. J. M. Poate, K. N. Tu and J. W. Mayer, Chapter 10 (Wiley, New York, 1978).

16. F. M. d'Heurle and P. Gas, J. Mat. Res. **1**, 205 (1986).

17. L. D. Locker and C. D. Capio, J. Appl. Phys. **44**, 4366 (1973).

18. L. S. Hung, J. Gyulai and J. W. Mayer, J. Appl. Phys. **54**, 5076 (1983).

19. P. Petroff, T. T. Sheng, A. K. Sinha, G. A. Rozgonyi and F. B. Alexander, J. Appl. Phys. **44**, 2545 (1973).

Chapter 5. RESULTS AND DISCUSSIONS III: CORRELATIONS BETWEEN ELECTRICAL BEHAVIOR AND INTERFACE METALLURGY FOR METAL/GaAs CONTACTS

From the results presented in the last two chapters, metal/GaAs interfaces can be classified into three categories according to their interface reactivity:

1. Very reactive systems which include Ni/GaAs, Co/GaAs and Pd/GaAs. These systems react at temperatures below 300 °C forming ternary intermediate phases.
2. Reactive systems which include Rh/GaAs and Pt/GaAs. These systems react at temperatures around 350 to 400 °C.
3. Non-reactive systems which include most of refractory metal. Interactions at these interfaces do not occur at temperatures below 450 °C. Among these, the W/GaAs system is the most stable interface wuhich does not react below 700 °C.

In order to investigate the effects of the metallurgy at the M/GaAs interface on the electrical properties of the contact, electrical measurements on contacts before and after heat treatments have been carried out on all these three types of interfaces. The results of these measurements will be presented in the following sections. The sample preparation procedures for these diodes are given in the appendix. Electrical measurements were carried out with the current-voltage (I-V) dependence of diodes. Parameters measured include the

Schottky barrier height ϕ_{bn}, the ideality factor n and the leakage currents of the diode under reverse bias conditions. Corrections to the image force lowering effect (~0.04 eV) on the barrier heights[1] are included in the values of ϕ_{bn} presented. For the W/GaAs contact, capacitance-voltage (C-V) dependence measurements were also performed. Carrier concentration profile under the depletion region was obtained in this case.

5.1 Very Reactive M/GaAs Contact (M=Co, Ni and Pd)

Three systems of very reactive contacts were studied, namely Co/GaAs, Ni/GaAs and Pd/GaAs. Among these systems, Pd/GaAs has been found to react at temperatures below 100°C (see sections 3.5). One common characteristic of the contacts in this category is that their first growth phase at the M/GaAs interface is a ternary phase M_xGaAs (x=2 for Co, x=3 for Ni and x ranges from 2 to 4 for Pd).

Figure 5.1 shows semi-logarithmic plots of the forward and reverse I-V characteristics for the Pd/GaAs diodes as deposited and annealed at 250 and 350°C for 20 min. The Schottky barrier heights ϕ_{bn} of the diodes are obtained by extrapolating the linear portion of the curves to intercept the current axis. The ideality factors n are obtained from the slopes of the linear portion of these curves. It is clear from the plots that as the diode is annealed at 350°C, the leakage current increase by orders of magnitude. This increase in the leakage currents after heat treatment is also accompanied by a decrease in the

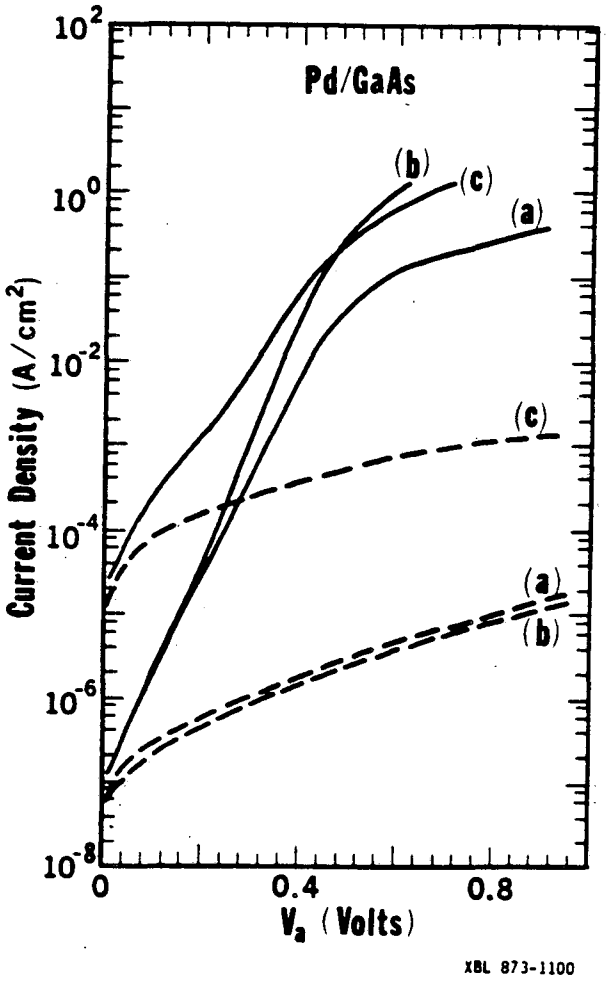

Figure 5.1 Semi-logarithmic plots of the forward (solid line) and reverse (dashed lines) current-voltage (I-V) characteristics for the Pd/n-GaAs diodes as deposited and annealed at 250 and 350 °C for 20 min.

barrier height and an increase in the ideality factor. A summary of the these parameters for the Co/GaAs, Ni/GaAs and Pd/GaAs diodes annealed at different annealing temperatures is given in Table XII.

It is observed in Table XII that the diodes improve at low temperatures (~200 °C) with increase in the barrier heights and decreases in ideality factors and leakage currents. Degradation of all the three types of diodes is noticed at temperatures around 300 °C.

Table XII Summary of the electrical measurements on the Co/GaAs, Ni/GaAs and Pd/GaAs diodes under isochronal annealing for 20 min at different temperatures.

	Annealing Temp. (°C)	ξ_{bn} (V)	n	Leakage current density at -.4 V (A/cm^2)
Co/GaAs	R.T.	0.79	1.29	$6X10^{-6}$
	300	0.67	1.67	$8X10^{-4}$
	400	0.57	2.6	$6X10^{-2}$
	500	ohmic		
Ni/GaAs	R.T.	0.76	1.30	$2X10^{-5}$
	220	0.833	1.21	$5X10^{-6}$
	350	0.750	1.24	$4X10^{-5}$
	400	0.64	1.80	$2X10^{-2}$
Pd/GaAs	R.T.	0.81	1.45	$2X10^{-6}$
	250	0.82	1.20	$1.5X10^{-6}$
	350	0.70	1.70	$4X10^{-4}$

This degradation is evident from the decrease in the barrier height; increase in ideality factor and orders of magnitude increase in the leakage current.

The results in section 3.1, 3.4 and 3.5 revealed that interactions between GaAs and the Co, Ni and Pd overlayers occur at the interface at below 300°C forming ternary M_xGaAs phases. Therefore improvements in these diodes at low temperatures are believed to be due to the the formation of a thin uniform layer of a ternary phase at the interfaces. These metal-GaAs interactions also disperse the native

oxide layers (~20-40 Å) mechanically[2]. As a result, abrupt, uniform and intimate M-GaAs/GaAs interfaces are produced so that the diodes annealed in this temperature range represent close to the ideal Schottky systems.

As the reactions proceed at temperatures around 300°C, large grains (size ~100-1000 nm) of these ternary phases are produced because of the weak M-M bonds in these metals (in the case of Pd, epitaxial phase I is found at low temperatures). The degradation of these diodes in this temperature range is probably the effect of the rough interfaces produced by the formation of large grains of the ternary phases. Since the electric field is enhanced in the vicinity of sharp corners and protrusions[3], the width of the potential barrier is decreased around large grain boundaries and thus thermionic field emission increases. Hence the effective barrier heights decrease for these diodes. Since thermionic emission is not the dominating process, the ideality factors increase significantly. Annealing at 500°C results in further degradation of the contact. In fact, ohmic instead of rectifying behavior is observed for these contacts. This can be attributed to the excessive interdiffusions occurring at the interfaces modifying the stoichiometry of the GaAs layer beneath the reacted layers. At the same time, the abrupt interfaces have turned into interdiffused and rough interfaces.

5.2 Reactive M/GaAs Contacts (M=Rh and Pt)

Metals such as Rh and Pt are considered reactive to GaAs since interactions at these M/GaAs interfaces occur at relatively low temperatures (~300°C). Table XIII shows a summary of the I-V measurements of the Rh/GaAs and Pt/GaAs diodes annealed at different temperatures. It can be observed from these data that optimum diodes with highest barrier heights as well as lowest ideality factors and leakage currents are obtained for diodes annealed at around 350°C. Degradations of both types of diodes result at annealing temperatures above 500°C.

Table XIII Summary of the electrical measurements on the Rh/GaAs and Pt/GaAs diodes under isochronal annealing for 20 min at different temperatures.

	Annealing Temp. (°C)	ϕ_{bn} (V)	n	Leakage current density at -.4 V (A/cm^2)
Rh/GaAs	R.T.	0.70	1.57	$1.5X10^{-4}$
	300	0.78	1.29	$1.5X10^{-5}$
	360	0.75	1.28	$2.5X10^{-5}$
	420	0.66	1.51	$1.0X10^{-2}$
	450	0.65	1.77	$4.0X10^{-2}$
	500	0.78	1.23	$1.0X10^{-5}$
	530	0.78	1.33	$1.0X10^{-6}$
	600	0.55	>2.0	$2.0X10^{-2}$
Pt/GaAs	R.T.	0.63	1.90	$1.0X10^{-4}$
	350	0.87	1.30	$6.0X10^{-7}$
	500	0.71	1.53	$1.0X10^{-3}$
	650	ohmic		

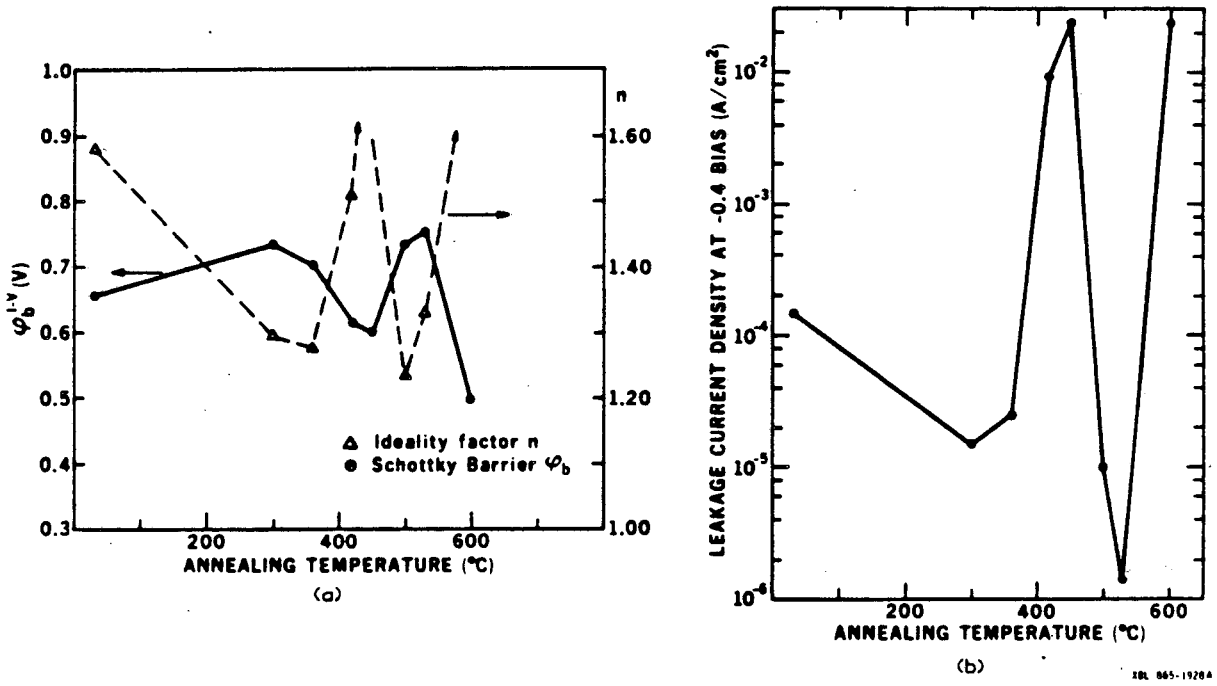

Figure 5.2 (a) Schottky barrier heights ϕ_{bn} and the ideality factor n as measured by the I-V dependence of the Rh/GaAs diodes as-deposited and annealed at various temperatures. (b) The leakage current densities of these diodes at -0.4 V bias.

Schottky barrier heights ϕ_{bn} and ideality factors n, as determined from the I-V dependence for as deposited and annealed Rh/GaAs diodes are shown in Figure 5.2(a). The leakage current densities of these diodes at -0.4 V bias are shown in Figure 5.2(b). Note that the ideality factor in the as deposited diodes deviates significantly from unity ($n \approx 1.57$). This is probably because of the presence of a layer of native oxide at the Rh/GaAs interface[4]. Cross sectional transmission electron microscopy measurements on Pt, Pd and Ni thin films on GaAs

with deposition conditions identical to those of this study revealed that a layer of ~10-20 Å thick existed at the M/GaAs interface in all of the unannealed samples[2]. From Figures 5.2(a) and (b) it is obvious that the diode characteristics of the Rh/GaAs diode undergo improvement after annealing at low temperatures (up to 350°C), degrade after annealing at temperatures ranging from 350 to 450°C, recover after annealing in the temperature range of 500 to 550°C and finally, fail completely after annealing at temperatures higher than 600°C. For Pt/GaAs diodes, annealing effects on the diodes are quite different. Only improvements and degradations at 350°C and higher than 500°C, respectively, are observed. The degradation and recovery of the diode properties at intermediate annealing temperatures (350 to 550°C) are not detected in the Pt/GaAs diodes.

After annealing at 300°C for 20 min, the ideality factor of the Rh/GaAs diode decreases from 1.57 to 1.29 and ϕ_{bn} increases from 0.70 to 0.78 eV. A decrease in the leakage currents by an order of magnitude is also noted as a result of the annealing. Since RBS and HIRBS analyses on this contact (section 3.2) reveal reactions at this annealing temperature, this improvement in the diode characteristics can be attributed to the formation of a thin layer (~100 Å) of RhAs at the interface. Consequently, the native oxide layer is mechanically dispersed by the Rh-GaAs reactions as previously observed for the Pt/GaAs reactions[2] resulting in a morphologically uniform and defect free interface. A similar explanation can be used to explain the improvement of the Pt/GaAs diode after annealing at 350°C for 20 min (ϕ_{bn} increase from 0.63 to 0.87 eV, n decreases from 1.9 to 1.3 and

leakage currents decrease by two orders of magnitude) with the formation of a uniform layer of $PtAs_2$ at the interface.

Drastic degradation (n increases to >1.7, ξ_{bn} reduces to 0.64 eV and the leakage currents increase by three orders of magnitude) are observed for Rh/GaAs diodes annealed at the temperature range of 400 to 450°C. This electrical degradation is most probably the result of the nucleation of the stable binary $RhAs_2$ phase at the original RhAs/GaAs interface. This nucleation leads to a laterally non-uniform interface morphology. The recovery of the Rh/GaAs diode after annealing at 500°C can be explained by the formation of a uniform layer of $RhAs_2$ at the interface so that a uniform interface morphology is restored. For Pt/GaAs diodes, the first phases formed are the binary Pt_3Ga and $PtAs_2$ phases at ~300°C with the $PtAs_2$ in intimate contact with GaAs (section 3.6). Annealing the Pt/GaAs diodes in the temperature range of 300-500°C results in the nucleation of the final stable PtGa phase at the $Pt_3Ga/PtAs_2$ interface without interfering with the morphologically smooth $PtAs_2$/GaAs interface. Therefore, the electrical properties of this diode remain unchanged in this temperature range.

Annealing both types of diodes at temperatures higher than 550°C results in severely degraded diodes. The diodes annealed at 700°C become ohmic rather than rectifying. Since the HIRBS analyses of these contacts annealed at temperatures higher than 600°C show significant amount of Ga and As in the reacted compounds on GaAs, it is expected that the failure is the result of GaAs outdiffusion (and possibly metal indiffusion) due to the dissociation of GaAs at the interface at high temperatures.

5.3 Non-reactive M/GaAs contact: W/GaAs contact

Figure 5.3 shows the forward and the reverse I-V characteristics of the W/GaAs diodes after annealing at various temperatures up to 900°C. Figure 5.4 displays the ξ_{bn} and n deduced from the I-V curves in Figure 5.3 and the reverse leakage currents at -0.4 V bias for diodes annealed at various temperatures. After annealing at temperatures between 300 and 500°C, the reverse leakage currents of the diode decrease by an order of magnitude. The forward currents for these

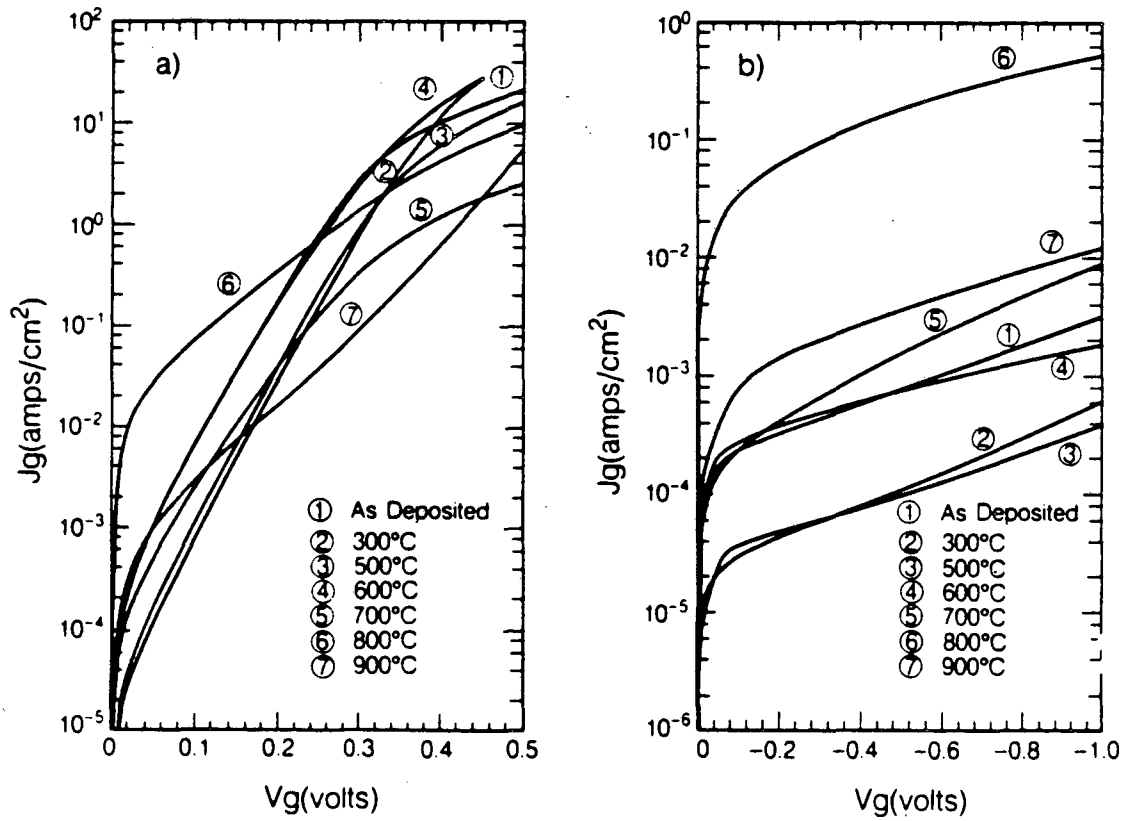

Figure 5.3 (a) Forward I-V curves for as deposited and annealed W/GaAs diodes. (b) Reverse I-V curves for as deposited and annealed W/GaAs diodes.

diodes also show very good linearity with n≈1.05 (n≈1.10 for as deposited diodes) in this temperature range. These values of n, ϕ_{bn} and the leakage currents indicate that the diodes annealed in this temperature range have close to ideal characteristics.

Degradation of the diodes is noticeable from the I-V curves after annealing at temperatures higher than 600°C. The ideality factor for the diode annealed at 600°C increases to 1.14 and the reverse leakage currents increase by an order of magnitude compared to the diode annealed at 300°C. After 700°C annealing, n becomes much larger than 1

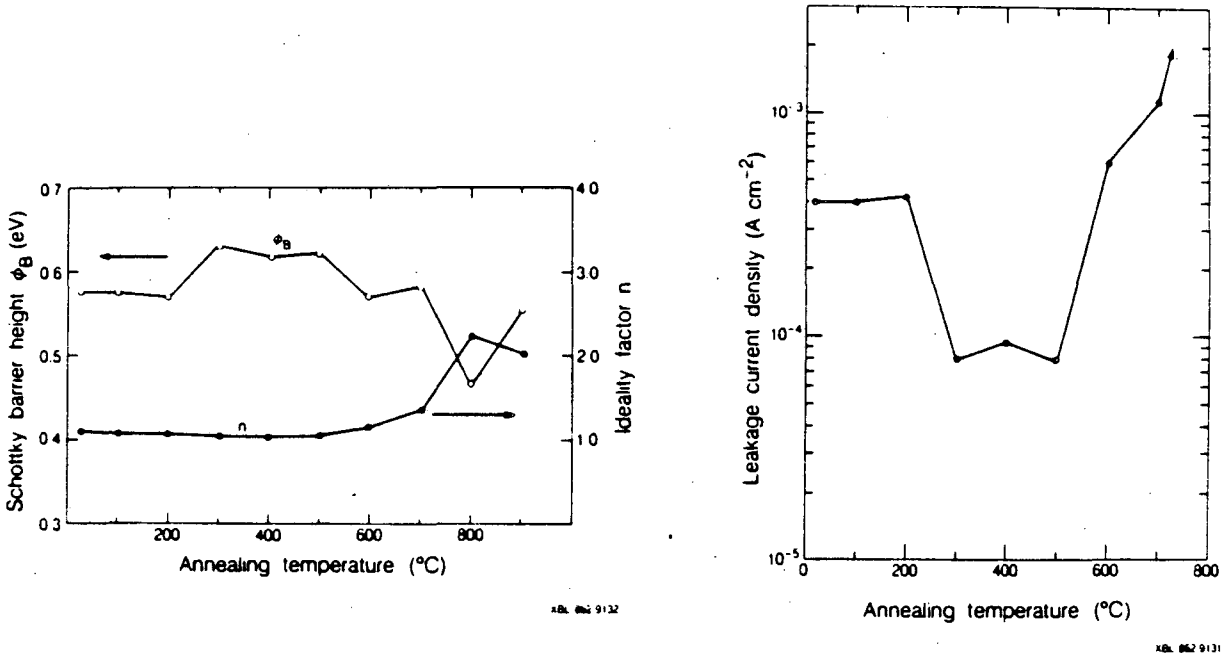

Figure 5.4 (a) Ideality factors n and Schottky barrier heights ϕ_{bn} measured from the I-V curves for W/GaAs diodes annealed at different temperatures. (b) Leakage current density at -0.4 V bias for diodes annealed at different temperatures.

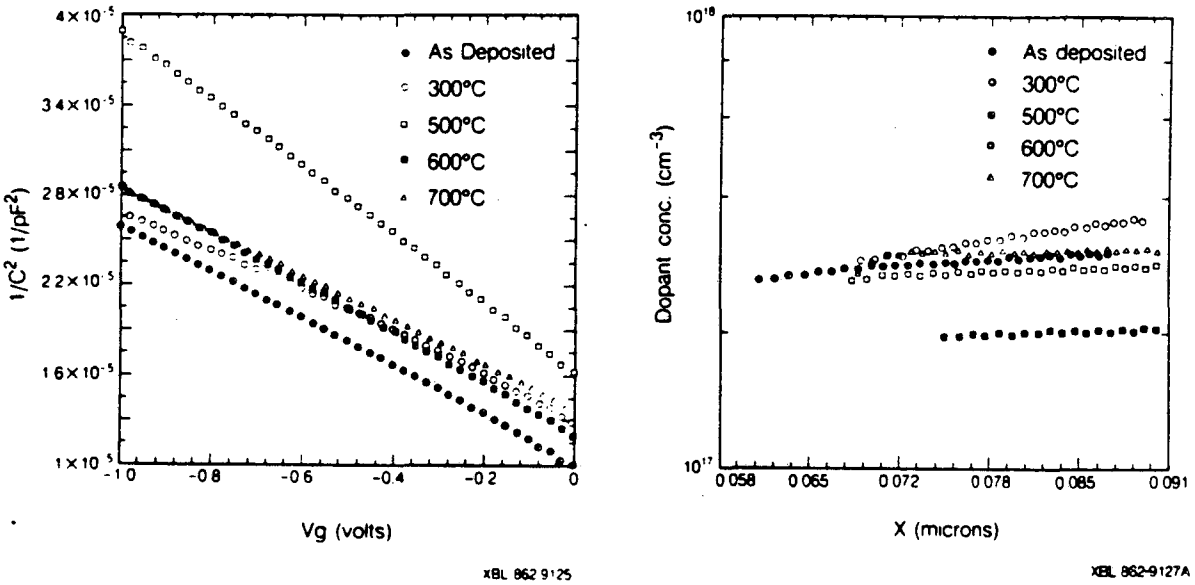

(a) (b)

Figure 5.5 (a) Plots of $1/C^2$ versus reverse bias V_R for W/GaAs diodes at different annealing temperatures. (b) Plots of the dopant concentration profiles for diodes annealed at different temperatures deduced from (a).

(~1.34) indicating that the diode characteristics can no longer be described with the ideal thermionic emission model. Higher temperature annealing at 800 and 900°C result in ohmic like behavior with comparable forward and reverse currents and n>2. The thermionic emission model can no longer be applied to the I-V characteristics of these contacts.

Figure 5.5(a) shows plots of $1/C^2$ versus reverse bias voltage V_R for the W/GaAs diodes under different annealing conditions. The dopant concentration profiles of the diodes calculated from these curves are shown in Figure 5.5(b). Relatively uniform dopant concentrations are observed for diodes annealed below 700°C ($N \sim 3X10^{17} cm^{-3}$).

The ideal behavior for W/GaAs diodes annealed at temperatures between 300 and 500 °C can be explained by the annealing out of defects due to native oxide and surface states at the interface, resulting in a sharp W/GaAs interface. The SEM images of this diode presented in section 4.7 suggest that the W films are more adherent to GaAs after annealing at low temperatures (<600 °C). The improvement of the diodes characteristics at these annealing temperatures is, therefore expected from the structural characteristics observed. This is in good agreement with the results of Waldrop[5]. Waldrop found that diodes with W evaporated on clean GaAs surfaces as well as GaAs surface covered with ~10 Å of native oxides exhibit nearly ideal behavior after annealing for 30 min in the temperature range 350 to 450 °C.

At annealing temperatures higher than 650 °C, glancing angle RBS results (section 4.7) suggest that interdiffusion occurs at the W/GaAs interface. After annealing at 700 °C for 20 min, the tungsten concentration is ~0.3 at.% at a depth of 500-600 Å below the interface. Since tungsten is known to be an acceptor in GaAs[6,7], it is expected that the tungsten atoms which diffuse into the GaAs substrate will change the electrical properties of the diode in two ways. First, the W levels present a high concentration of recombination centers near the junction. As a result, the recombination currents in the diode increase. According to the Shockley-Read-Hall model[8,9], the recombination current J_r can be expressed as follows:

$$J_r = J_{ro}\exp(qV/2kT),$$

where J_{ro} is the prefactor which depends on the geometry of the diode and the electronic properties of the substrate material. Therefore, the ideality factor for the forward I-V characteristics of the diode will approach 2 when the recombination currents increase. These effects are observed in the I-V characteristics of the W/GaAs diodes annealed at 600 and 700°C shown in Figure 5.3. The diode annealed at 600°C has n=1.13 which is slightly higher than diodes annealed at lower temperatures (n<1.1). The leakage currents for these diodes is also an order of magnitude higher than that for diodes annealed at lower temperatures. Further increase in the recombination currents is noted for diodes annealed at 700°C. The ideality factors for these diodes increase to 1.5 with a further increase in the leakage currents by a factor of 5 (as compared to the 600°C annealed diode). Thus it is suspected that significant tungsten diffusion actually started at ~600°C but this diffusion is, however, below the detection limit of RBS ($<10^{18}$ atoms/cm^3) and cannot be observed in the RBS spectra.

Second, when the concentration of tungsten acceptors in GaAs is high enough, the shallow donors will be significantly compensated by these acceptors resulting in a non-abrupt layer of higher resistivity GaAs at the interface. This highly resistive layer is between 600 to 1000 Å thick and does not have a sharp interface with the n-GaAs. The existence of this layer for the 600 and 700°C annealed diodes is indirectly confirmed by the inversion behavior under reverse bias in the low frequency C-V measurements on these diodes shown in Figure 5.6. Furthermore, a calculation based on the Norde's function[10,11] of

the series resistance of the diode using I-V data, indicates an order of magnitude increase in the series resistance of the 700 °C annealed diodes as compared to the 500 °C annealed diodes. Such an increase in the series resistance strongly suggests the presence of a highly resistive layer near the W/GaAs interface. Table XIV shows the results of the series resistance calculations derived from the Norde's approach. We propose that the W/n-GaAs diode transforms into a W/GaAs:Te+W/n-GaAs structure after annealing at temperatures >600 °C. Therefore, the electrical behavior deviates significantly from the ideal rectifying behavior.

The TEM and RBS measurements show that above 850 °C annealing, the W overlayer starts to react with the GaAs substrate and the reaction product, W_2As_3, tends to ball up, forming islands on the GaAs surface. At this stage, the diode is physically degraded with a very rough interface, as can be observed from the SEM micrographs in Figure 4.22. Parameters such as ideality factor, barrier height, depletion width, etc. obtained from the electrical measurements (I-V, C-V) become meaningless for these diodes.

Table XIV Series resistances R for the W/GaAs diodes as-deposited and annealed at 500 and 700 °C for 20 min calculated by using the Norde's function. Values of the ideality factor n for the corresponding diodes are also shown.

	as-deposited	500 °C, 20 min	700 °C, 20 min
n	1.10	1.05	1.34
R(Ω)	25.4	11.5	

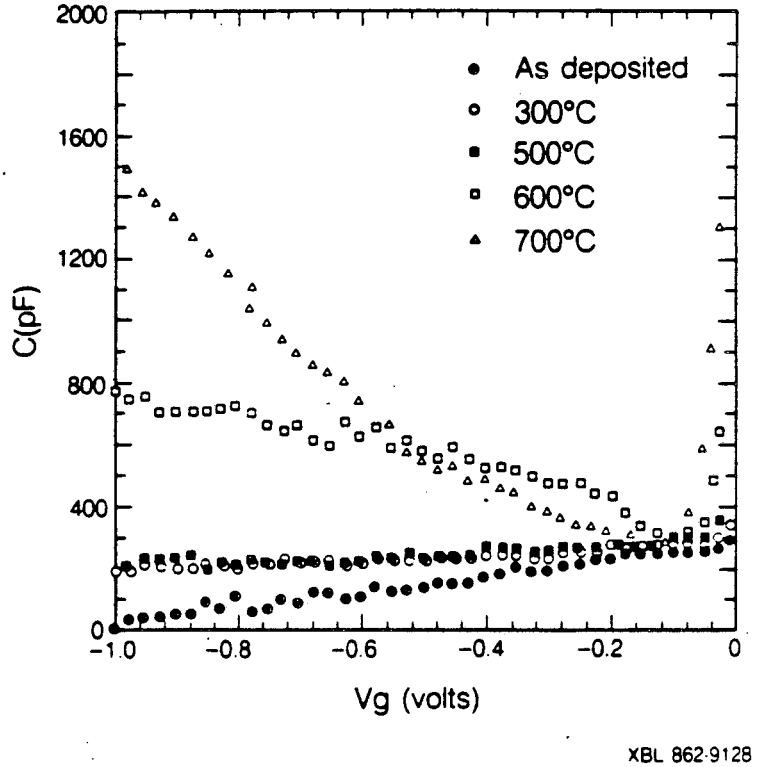

Figure 5.6 Low-frequency (80 Hz) C-V plots for as deposited, 600 and 700 °C annealed W/GaAs diodes. The inversion behavior for the diodes annealed at temperatures higher than 600 °C indirectly confirms the existence of high resistive GaAs layers at the interfaces of these diodes.

REFERENCES

1. R. H. Rhoderick, *Metal-Semiconductor Contacts*, p.39 (Clarendon, Oxford, 1978).

2. T. Sands, V. G. Keramidas, A. J. Yu, K. M. Yu, J. Washburn and R. Gronsky, J. Mat. Res. (to be published).

3. T. J. Lewis, J. Appl. Phys. **26**, 1405 (1955).

4. R. H. Rhoderick, *Metal-Semiconductor Contacts*, p.121 (Clarendon, Oxford, 1978).

5. J. R. Waldrop, Appl. Phys. Lett. **41**, 350 (1982).

6. V. V. Ushakov and A. A. Gippius, Sov. Phys. Semicond. **14**, 333 (1980).

7. V. V. Ushakov and A. A. Gippius, Sov. Phys. Semicond. **17**, 881 (1984).

8. W. Shockley and W. T. Read, Phys. Rev. **87**, 835 (1952); and R. N. Hall, Phys. Rev. **87**, 387 (1952).

9. C. T. Sah, R. N. Noyce and W. Shockley, Proc. IRE **45**, 1228 (1957).

10. H. Norde, J. Appl. Phys. **50**, 5052 (1979).

11. K. Sato and Y. Yasumura, J. Appl. Phys. **58**, 3655 (1985).

Chapter 6 FURTHER DISCUSSIONS OF EXPERIMENTAL RESULTS AND SUMMARY

Based on the experimental results presented in chapters 3, 4, and 5, some general trends in the solid phase reactions between thin film metal and GaAs substrate and their resulting electrical behavior can be observed. These observations including driving force for the reactions, formation and distribution of intermetallic phases, reaction kinetics and the influence of interface metallurgy on electrical properties of M/n-GaAs diodes will be given in the following sections.

6.1 Systematics of Solid Phase Reactions at Thin Film Metal/GaAs Interfaces

6.1.1 Reaction kinetics

Diffusion controlled kinetics is observed in all of the M/GaAs reactions at temperatures below 700 °C except for the Mo/GaAs interface. For the case of Mo/GaAs, the reactions are found to be linear with time. Such a dependence is usually explained with the interface controlled reactions and has been observed in the formations of refractory metal disilicides. This is consistent with the relatively high temperatures (≥650 °C) needed to initiate the Mo/GaAs interface reactions. The high temperature (>700 °C) phase transformations of the Ir/GaAs and Mo/GaAs contacts also deviate from the diffusion limited process. At such high temperatures diffusions of both, the metal atoms

and the substrate Ga and As atoms are so rapid that the reactions are no longer limited by the diffusion process. Instead, nucleation at the metal/GaAs interface become the dominant rate limiting process. When this occurs, the phase growth does not proceed in a layer by layer fashion but as columns at a very rapid rate.

The activation energies for M/GaAs reactions are in the range of 1.25-3.2 eV. These values are comparable to those found for silicide formation, indicating similar processes for the M/GaAs and M/Si interface reactions. For more reactive M/GaAs systems with M=Co, Rh, Pt, Ti and Zr, the activation energies are typically less than 1.7 eV. For the less reactive V/GaAs, Nb/GaAs and Ir/GaAs systems (and possibly the Mo/GaAs), the activation energies are higher than 2 eV. Activation energies for the very reactive Ni/GaAs and Pd/GaAs systems are expected to be very low ($\leq$1.5 eV). However, the detail kinetics of these contacts is not measured because of the rapid reaction rates and the low annealing temperatures ($\leq$200°C) involved.

6.1.2 Interface reactivity

Reactivity of the thin film metal/GaAs interfaces is related to the nature of the metal layers. Near noble metals which have high electronegativity and weak metal-metal bonds (and thus have low heat of vaporization) are found to be more reactive than the electropositive refractory metals which have strong M-M bonds. In addition, the near noble metals also have a strong tendency to attain the stable d^{10} electronic structure through electron transfer resulting from the formation

of the stable M-Ga and M-As phases. Consequently, near noble metal films (except for iridium) react with GaAs at temperatures $\lesssim$300 °C while the refractory metal films react with GaAs at temperatures $\gtrsim$400 °C.

Therefore there are primarily two major driving forces for the solid phase reactions at the M/GaAs interface: 1) the M-M bond strength which is manifested in the heats of vaporization (or heats of formation) of the metals; and 2) the electronegativity differences between the metal and the Ga and As. Electronegativity difference of a molecule A-B in the Pauling's scale is defined as the square root of the difference between the actual bond energies D(A-B) and the arithmetic (or geometric) mean of the corresponding symmetrical bond energies[1]. Thus, it is reasonable to assume that the interface reactivity of an interface is directly dependent on the sum of the square of the electronegativity differences of M-Ga and M-As and inversely depen-dent on the heat of vaporization ΔH of the metal. Consequently, one can define a reactivity parameter R in the following way:

$$R \sim \frac{(X_M - X_{Ga})^2 + (X_M - X_{As})^2}{\Delta H} . \qquad (6.1)$$

Hence, an interface with a high R value is very reactive and vice versa. Table XV shows the calculated values of R and the activation energies of reactions for the M/GaAs systems studied in this work in the order of increasing temperature for initial interface reactions. With a few exceptions, a general trend of decreasing reactivity number R can be observed in the table.

Table XV The *R* values for different metals as calculated from equation (6.1). The activation energies for the corresponding M/GaAs reactions are also tabulated. The metals are arranged in the order of increasing reaction temperature.

Metal	*X*	Reaction Temp. (°C)	Heat of Vaporization (eV/molecule)	Activation Energy (eV)	*R*
Pd	2.2	≤200	3.94	-	0.102
Ni	1.8	200	4.45	-	0.018
Co	1.8	250	4.40	1.68 ±0.1	0.018
Pt	2.2	300	5.85	1.60 ±0.15	0.068
Rh	2.2	300	5.76	1.65 ±0.20	0.069
Zr	1.4	450	6.29	1.25 ±0.10	0.064
Ti	1.5	450	4.87	1.53 ±0.15	0.053
Cr	1.6	450	4.11	-	0.039
V	1.6	450	5.32	2.10 ±0.10	0.030
Ir	2.2	500	6.88	3.15 ±0.20	0.058
Nb	1.6	550	7.49	2.60 ±0.30	0.021
Mo	1.8	650	6.80	-	0.012
W	1.7	750	8.74	-	0.011

Notable exceptions to this dependence are three near noble metal/GaAs systems: Ni/GaAs, Co/GaAs and Ir/Gas. The Ni/GaAs and Co/GaAs contacts have very low R values (<1) but are known to react at very low temperatures ($\leq$200°C); while the Ir/GaAs has relatively large R but has high initial reaction temperature (~500°C). Therefore additional factors must be present and play dominant role in the interface reactions of these systems. In the cases of the very reactive Ni/GaAs and Co/GaAs contacts, initial reactions at low temperatures result in the formation of ternary Ni_3GaAs and Co_2GaAs, respectively. The formation of these ternary phases is consistent with the fact that $X_{M-Ga}=X_{M-As}$ for these systems ($X_{Co}=X_{GaAs}=1.8$) this also mean that the electronegativity driving forces for the formation of M-Ga and M-As phases are equal. These ternary phases are formed epitaxially on the GaAs substrate with very small lattice mismatch (<2%) which makes the reactions energetically favorable. Thus these systems are very reactive despite of their low R values. According to the R value, the Ir/GaAs contact should react at temperatures around 450°C with activation energy of ~1.5 eV. However, experimental results show that the Ir/GaAs interface reacts at ~500°C with high activation energy of ~3 eV. This non-reactive nature of the Ir/GaAs contact is consistent with the high heat of vaporization for the iridium metal indicating that the electronegativity factor is less dominant in this case.

Figure 6.1 shows a plot of the activation energy for interface reactions for the M/GaAs systems studied in the present work versus the logarithm of R. The refractory metal/GaAs systems follow a linear

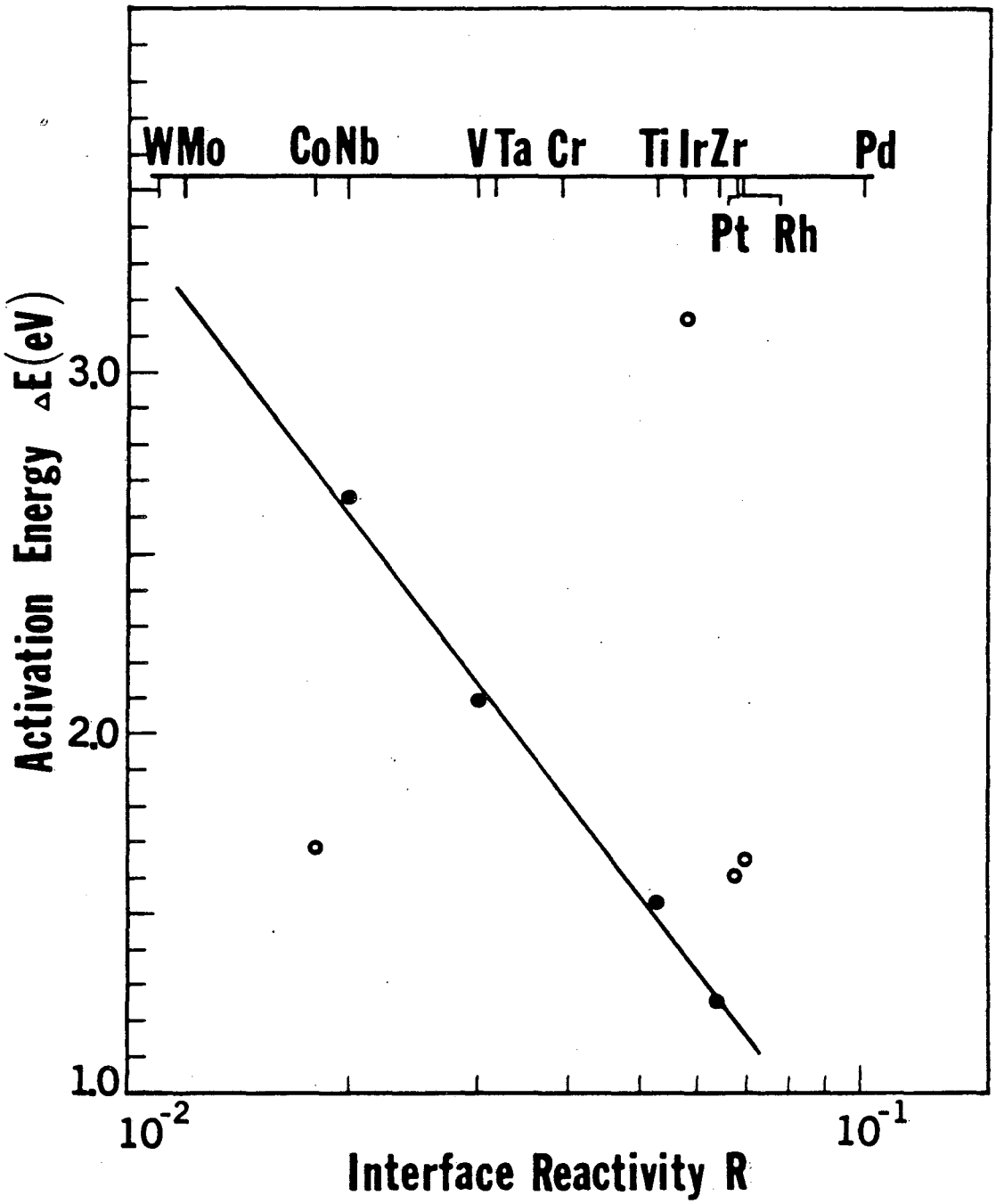

XBL 872-565

Figure 6.1 A plot of the activation energies for interface reactions for M/GaAs systems studied in the present work versus the logarithm of the reactivity parameters *R* as calculated from equation (6.1). The open circles are data from near noble metals and the full circles are from refractory metals.

relationship. The near noble metal/GaAs contacts do not display a simple relationship between R and ΔE. Thus it can be concluded that for reactions at refractory metal/GaAs interfaces, the reactivities follow equation (6.1). The activation energies for these systems depend on their corresponding R values in the following way:

$$\Delta E = C + K\ln(R) \tag{6.2}$$

where C and K are fitting parameters and their values can be deduced from the plot in Figure 6.1. A least square fit for data in Figure 6.1 yields $C \approx -2.3$ and $K \approx -1.3$. Alternatively one can express the reactivity as $R \sim \exp(-\Delta E/1.3)$.

6.1.3 Phase distribution

Distribution of the different phases formed in M/GaAs reactions is found to follow an electronegativity rule: phase stratification occurs for $|X_M - X_{Ga}| \neq |X_M - X_{As}|$. In these cases, a layer sequence of M-Ga/M-As/GaAs is always observed. When $(X_M - X_{Ga}) > (X_M - X_{As})$ (in the cases of the near noble metals: Pt, Rh and Ir), the electropositive Ga diffuses into the electronegative metal layer leaving the As relatively immobile at the interface. When $|X_M - X_{Ga}| < |X_M - X_{As}|$ (in the cases of the refractory metals: Zr, V, Nb, Cr and W), the metal is the relatively electropositive species in comparison to the As. Therefore the metal diffuses to the interface and preferentially reacts with As forming M-As at the interface. The Ga released in the M-As reaction reacts with the in-diffusing metal atoms forming a layer of M-Ga on top of the M-As phase.

In the case of the Co/GaAs and Ni/GaAs, X_M=1.8 and $|X_M-X_{Ga}|=|X_M-X_{As}|$. Hence the formation of ternary M_xGaAs phase is more favorable.

The Pd/GaAs and Mo/GaAs contacts are an exception to the above rule. For Pd/GaAs, the ternary phase I is formed epitaxially on the GaAs substrate at temperatures below 200°C (possibly around 100°C). This low reaction temperature and the high epitaxial quality of phase I, leads to the speculation that the formation of phase I is energetically more favorable at the Pd/GaAs interface. Molybdenum has X=1.8 and hence should react similarly to Co and Ni. However, Mo/GaAs reactions which are initiated at high temperatures result in the formation of stratified Mo-Ga and Mo-As phases. This may be due to the high reaction temperatures at which the the GaAs at the interface is dissociated and thermally induced interdiffusion occurs. It is possible that the diffusion coefficient of Ga in Mo is much higher than that of As in Mo at this temperature which would account for the observed phase stratification. Unfortunately, diffusion coefficient data for Ga and As in Mo are not available for comparison.

In addition to the electronegativity rule mentioned above, phase stratification in M/GaAs systems is also dependent on the thickness of the reacted layer. When the grain size of the reacted phases is comparable or larger than the reacted layer thickness, the phases can only be laterally separated in order to minimize interface energy. As has been discussed in chapter 3, the grain size of the reacted phases is, in turn, dependent on the M-M bond strength of the metal. Therefore, for very thin ($\lesssim$200 Å) film metal/GaAs, phase stratification is only observed for metals with very strong M-M bonds (such as Ir).

6.2 Dependence of Electrical Properties on The Interface Reactions of Metal/n-GaAs Diodes

Results of the electrical measurements of the six types of diodes presented in chapter 5 are summarized in Table XVI. The values of ϕ_{bn}, n and leakage current densities at -0.4 V bias shown in Table XVI are those of the best diode (lowest n and leakage current and highest barrier) for each system. The annealing temperatures at which these diodes are obtained, T_o, are also given in the table. Comparing Table XVI with Tables XII and XIII in chapter 5, one notices that the values of T_o are the same as those at which initial reactions at the interface are observed. For the W/GaAs diode, although no metallurgical reaction is observed up to 700 °C, the diode exhibits ideal behavior after annealing at 300 °C and remains ideal up to 600 °C. This can be attributed to the balling up of the native oxide at high temperatures resulting in an intimate contact between the tungsten and GaAs. In addition, tungsten, being an electropositive metal, may react with the GaAs native oxide[2]. Note that the ideality factors for these diodes deviate significantly from unity ($n \sim 1.2$). This is mainly due to the high doping concentration of the substrate ($n \approx 2\text{-}3 \times 10^{17} cm^{-3}$). An exception is the W diode ($n \approx 1.05$) which has a better interface as a result of sputter deposition. These values of n are in good agreement with the results of Zussman[3] who explored the effects of high substrate doping and different deposition techniques on the diode characteristics.

Table XVI Summary of electrical measurements on six type of diodes after annealing at T_o.

Metal/GaAs	Annealing Temp. T_o	ϕ_{bn} (V)	n	Leakage current at -0.4V (A/cm^2)
Co/GaAs	<300 °C	0.787	1.29	$6X10^{-6}$
Ni/GaAs	220 °C	0.833	1.21	$5X10^{-6}$
Rh/GaAs	300 °C	0.781	1.29	$1.5X10^{-5}$
Pd/GaAs	250 °C	0.820	1.20	$1.5X10^{-6}$
W/GaAs	300 °C	0.679	1.05	$8X10^{-5}$
Pt/GaAs	350 °C	0.870	1.30	$8X10^{-7}$

Degradation in the diode properties for Co, Ni and Pd diodes is observed after annealing at temperatures higher than 350 °C. This can be correlated to the formation of a laterally irregular interface morphology of the diodes resulting from the disintegration of the intermediate ternary phases and precipitation of binary phases in this temperature range. Degradation of the Pt diode starts at temperatures higher than 500 °C due to the interdiffusion of the Pt and Ga and As atoms at the interface region. The degradation and recovery of the Rh diode in the temperatures range of 400-550 °C has been discussed in detail in the last chapter. Interdiffusion is also observed for the W diode after annealing at temperatures >650 °C and are accounted for the degradation of this diode at these temperatures.

Values of the barrier heights for the diodes annealed at optimum temperatures along with the barrier heights of as-deposited diodes are shown in Figure 6.2. Note a very distinct difference between the very

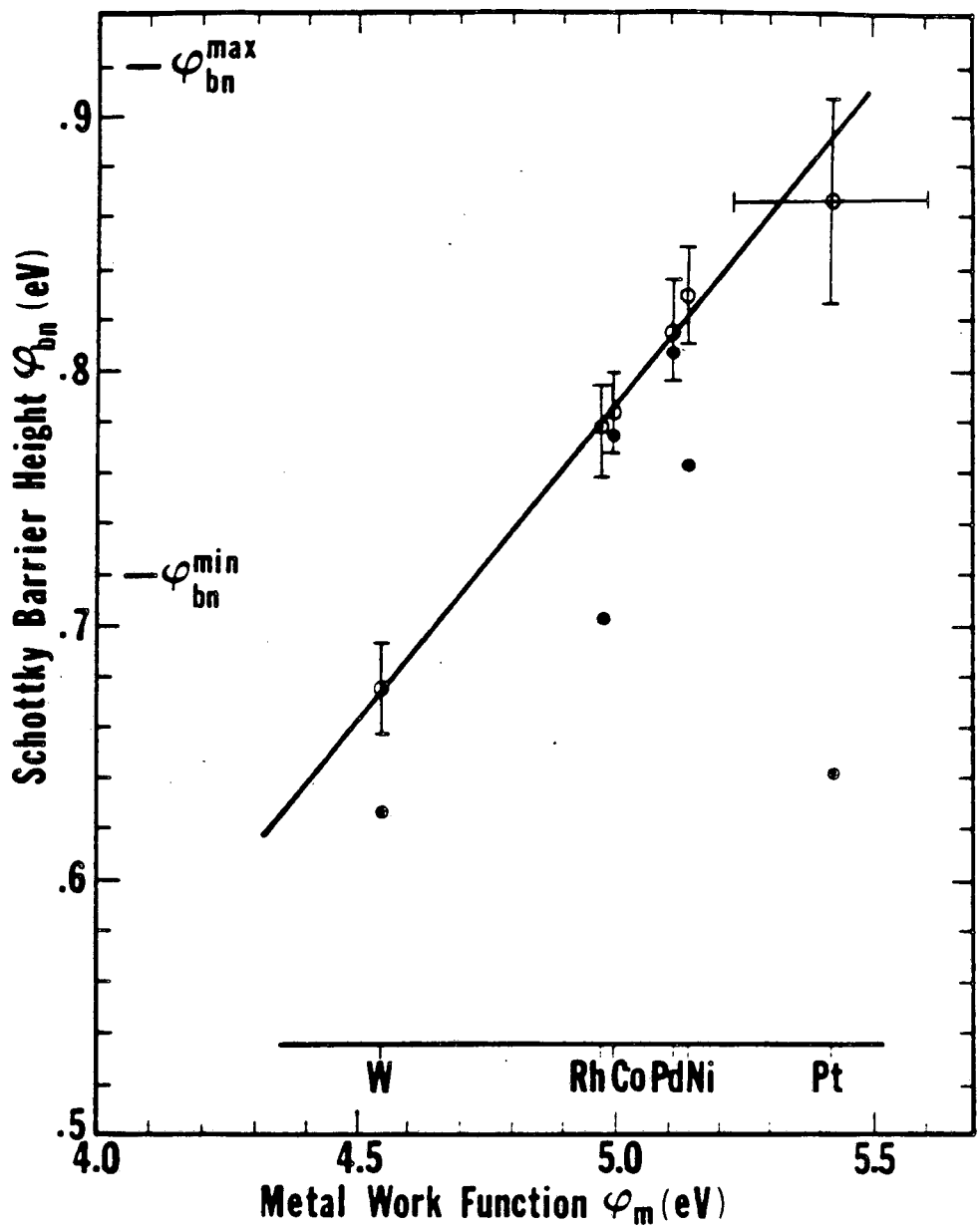

XBL 872-568

Figure 6.2 A plot of the Schottky barrier heights φ_{bn} of M/GaAs diodes (M=Co, Ni, Rh, Pd, W and Pt) as deposited (filled circles) and after annealing at T_o (open circles) versus the metal work functions φ_m.

reactive metals Co, Ni and Pd and the relatively non-reactive Pt, Rh and W. The diodes with the very reactive metals show no substantial increase of the barrier height upon annealing. In the latter case, the barrier properties are well established during room temperature metal deposition. Barrier heights for less reactive metals increase upon annealing at elevated temperatures. This effect is especially visible for Pt diodes where an increase of the barrier height by more than 0.2 eV is observed.

These experimemtal data can be understood in terms of the recently proposed amphoteric defect model[4] discussed in section 1.2.4. In this model the barrier height is determined by the pinning of the fermi energy in he range from 0.5 to 0.7 eV above the valence band maximum. This leads to the barrier height limits ξ_{bn}^{max}= 0.92 eV and ξ_{bn}^{min}= 0.72eV. The lower and upper limit of this range is given by an energy level of (As_{Ga}, V_{As}) donor complex and the V_{Ga} acceptor, respectively. The final pinning positions in this range depends on additional factors such as metal electronegativity (or work function) and concentration of the native defects. The latter factor may in turn be affected by the surface preparation conditions and/or solid phase reactions at the interface.

It is known that the surface preparation technique used in the present work leads to an oxidized surface[5] with the fermi level pinned at ~0.7 eV above the valence band[6]. Deposition of a non-reactive (at room temperature) metal results in the formation of a barrier determined by this initial pinning. On the other hand, highly reactive

metals disperse the interface oxide during the deposition ensuring intimate contact between metal and semiconductor. For non-reactive metals, higher temperatures are required to induce such reactions. The fact that optimum Schottky barrier heights are very close to the limits predicted by the defect model indicates that most of the defects responsible for pinning are located at some distance from the interface so that they are not affected by the initial chemical reactions directly at the interface.

The barrier height dependence on metal electronegativity is in general agreement with the prediction of the defect model. The only exception is the highly electronegative Rh which forms barrier lower than 0.8 eV. To account for such an exceptions, better understanding of the effects of interface reactions on the defect stability would be required. As seen in figure 6.2, the optimum barrier height also shows a linear dependence on the experimental metal work function[7]. This observed linear dependence is believed to be due to the existence of the thin interface reacted layer. For all the metal/GaAs systems studied, these interface layers have [M]/[GaAs] $\geq$2. They are, therefore, expected to have work functions close to those of their corresponding metals.

6.3 Summary

Summaries of the results on the solid phase reactions of thin film metal/GaAs interfaces are given at the end of chapters 3 and 4 in this thesis. In this section, the major conclusions of this investigation will be summarized.

1) Diffusion controlled reaction rates dominate for thin film M/GaAs solid phase reactions. Exceptions are the initial reactions of Mo/GaAs which is interface reaction rate controlled and the high temperature phase transformation of Ir/GaAs and Mo/GaAs which are nucleation controlled.
2) Interface reactivity of M/GaAs systems, especially for M= refractory metals, depends primarily on the M-M bond strength of the metal and the electronegativity differences between metal and the substrate Ga and As. An empirical relationship between the activation energies for refractory metal/GaAs reactions and an interface reactivity parameter R defined by equation 6.1 has been established (equation 6.2).
3) The phase distribution in the reacted layer is determined by the electronegativity of the deposited metal. The large electronegativity difference between electronegative metals ($X>2$) and Ga and that between electropositive metals ($X<1.8$) and As results in relatively immobile As at the GaAs interface and thus stratification of phases in the sequence of M-Ga/M-As/GaAs.

4) For very thin overlayers ($\lesssim$200 Å), when the grain size of the reacted phases is larger than the layer thickness, minimization of the interface energies of the system prohibit the vertical stratification of the phases. The grain size of the phases is related to the M-M bond strength of the metal, i.e. stronger the M-M bond the finer will be the reacted grain size.

5) The final stable phases for the solid phase reactions of all metal/GaAs contacts are the binary M-Ga and M-As phases. For thin ($\approx$200 Å) Pd/GaAs under uncapped annealing in forming gas or in vacuum, a ternary phase (phase II) which is As deficient can be the stable phase.

6) Initial solid phase reactions at M/GaAs interface reduce the original native oxide at the interface and thus improve diode properties.

7) Phase nucleation at the GaAs interface results in a laterally nonuniform interface leading to high electric field spots which in turn degrade the diode properties.

8) The barrier heights of diodes which achieve intimate contact with the GaAs substrate through solid phase reactions are limited by the native defects which are located below the interface. Within these limits, the barrier heights of the diodes shows a linear dependence on the metal work function which is related to the work function (electronegativity) of the reacted interface layer.

We have investigated the thermally activated interactions between metal thin films and GaAs substrates. Recent investigations on other activation processes such as ion beam mixing and rapid thermal annealing also show good promise for the fabrications of contact structures to GaAs devices. Studies similar to this one should be carried out for these processes in the future in order to obtain a complete understanding of metal/GaAs interfaces. It is our hope that this comprehensive and systematic study forms a scientific basis contributing to GaAs technology. There can be no doubt that GaAs will play an increasing important role in optoelectronics and very high speed applications and a well understood contact technology is one of the fundamentals for the success of this new technology.

REFERENCES TO CHAPTER 6

1. L. Pauling, *The Nature of Chemical Bonds*, Cornell University Press, Ithica, 1960.

2 J. R. Waldrop, Appl. Phys. Lett. **41**, 350 (1982).

3. A. Zussman, J. Appl. Phys. **59**, 3894 (1986).

4. W. Walukiewicz, presented at the 14th Conference on the Physics and Chemistry of Semiconductor Interfaces, Salt Lake City, Utah, Jan. 26-29 (1987).

5. T. Sands, V. G. Keramidas, A. J. Yu, K. M. Yu, R. Gronsky and J. Washburn, to be published, J. Mat. Res (1987).

6. N. Newman, W. E. Spicer, T Kendelewicz and I. Lindau, J. Vac. Sci. Technol. **B4**, 931 (1986).

7. R. C. West, M. J. Astle and W. H. Beyer, ed., *CRC Handbook of Chemistry and Physics*, E76, CRC Press, Florida, 1983.

APPENDIX: SAMPLE PREPARATION PROCEDURES

1. GaAs surface preparation

· Semi-insulating undoped and n-type Te doped ($n \sim 2X10^{17} cm^{-3}$) GaAs wafers were degreased by boiling in trichloroethane, acetone and methanol for 5 minutes each.

· The wafers were etched in a 50% HCl solution for 1 minute in order to reduce the thickness of the native oxide on the GaAs surface.

· Wafers were rinsed in deionized water and blown dry with N_2.

2. Metal Film and Oxide Cap Depositions

· Clean GaAs wafers were loaded into an evaporation chamber which was evacuated with a diffusion pump to a base pressure below 10^{-6} Torr.

· Thin films of Co, Rh, Ir, Ni, Pd, Pt, V, Cr and Mo with various thicknesses (100-1500 Å) were deposited on the wafers by electron beam evaporation.

· Films of Ti, Zr, Nb and W were sputter deposited onto the GaAs substrate at an argon pressure of ~15 mTorr.

· The metallized wafers were then cut into small pieces and capped on all sides with ~1500 Å of SiO_2 film deposited by plasma enhanced chemical vapor deposition at a substrate temperature of 150°C.

3. Annealing and Cap Removal

· Annealings were carried out in the temperature range of 100-900°C for various time durations in a flowing N_2 or forming gas ambient.

· The oxide caps were then removed by dipping the samples in a solution of buffered HF solution for ~3 minutes.

4. Diode Fabrication

· Circular diodes (diameter~1 mm) were patterned on the wafers by placing a metal shadow mask on the wafer during electron gun deposition of the Co, Ni, Rh, Pd and Pt films.

· For sputter deposited W diodes, circular dots were defined on the substrate using standard photolithography.

· For diodes annealed at temperatures higher than 450°C, ohmic contacts of the diodes were fabricated on the back side of diodes after the annealing by depositing ~1000 Å of Au-Ge eutectic alloy followed by a brief annealing treatment at 425°C after removal of the oxide caps.

· For diodes annealed at temperatures below 450°C, the back ohmic contacts were formed before metal deposition.

LAWRENCE BERKELEY LABORATORY
TECHNICAL INFORMATION DEPARTMENT
UNIVERSITY OF CALIFORNIA
BERKELEY, CALIFORNIA 94720